UNIVERSIDAD DE CHILE
FACULTAD DE CIENCIAS FÍSICAS Y MATEMÁTICAS
DEPARTAMENTO DE INGENIERÍA ELÉCTRICA

DEVELOPEMENT OF MICROWAVE DEVICES FOR MILLIMETER AND SUB-MILLIMETER RECEIVERS

TESIS PARA OPTAR AL GRADO MAGÍSTER EN INGENIERÍA ELÉCTRICA

IGNACIO ALBERTO HUGO BARRUETO GONZÁLEZ

PROFESOR GUÍA:
FAUSTO PATRICIO MENA MENA

PROFESOR CO-GUÍA:
NETTY HONINGH

MIEMBROS DE LA COMISIÓN:
NICOLÁS REYES GUZMÁN
URS GRAF

Este trabajo ha sido parcialmente financiado por CONICYT través de los proyectos FONDECYT 11151022 y BASAL PFB06

SANTIAGO DE CHILE
MAYO 2017

ABSTRACT

DEVELOPEMENT OF MICROWAVE DEVICES FOR MILLIMITER AND SUB-MILLIMITER RECEIVERS.

The Atacama Large Millimeter/Submillimeter Array (ALMA) is one of the largest astronomical facilities in the world. Each of the 66 antennas accommodates ten observational bands, covering from 35-950 GHz. To extend the operative lifespan of ALMA, a continuous upgrade program is in place. Among other objectives, this program pursues the increase of bandwidth of the instruments and the need to complement ALMA with another observatories supporting multi-pixel arrays. This thesis work is placed within two projects that attempt to reach those goals. The first is the ALMA Band-2+3 upgrade proposal, that attempts to merge Bands 2 and 3 in a single receiver. The second one is the development of instrumentation for the CCAT-p Telescope, to be placed next to the site of ALMA, at Cerro Chajnantor.

A heterodyne receiver is composed by the feed antennas which captures the radiation concentrated by the main dishes. Depending on the structure of the receiver, an orthomode transducer (OMT) separates the polarization in two orthogonal components. Subsequently the signal is mixed with a local oscillator signal in order to down-convert the original signal. More specifically, this thesis presents the design, construction and characterization of a turnstile OMT for ALMA Band 2+3 receiver and the study and design of a LO power distribution scheme for the CCAT-p Heterodyne Array Instrument.

The OMT should comply with the stringent ALMA requirements set for all passive devices. A design was conceived to solve construction issues of a previous version. The measurements show that the OMT does comply with most of them. However, a disagreement between the simulations and measurements prompted us to determine the effective conductivity of milled waveguides at 15, 77 and 290 K. In order to do so, we characterized waveguide meanders. These results improved the agreement and could used on future design efforts.

The LO power distribution of CHAI requires to deliver the LO signal to an 4×4 array, which will serve as a basic block for larger arrays configurations. The 4×4 array will be assembled out of 4 rows of $1{\times}4$ pixels. The distribution must cover the 800-820 GHz band, the imbalance between power delivered to each mixer must be lower than -3 dB and the whole distribution must fit within a footprint of 40×40 mm^2.

We have presented two designs based on coplanar waveguides (CPW) and waveguide technology, a balanced scheme based on hybrids and an imbalanced scheme based on Wilkinson power dividers. The balanced scheme required waveguides of considerable length, generating standing waves that created a considerable imbalance in the power distribution. The second scheme is an unequal power distribution that has a theoretically better performance but requires 3:1, 2:1 and 1:1 Wilkinson dividers. The simulations of 3D model of a CPW 3:1 Wilkinson shows that the actual model does not achieve the expected performance. However, further optimization promises an improvement in performance. In both projects we have demonstrated that careful design makes possible to obtain devices whose performance surpass the current state of the art.

My earnest gratitude to all the people whose
help and support made this work possible
Thanks

Contents

1 Introduction **1**
1.1 Background 1
1.2 Heterodyne Receivers 3
1.3 Modern Heterodyne Receivers 5
1.3.1 Single pixel receivers 5
1.3.2 Multi pixel receivers 7
1.4 CCAT-p 9
1.4.1 Science with CCAT-p 9
1.5 Context of this work 11
1.6 Hypothesis 12
1.7 Objectives 12
1.8 Scope of this Thesis 13

2 Theory and Design **14**
2.1 Scattering Matrix 14
2.2 Electromagnetic Waves 15
2.2.1 Free space propagation of electromagnetic waves 16
2.2.2 Polarization of a wave 17
2.3 Electromagnetic Propagation in Hollow Waveguides 18
2.3.1 Waveguides 18
2.3.2 Orthomode Transducer 23
2.4 Electromagnetic Propagation in Coplanar Waveguides 24
2.5 Summary 26

3 Orthomode Transducer **27**
3.1 Previous OMT Design for ALMA Band 2+3 27
3.2 Second Version of the OMT 30
3.3 Constructions of Waveguides 33
3.4 Experimental setup 33
3.5 Results 34
3.6 Conductivity Measurement across the W Band 37
3.7 Summary 41

4 SMAI **42**
4.1 First Power Distribution Design 42
4.1.1 Hybrid Design 44

4.1.2 CPW-to-waveguide Transition 49
4.1.3 Simulation of the Basic Distribution Block 50
4.2 Second Power Distribution Design 53
4.2.1 Wilkinson Power Dividers 54
4.2.2 3:1 Wilkison design 58
4.3 Simulations of the 3:1 Wilkinson 61
4.4 Summary 62

5 Conclusions and Future Work **64**
5.1 Effective Conductivity Measurement 64
5.2 OMT for ALMA BAND 2+3 64
5.3 LO-power distribution for SMAI 65

Bibliography **66**

List of Tables

1.1 Band distribution of ALMA . . . 7

3.1 Comparison between simulations and experimental results for the OMT . . . 35
3.2 Conductivity of Aluminium and Copper of milled waveguides at different temperatures . . . 41
3.3 Comparison between simulated insertion losses with the effective conductivity and experimental results . . . 41

4.1 Calculated dimensions of the hybrid . . . 44
4.2 Optimised dimensions of the hybrid . . . 48
4.3 Calculated impedance values for the three Wilkinson power dividers . . . 54
4.4 Calculated dimension for the $3:1$ Wilkinson power divider . . . 60
4.5 Comparison between theoretical and simulated results for the 3:1 Wilkinson power divider . . . 61

List of Figures

1.1 Half absorption altitude of the electromagnetic spectrum on earth 2
1.2 Atmospheric transmission at the Chajnantor plateau 2
1.3 Schematic of an ideal mixer 3
1.4 Basic mixer example 3
1.5 Schematic of a Double Sideband receiver. 4
1.6 Schematic of a Single Sideband receiver. 4
1.7 Schematic of a Double Sideband receiver. 4
1.8 Cryostat and front end 5
1.9 Cartridge and schematic of ALMA bnads 3 and 1 6
1.10 First proposed design of CCAT 10
1.11 Current design under discussion 10
1.12 SMAI pixel configuration for one band. It can be noted the modular nature of the CHAI receiver , with SMAI serving as the basic block of it. 12

2.1 Portrayal of an arbitrary network of N ports 15
2.2 Basic configurations of propagation modes 17
2.3 Types of polarization 18
2.4 Geometry of a rectangular waveguide 18
2.5 TE mode field lines 19
2.6 Field lines of the TM modes 20
2.7 Geometry of a circular waveguide 21
2.8 TE mode field lines 22
2.9 TM mode field lines 23
2.10 Juntura turnstile 23
2.11 Scheme of a CPW with a substrate of finite thickness 25
2.12 Even quasi-TEM mode of a cpw 25

3.1 Previous design of the OMT 28
3.2 Reflections at the input port of the OMT v1.0 28
3.3 Copolar Transmission of the OMT v1.0 28
3.4 Crosspolar Transmission of the OMT v1.0. 29
3.5 Transmission between output ports of the OMT v1.0 29
3.6 New model proposed 30
3.7 Cuts and current distribution for a TE_{10} mode. The fabrication of the OMT required that waveguides in the same plane of the Y-power combiners to have seams in $x = 0$ and $x = a$ respectively. 31

3.8 Simulated reflections at the input port of the OMT 31
3.9 Simulated copolar transmissions of the OMT 32
3.10 Simulated crosspolar transmissions of the OMT 32
3.11 Simulated transmissions between output ports of the OMT 32
3.12 Built OMT and Horn 33
3.13 Measurements of the OMT with an Anritsu VNA.(a) Measurement setup for the reflections and isolations between ouput ports. (b) Measurement setup for the copolar and cross polar transmissions. 34
3.14 Experimental and simulated reflections at the output ports of the OMT . . . 35
3.15 Experimental and simulated copolar transmissions of the OMT 35
3.16 Experimental and simulated cross polar transmissions of the OMT 36
3.17 Experimental and simulated transmissions between output ports of the OMT 36
3.18 Model of the WR10 meander in HFSS 36
3.19 Alluminium meander 37
3.20 Copper meander 37
3.21 Waveguide meander measurement setup 38
3.22 Meander inside the cryostat 39
3.23 Measured tranmissions for the meander. The mylar film and the short circuit at the end of the meander generates a cavity resonator which enables the presense of a standing wave. 39
3.24 Experimental and simulations results of the conductivity measurements of the aluminium meander 40
3.25 Experimental and simulations results of the conductivity measurements of the copper meander 40
3.26 Experimental and simulated copolar transmissions of the OMT 40

4.1 Scheme of the proposed LO power distribution 43
4.2 Scheme of the hybrid 44
4.3 Example of a air bridge over a CPW line 45
4.4 Lateral view of the air bridges 45
4.5 Example of the use of air bridges 46
4.6 CST model of a 90° bend 46
4.7 CST model of a 45° bend 47
4.8 Reflections from the 90° bend (S11 Parameter) 47
4.9 Reflections from the 45° bend (S11 Parameter) 47
4.10 CST model of the hybrid designed 48
4.11 s11 and s14 parameters of the hybrid 48
4.12 s12 and s13 parameters of the hybrid 49
4.13 CPW to Waveguide transition 50
4.14 Reflections of the CPW to Waveguide transition 50
4.15 Proposed distribution of devices in the basic block of the LO distribution . . 51
4.16 Scheme of the proposed LO distribution network in CST 51
4.17 Reflections at the input of the block 52
4.18 Power transmission to the four mixers 52
4.19 Difference in power injected to the mixers. 52
4.20 New scheme for the power division 53
4.21 Scheme of a wilkinson power divider 54

4.22 Reflections at the input port of the 1:1 Wilkinson 55
4.23 Transmissions to output ports 2 and 3 of the 1:1 Wilkinson 55
4.24 Reflections at the input port of the 2:1 Wilkinson 55
4.25 Transmissions to output ports 2 and 3 of the 2:1 Wilkinson 56
4.26 Reflections at the input port of the 3:1 Wilkinson 56
4.27 Transmissions to output ports 2 and 3 of the 3:1 Wilkinson 56
4.28 Reflections at the input port of the second design of LO distribution network 57
4.29 Transmission to the four mixers of the basic block 57
4.30 Difference in power pumped to the mixers 57
4.31 Electric field lines in the covered CPW line 58
4.32 Transmission line scheme for the calculation of Z_{in} 58
4.33 Scheme of the CPW EBG 59
4.34 Model of the complete model of the $3:1$ Wilkinson power divider 61
4.35 Simulated transmissions to output ports 2 and 3 of the 3:1 Wilkinson 62
4.36 Simulated reflections at the input port of the 3:1 Wilkinson 62

Chapter 1

Introduction

1.1 Background

Astronomical observations can be classified by the frequency of the electromagnetic wave detected, going from Gamma rays to Radio radiation. The Earth's atmosphere absorbs most of the incoming space radiation, leaving only two windows fitting for ground based astronomy, the visible range and the RF and millimetric range (microwave radiation)(Figure 1.1). The former goes from 400 to 800 Terahertz while the latter comprises from a few Gigahertz to the Terahertz. Even thought the existence of these atmospheric windows allows a fraction of the radiation to penetrate the atmosphere, it does not guarantee that astronomical observations can be made anywhere in the planet. There are still a few harmful effects that prevent the radiation coming unscathed from an encounter with our atmosphere. The most important are the astronomical seeing, affecting the visible radiation, and water vapour absorption, affecting microwave radiation. These two phenomenons limit the places suitable for ground based astronomy.

The Chajnantor plateau in the Atacama desert stands out as one of the best locations for performing radio astronomy in the planet. This is because most of the detrimental effects of the atmosphere are removed by dry conditions and high altitude. Proof of this is the great atmospheric transmission at millimetric frequencies (Figure 1.2).

Due to these particular conditions the Chajnantor is, and will be, home to a high number of observatories. The current operating telescopes in the plateau are the Atacama Submillimeter Telescope experiment, Atacama Pathfinder Experiment (APEX) , Atacama Cosmology Telescope (ACT), NANTEN2 telescope and Atacama Large Millimeter/Submillimeter Array (ALMA). Moreover, there are several observatories that will be built in the plateau. One of the most important is the Cerro Chajnantor Atacama Telescope - Prime (CCAT-p) which is a 6 meter diameter telescope at 5600 m.a.s.l. It will feature a novel crossed-Dragone optical design and is specifically designed to measure very distinct celestial phenomena [1].

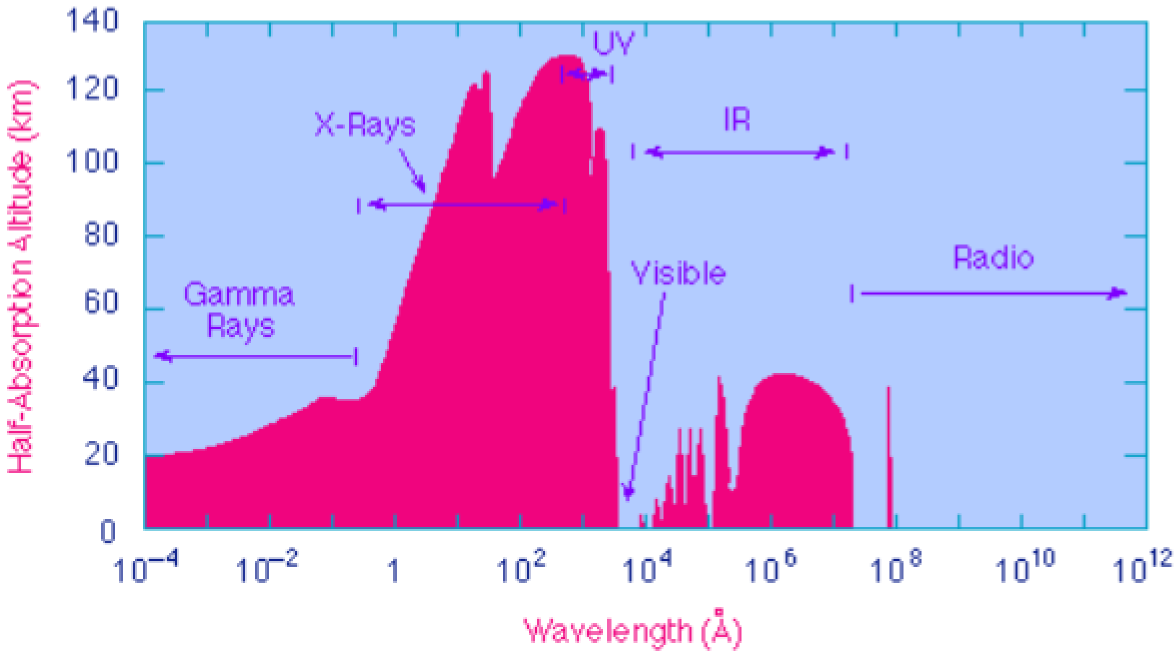

Figure 1.1: Half absorption altitude of the electromagnetic spectrum on earth. It represents the height at which half of the radiation is absorbed by the atmosphere [2].

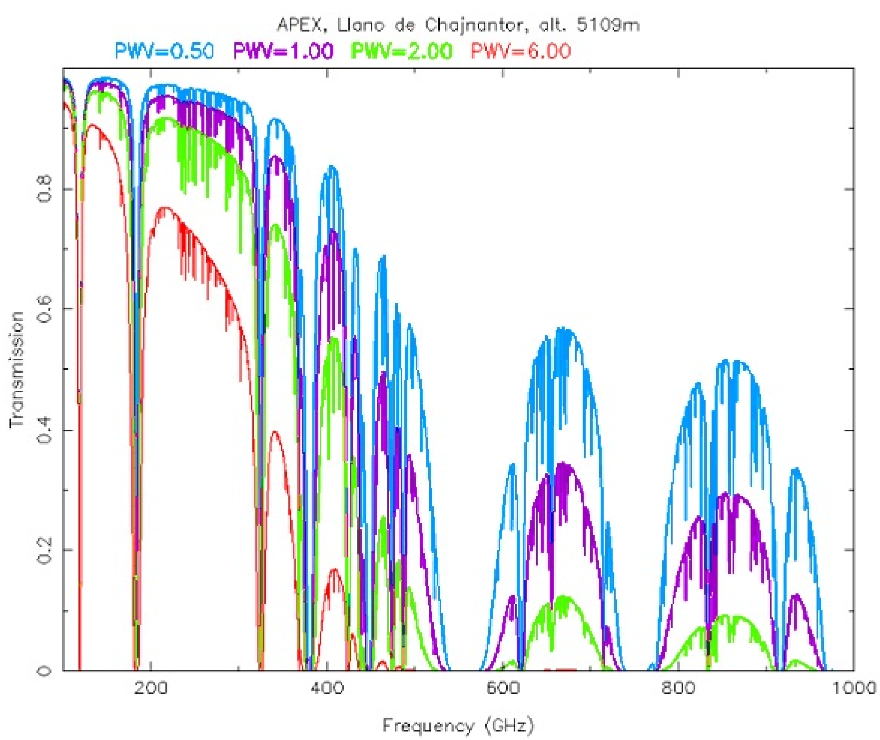

Figure 1.2: Atmospheric transmission at the Chajnantor plateau at different concentrations of precipitable water vapor [3].

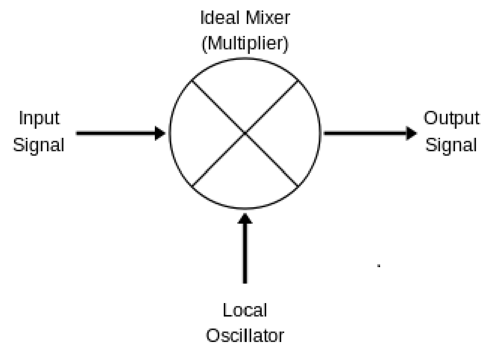

Figure 1.3: Schematic of an ideal mixer.

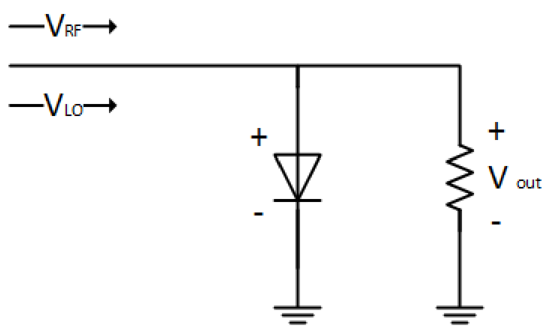

Figure 1.4: Basic mixer example. Here the diode acts like the non linear device and mix the two signals.

1.2 Heterodyne Receivers

The process of heterodyning consist in shifting the signal of concern to more convenient frequencies, keeping the amplitude and phase unaltered. The goal of this method is to enable the processing of the signal by the commercial electronics available.

The one essential element for heterodyne receivers is the mixer. This component carries out the shifting of the frequency of the signal (Figure 1.3). The output signal of this device is a composite of two signals with frequency $f_1 = f_{in} - f_{LO}$ and $f_2 = f_{in} + f_{LO}$. Any non linear device could be used as a mixer, the most basic configuration for an heterodyne receiver consist in a diode and a resistance (Figure 1.4). The LO signal turns on and off the diode resulting in the "cut off" of the RF signal and, thus, the signals are mixed.

However the I-V curve of the diode is not ideal and there appear several other mixing products that have a harmful effect on the output signal. To deal with these problem a more elaborated receiver is needed. The double sideband(DSB) receiver is the most simple of the receivers used (Figure 1.5). This receiver mix both the lower and upper sidebands in the intermediate frequency output, thus increasing the noise in it. To avoid excess the noise in the intermediate frequency, the single sideband (SSB) configuration is conceived (Figure 1.6). This receiver has a filter before the mixer that eliminates one of the sidebands. Hence, the noise in this configuration is lower than the DSB. However this reduction in noise comes at the cost of

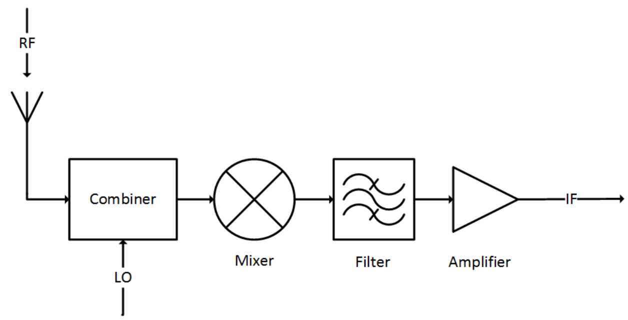

Figure 1.5: Schematic of a double sideband receiver. Here the astronomical signal (RF) is combined with the Local Oscillator signal (LO) and it is filtered and amplified before continuing to be processed by the electronics of the backend.

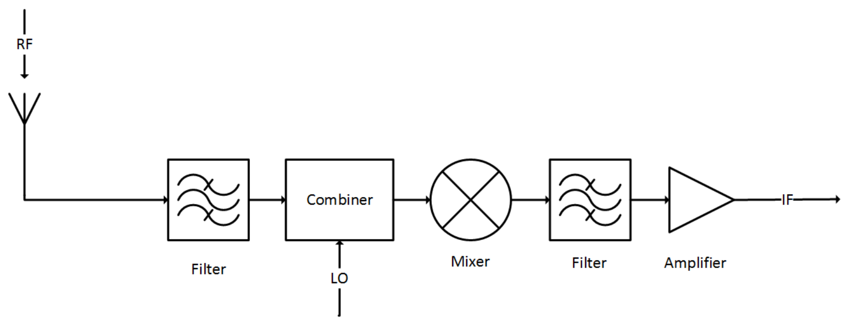

Figure 1.6: Schematic of a Single Sideband receiver. Here the RF signal is filtered to remove one of the sidebands before the mixing with the LO.

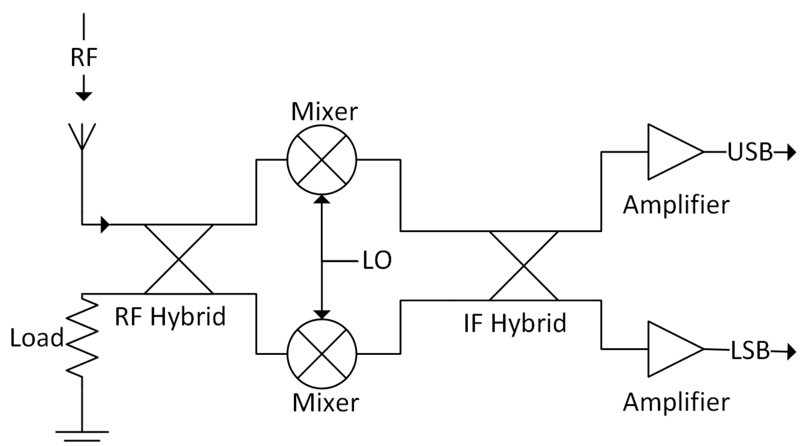

Figure 1.7: Schematic of a sideband separating receiver. The RF is divided in equal parts with a offset of 90° and mixed with the LO that is divided in phase to the two mixers. Finally the signals are combined again in the IF 90° Hybrid and amplified before continuing to the backend

losing half the bandwidth. Finally, the sideband separating configuration (2SB) (Figure 1.7) separates the sidebands (hence the name) and allows its processing separately. Nevertheless the receiver needed for such processing is more complex than the DSB ans SSB configurations and the rejection of the sideband depends on the imbalances in amplitude and phase.

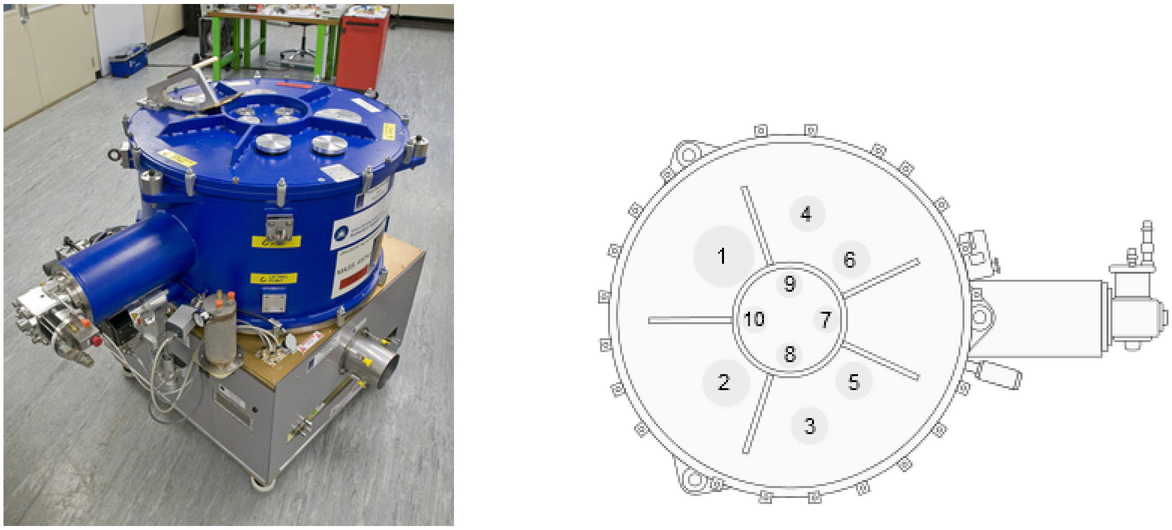

(a) (b)

Figure 1.8: (a) Front End at the Operational Support Facilities of ALMA (b) Superior view of the cryostat. It can be noted that the lower the band, the bigger the space needed to house the complete receiver cartdrige. *Credit: M. Mattamala*

1.3 Modern Heterodyne Receivers

1.3.1 Single pixel receivers

The single pixel receiver is the prevalent type of microwave and radio detector. It has been around since Reginald Fessenden invented the process of heterodyning for radio telecommunications in 1904 [4]. However, it was not before Karl Jansky discovered the radio emission coming from the galactic center that heterodyne receivers were used for astronomical observations [5]. Since then it has been widely used for astronomical observations culminating in the ALMA observatory, the largest astronomical facility in the world. ALMA was developed by a worldwide partnership between the European Organisation for Astronomical Research in the Southern Hemisphere (ESO), the U.S. National Science Foundation (NSF) and the National Institutes of Natural Sciences (NINS) of Japan in cooperation with the Republic of Chile. ALMA, located in the Chajnantor plateau, operates with 54 12-meter antennas and 12 smaller 7-meter antennas [6]. The front end of each of these 66 antennas operates in 10 observation bands (Figure 1.8) using single pixel receivers covering from the lower limit in Band 1 (35 - 50 GHz) reaching the terahertz regime with Band 10 (787 - 950 GHz). Table 1.1 displays the band distribution.

1.3.1.1 ALMA Receivers

The architecture of an ALMA receiver consist of several stages. First, it comes the the feed horn that couples to the RF signal given by the telescope optics. Depending on the available technology of the next device is either an OMT or a Low Noise Amplifier (LNA).

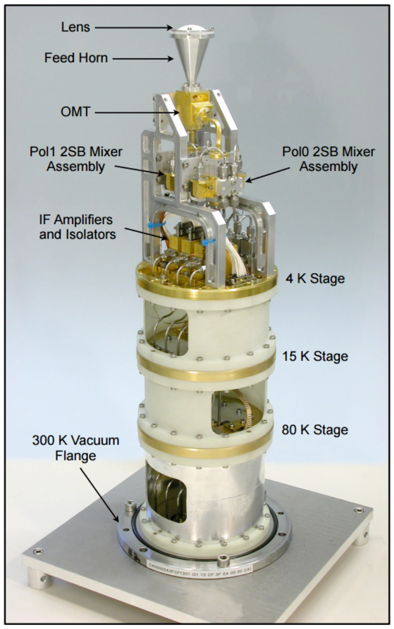

(a)

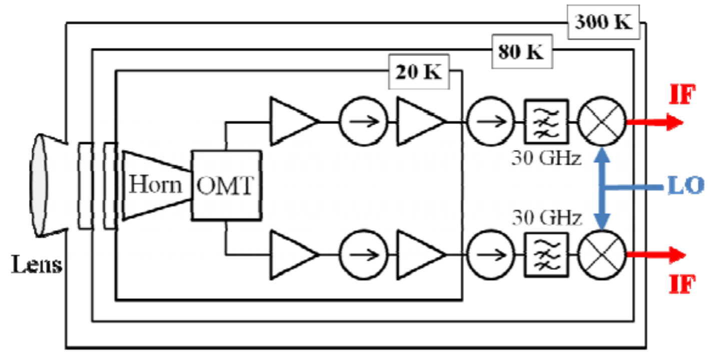

(b)

Figure 1.9: ALMA Band 3 cartridge . The three cryogenic stages are present in the ten bands.(a) Example of ALMA Band 3 cartridge[7]. (b) Schematic of ALMA Band 1 receiver

The uniqueness of an OMT is that it allows the study of both orthogonal polarizations of the signal, assuring that no information is lost in the process. After the OMT the signals are delivered to non linear devices to carry out the mixing process. After the heterodyning, the signal is amplified and delivered to the electronics in the back end to be digitalized. Figure 1.9 shows an example of the ALMA Band 3 cartdrige and the schematics of the ALMA Band 1 receiver.

1.3.1.2 ALMA Band 2+3

From table 1.1 it can be noted that Bands 2 and 3 overlap in the frequency range. This gives the possibility to create a receiver capable of merging Bands 2 and 3 on a single element. From the astronomical point of view, this is a very attractive possibility as it would release space from one of the replaced bands giving the opportunity to place new receivers, as a potential band 11. However, to develop such a receiver supposes a vast technical effort as the fractional bandwidth of the Band 2+3 (56.6 %) is greater than any of the other bands.

Among the science cases to perform with Band 2+3 we have the following. [8, 7]

- Deuterium J= 1→ 0 transition will enable studies of stellar cloud evolution and chemical fractionation of interstellar material.
- DCO + J = 3-2 line traces the Helium line o snow line of CO on protoplanetary disks.
- H2CO + Transition lines helps to trace galactic structures and it is a prebiotic molecule
- Red-shifted lines of CO and HCN emission lines required for galactic evolution studies

Table 1.1: Band distribution of ALMA

Band	Frequency [GHz]	Receiver Technology	Fractional Bandwidth %
1	31 - 45	HEMT	37.48
2	67 - 90	HEMT	29.61
3	84 - 116	SIS	32.42
4	125 - 163	SIS	26.62
5	162 - 211	SIS	26.5
6	211 - 275	SIS	22.42
7	275 - 373	SIS	30.59
8	385 - 500	SIS	26.21
9	602 - 720	SIS	17.92
10	787 - 950	SIS	18.85

1.3.2 Multi pixel receivers

One of the most important features of a receiver is the sensitivity since it determines the quality of the observations made. The reason is that radio astronomical sources do not emit high energy radiation. Furthermore, the little power emitted by the source is decreased even more considering the fact that the source is far away from the Earth. There are several measures that can result in an increased sensitivity of the receiver. The most relevant are removing the effect of the atmosphere and decreasing the noise of the receiver [9].

Nowadays, modern heterodyne receivers, thanks to the advent of superconductive detectors and improved semiconductor amplifiers, have achieved sensitivity levels close to the theoretical limit for heterodyne detection [10]. This renders the increase the number of independent detectors as the only way to improve the productivity of a receiver. However, incrementing the number of detectors is not an small undertaking. The complexity of submillimeter and terahertz receivers is the main reason why there are mainly single pixel receivers and only in the last two decades multipixels receivers have arisen.

Among the first heterodyne arrays to be developed is one with eight cooled Schottky diode mixer (pixels) fabricated by the National Radio Astronomy Observatory (**NRAO**) at Kitty Peak, Arizona on 1988 [11].

A decade later, the National Astronomical Observatory of Japan (NAOJ) installed the SIS 25-**BE**AM **A**RRAY **R**ECEIVER **S**YSTEM (**BEARS**) on the Nobeyama Radio observatory (NRO), Japan. The BEARS receiver operates on the 82 - 116 GHz band with SIS mixers in a DSB configuration [12].

In 1999, The **CHAMP** receiver was installed at the Caltech Submillimeter Observatory on Mauna Kea, Hawai [13]. It was a 4×4 pixel array operating in the 625 μm atmospheric window. CHAMP possessed two sub arrays of 8 pixels for each polarization. In 2007 CHAMP was upgraded to CHAMP$^+$ and installed at APEX [14]. It featured two brand new arrays of 7 pixels each to cover the 660 and 850 GHz atmospheric windows.

A year later, on 2000, **PoleStar** [15], a four channel receiver, was located in one of the most extreme observatories, the AST/RO located on the Antarctic plateau. The University of Arizona conceived the receiver to trace neutral carbon and carbon monoxide in the 800-820 GHz band.

In 2001, IRAM entered the heterodyne array field with his own receiver **HERA** [16], placing it on the 30 m telescope on Pico Veleta, Spain. HERA worked in the 215-270 GHz band in a dual polarization configuration with 9 pixels fashioned in a square array.

The same year, KOSMA presented the dual band receiver **SMART** [17], featuring a 2×4 pixel array covering the 460-490 and 800-880 GHz bands working in a dual band configuration. It was installed on the KOSMA 3m telescope on Gornergrat, Switzerland in 2001 and in 2008 was moved to Pampa la Bola, Chile.

DesertStar is a hexagonal 7 pixel receiver, developed by the University of Arizona to execute observations on the 345 GHz atmospheric window [18]. It begun its operations on the Henrich Hertz Telescope on 2003. DesertStar benefited from the background given by the development of PoleStar and SMART as it used a phase grating made by KOSMA to optically multiplex the Local Oscillator signal.

The University of Cambridge, in collaboration with several other scientific entities, developed **HARP** for the 325-375 GHz band and was installed at the James Clerk Maxwell Telescope on Mauna Kea [19], Hawaii in 2005. It has a 4×4 mixer array operating in a single sideband configurations using an interferometer for the sideband filtering.

The Stratosferic Terahertz observatory (**STO**) [20], is a long-duration ballon-borne observatory. It was launched for the first time in January 2012 for 14 days from Mc Murdo, Antartic Station. The instrument currently posses a 0.8 m main dish and a three band array, 2×1.46 THz, 2×1.9 THz and 1×4.7 THz HEB mixers [21].

SuperCam, with its 8×8 array, was the first receiver to step over the 50 pixel boundary [22]. It was installed on the HHT on Mount Graham, Arizona on 2009 to observe in the 870 μm (350 GHz) window. The focal plane of SuperCam is fashioned differently from other arrays as it was not build from individual pixels. Instead it displayed an array built from 8 monolithic blocks, each of them enclosing 8 pixels.

IRAM continued its operations on the 30 meter telescope, on Pico Veleta, Spain, with two new receivers for the **2** and **3 mm** bands [23, 24], installed on 2010 and 2012, respectively. The 2 mm band receiver possess 4 pixels arranged in a linear manner, meanwhile the 3 mm band receiver comprises an array of 5×5 double-polarization pixels.

On 2011 the University of Arizona,in collaboration with other institutes, proposed the **KaPPa** receiver as a proof of technology for future heterodyne arrays with $\sim$ 1000 pixels [25]. It has been designed for the 660 GHz atmospheric window and in features a 2D vertically stacked micromachined mixer scheme.

Contemporary to the **KaPPa** and IRAM 30 m receivers, NRAO conceived the K-band Focal Plane Array (**KFPA**) with an hexagonal array of seven pixels, working in a double circular polarization architecture each [26].

The **Sardinia** telescope, managed by the Instituto Naziolane di Astrofisica (INAF), begun its operation on the first quarter of the 2014 [27]. It was designed to house a different instruments, among them pixel arrays for the K, Q and S bands, with 7, 19 and 5 pixels each, operating in a dual polarization scheme. Currently, only the K band has been commissioned meanwhile the Q and S band are under construction.

Argus is a 16 pixel array for the 85 - 116 GHz band, installed on 2014 on the Green Bank Telescope, West Virginia [28]. Its focal plane is an 4×4 arrays composed by four subunits of four individual MMIC receivers each and a multilayer routing board. The front end design is scalable, intended for future arrays with increased number of pixels.

In November 2016 **upGREAT** was finally commissioned [29]. It is designed to operate at the Stratospheric Observatory for Infrared Astronomy (SOFIA) and possess two arrays operating at 1.9 with 2×7 pixels and 4.7 THz with 7 pixels.

1.4 CCAT-p

The CCAT consortium begun on late 2003 with a partnership workshop in Pasadena between the California Institute of Technology, NASA Jet Propulsion Laboratory and Cornell University. The site selection, design development and consolidation of the consortium took place between the years 2007 to 2009. University of Colorado, Canadian Consortium, the Cologne-Bonn groups and Associated Universities were included in the partnership. However on fall of the year 2014 Caltech leaves the association. And in the year 2015 the proposal of a 25-meter telescope is submitted and declined (Figure 1.10).

After this drawback, the project was reformulated and renamed as CCAT-p, where the p stands for *pathfinder*. The design currently under analysis is specially designed for the targeted science cases. It features a six-meter off-axis crossed-Dagone design and a novel AZ-EL mount [30, 31] and a surface accuracy 10μm (7 μm goal) (Figure 1.11).

1.4.1 Science with CCAT-p

The main science drivers behind the CCAT-p are [33]

- **kinectic Sunyaev-Zel'dovich effect** (kSZ) [34]. It is a cosmological phenomenon involving distortions of the CMB photons caused by interactions with the hot interstellar medium. There are three kinds of interaction predicted.
  - Thermal (tSZ): Due to random thermal motions of scattering electrons. It has a strong spectral signature.
  - Relativistic (rSZ): Due to populations of relativistic electrons. It has a small spectral correction.
  - Kinetic (kSZ): Due to interactions with group velocity relative to the CMB frame. It has traces of the CMB spectrum.

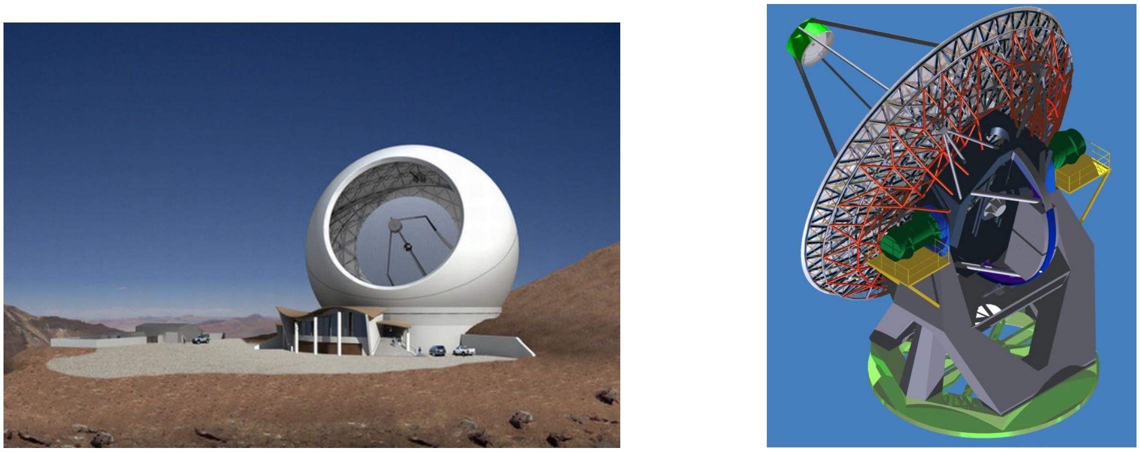

(a) (b)

Figure 1.10: (a) Impression of the first proposed desing for CCAT on the Cerro Chajnantor *Credit: CCAT/Cornell* (b) Schematic of the mount proposed for the 25 meter telescope [32]

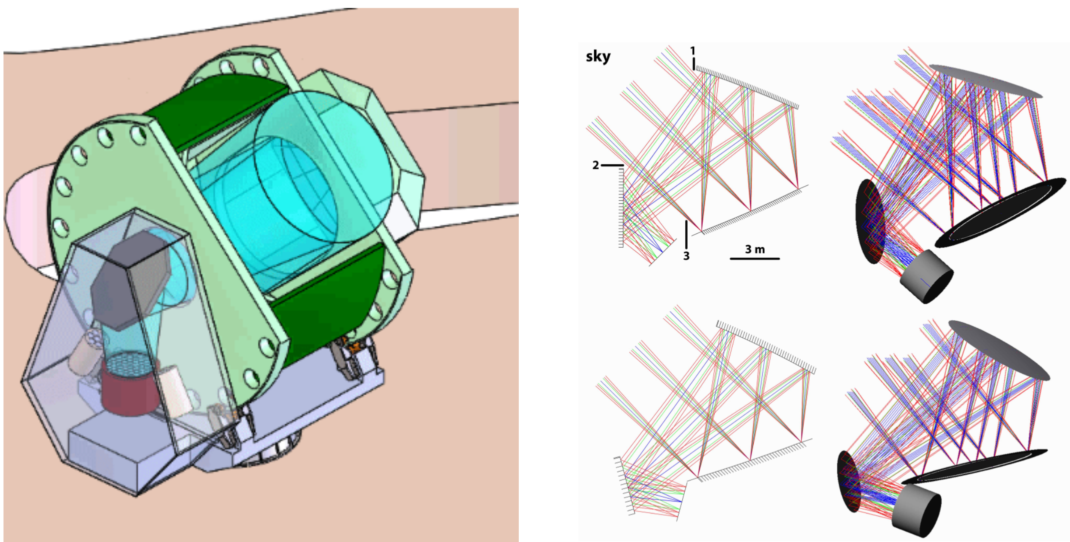

(a) (b)

Figure 1.11: CCAT-p, the current design under discussion (a) Impression of the optics used and its allocation within the telescope *Credit: CCAT* (b) Optical path of the incoming space radiation in the off-axis mirror design [30]

To perform detection of the kSZ is necessary to remove the other two kinds, tSZ and rSZ. Moreover the CMB, submillimeter and radio sources needs to be excluded as well. The inspection of this phenomena will yield important information over the evolutions of galactic clusters, the behaviour of gravity at large scales and it will shed some light on the dark energy. Furthermore, it will enable approximations and constrains on the mass of neutrinos.

- **Intensity Mapping of [CII] from the Epoch of Reionization** (IM/EOR) [35]. Intensity mapping is an observational technique to survey large scales structures of the universe. The most popular are the temperature and polarization of the CMB. Spectral line intensity mapping yields 3D spatial information, allowing the study of process of structure formation and the absorption/emission fluctuations can be used as a probe to study the dark matter density variations. The 21 cm line of the hydrogen was intended to serve such purpose. However the direct detection of it is very difficult as it is sensitive to the intergalactic medium (IGM). Instead, observing the stronger emission line of 158 μm of [CII] at red-shifts $z = 6 - 8$ is much easier and does not requires great astronomical facilities. [CII] has the advantage that allows direct mapping of the sources of reionization.

- **Galactic Ecology of the Dynamic Inter Stellar Medium** (GEco) [36] The study the process of star formation and how it is affected by its environs demands the analysis of the fine spectral lines of several tracers, such as [CI], [CII], [OI], and [NII] as well as medium/high excitations of CO. These species are agents of cooling in star formation clouds so they act as tracers of the process carried out in molecular clouds.
- **Stage IV ground-based CMB observatory** This is not an immediate science objective for CCAT-p. However the opportunity presented by CCAT-p makes it very attractive to take advantage of it to study the CMB.

The accomplishment of the science demands requires the development of at least three instruments for CCAT-p. The three conceived instruments are [33]

- **PCAM** is a submillimeter, modular, wide field camera originally designed for the CCAT telescope as **SWCAM** and later scaled to CCAT-p. It should be the first light instrument as allows the test and verification of the optical system efficiency plus serving the study of **kSZ** and **GEco**. It has seven interchangeable (except wavelength specific elements) subcameras and it will deliver 1° field of view to each subcamera.
- **CHAI** is a heterodyne receiver able to perform simultaneous observations in the 370 μm (810 GHz) and 610 μm (492 GHz). Each band is planned to comprise 128 pixels operating in a balanced mixer scheme and to be housed individualy in a separate dewar. Its modular design enables easy changes or upgrades in mixer technology or band.
- **Imaging Spectrometer**. In order to detect the red-shifted 158 μm line of the [CII] an imagin spectrometer is needed. There are various potential schemes to deliver the spectrometer, however, the easiest way is to turn **PCAM** in an imaging Fabry-Perot interferometer.

1.5 Context of this work

This thesis work is immersed in two independent microwave development projects at the Millimeter Wave Laboratory (MWL) at the Astronomy Department, University of Chile and in the I. Physikalisches Institut, University of Cologne.

The work at the MWL is within the Band 2+3 development project. It is intended to demonstrate that the Bands 2 and 3 can be merged in one ultra broadband receiver. The relevance of such project is that ultrabroadband receivers can be manufactured and comply with the stringent requirements established by ALMA.

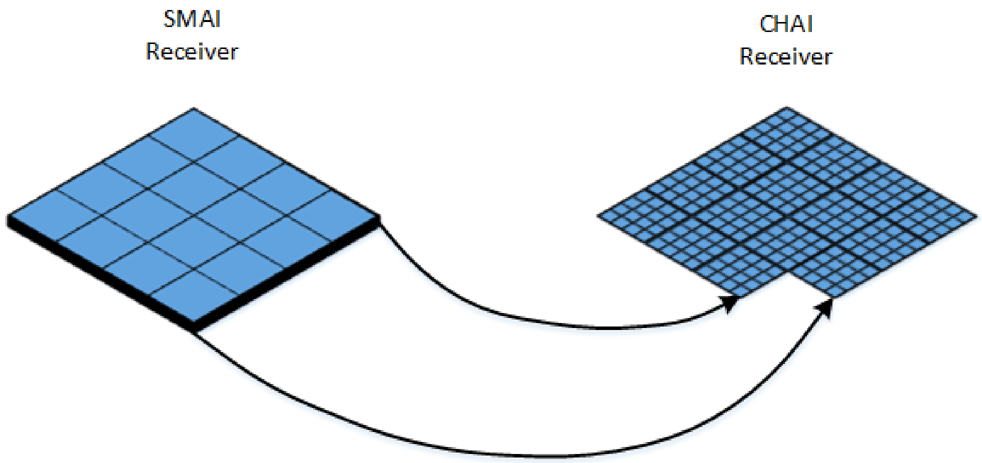

Figure 1.12: SMAI pixel configuration for one band. It can be noted the modular nature of the CHAI receiver , with SMAI serving as the basic block of it.

The second part of this work is immerse in the NANTEN2 instrument upgrade proposal of the SMART receiver. SMART (Sub-millimeter receiver for Two frequencies) consist in 2×4 pixels subarrays [37]. The upgrade proposal has been named SMAI (**SM**ART + CH**AI** = **SMAI**) covering the same frequencies as SMART and having an increased number of pixels, 16 for each band (Figure 1.12). The importance of SMAI in not a merely instrument upgrade as it will serve as a stepping stone and proof of technology for developing the CHAI receiver on CCAT-p.

1.6 Hypothesis

1. The Turnstile-junction OMT is capable of achieving an operational bandwidth of 54% complying with the requirements imposed by ALMA 2+3.
2. The SMAI LO-power distribution based on CPW and waveguide devices will serve as a stepping stone toward the new generation of sub-milimetric arrays with an increased number of pixels overcoming the barrier of 100 pixels.

1.7 Objectives

The main goal of this work is to develop devices suitable for millimeter and submillimeter heterodyne arrays receivers, in particular for band 2+3 of ALMA and for NANTEN2 SMAI receiver.

For band 2+3 an optimized model of an Orthomode Transducer (OMT) is presented. The distinct requirements of the OMT for the whole band 2+3 (67-116 GHz) are

- Reflections at the input and output port should be lower than −20 dB

- Crosspolar transmission should be lower than -40 dB
- Transmission between outputports should be lower than -50 dB

For SMAI we have studied distribution network capable of distributing the LO power to all 16 pixels for the upper band of the SMAI receiver. The specific requirements of this distribution are listed below.

- Frequency range: 800 - 820 GHz
- The imbalance between each mixer can not be greater than -3 dB
- Insertion losses should be lower than -10 dB
- The distribution network must fit in a footprint of 40×40 mm^2

1.8 Scope of this Thesis

Chapter 2 review the main concepts needed to understand the design process behind each model and device. We start with electromagnetic waves theory and move to waveguide transmission to finish with coplanar waveguides. In the chapter 3 we review the the previous OMT design, discuss its performance and the troubles faced on its construction. Subsequently we propose a second design and study its performance. Afterwards we study the conductivity of the constructed waveguides in Aluminium and C14500 Tellurium Copper Alloy. In chapter 4 we present two possible LO-power distribution schemes for the SMAI receiver and

Finally, in Chapter 5 we display the conclusions and achievements of the work executed and discuss possible improvements both in design, construction and measurement of the devices.

Chapter 2

Theory and Design

In this chapter the process of design is reviewed, and the theoretical background needed to understand the development steps taken to achieve the models presented. First, we present the electromagnetic wave and waveguide propagation theory. Subsequently we present the previous OMT design and introduce the modifications leading to the current design. The need to make simulations as precise as possible prompts to the calculation of the effective wall conductivity of the machined waveguides. The second part of this chapter deals with the CPW theory and and the proposed schemes of LO Power distribution.

2.1 Scattering Matrix

The scattering matrix is a pictorial representation of the behaviour of a network seen from any of its N ports. This matrix links the voltages of input and output waves of the N ports of the network (Figure 2.1).

The scattering matrix S is the array of parameters $S_{\mathrm{i}j}$, defined by the ratio between the voltages of the incident wave at the port j and the outcoming wave at port i. A specific case of particular importance is the parameter S_{ii} which represents the reflections at the port i. Then we have

$$\begin{bmatrix} V_1^- \\ V_2^- \\ \vdots \\ V_n^- \end{bmatrix} = \begin{bmatrix} S_{11} & S_{12} & \cdots & S_{1n} \\ S_{21} & S_{22} & \cdots & S_{2n} \\ \vdots & \vdots & \ddots & \vdots \\ S_{n1} & S_{n2} & \cdots & S_{nn} \end{bmatrix} \cdot \begin{bmatrix} V_1^+ \\ V_2^+ \\ \vdots \\ V_n^+ \end{bmatrix} \tag{2.1}$$

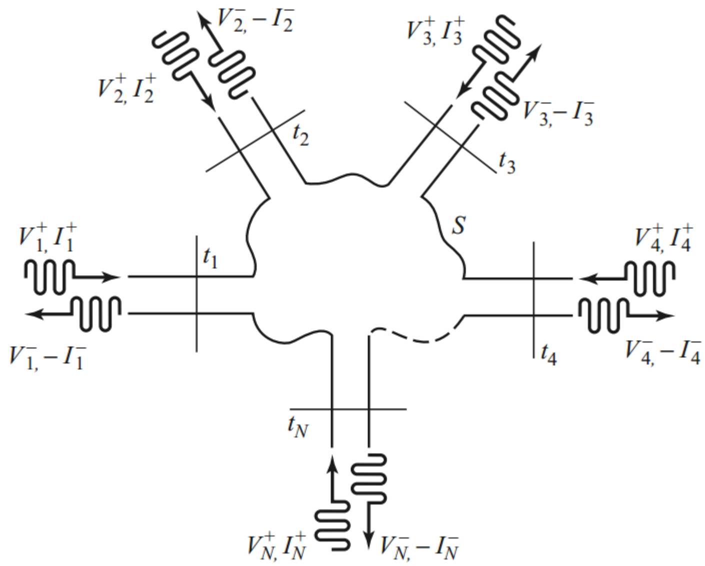

Figure 2.1: Portrayal of an arbitrary network of N ports. V_m^+ is the magnitude of the input wave at the port m and V_n^- is the magnitude of the output wave at the port n [38].

2.2 Electromagnetic Waves

An electromagnetic wave can be defined as an oscillation, characterized by an energy transport propagating through the space-time continuum. James Clerk Maxwell enunciated the relationships that depicts the macroscopic behaviour of the electromagnetic fields [39]. The original Maxwell equations were twelve mathematical statements and Oliver Heaviside was the responsible for reducing them to the four actual known vectorial equations [40],

$$\vec{\nabla} \times \vec{\mathcal{E}} = -\frac{\partial \vec{\mathcal{B}}}{\partial t} \tag{2.2}$$

$$\vec{\nabla} \times \vec{\mathcal{H}} = \frac{\partial \vec{\mathcal{D}}}{\partial t} + \vec{\mathcal{J}} \tag{2.3}$$

$$\vec{\nabla} \cdot \vec{\mathcal{D}} = \rho \tag{2.4}$$

$$\vec{\nabla} \cdot \vec{\mathcal{B}} = 0 \tag{2.5}$$

with $\mathcal{E}$ is the electrical field, $\mathcal{B}$ the magnetic field , $\mathcal{H}$ the magnetic field intensity, $\mathcal{D}$ the Electrical displacement field, $\mathcal{J}$ is the electrical current density and ρ is the charge density in the volume. From these relationships it is possible to predict the propagation of electromagnetic waves. Analysing the sinusoidal regime and using the phasor form of the fields in a linear, homogeneous, isotropic and free of electromagnetic sources region, eqs. 2.2 and 2.3 reduce to

$$\nabla^2 \vec{E} + \omega^2 \mu \varepsilon \vec{E} = 0. \tag{2.6}$$

Equation 2.6 is known as the *Wave equation*, or *Helmholtz equation*, for $\vec{E}$. An analogous equation for $\vec{H}$ can be achieved in the same manner

$$\nabla^2 \vec{H} + \omega^2 \mu \varepsilon \vec{H} = 0. \tag{2.7}$$

The constant $k = \omega\sqrt{\mu\varepsilon}$ is the propagation constant of the medium. Separating the laplacian in its rectangular components provides

$$\frac{\partial^2 \vec{E}}{\partial x^2} + \frac{\partial^2 \vec{E}}{\partial y^2} + \frac{\partial^2 \vec{E}}{\partial z^2} + k_0^2 \vec{E} = 0. \tag{2.8}$$

This equation applies for every rectangular component of $\vec{E}$,

$$\frac{\partial^2 E_{\mathrm{i}}}{\partial x^2} + \frac{\partial^2 E_{\mathrm{i}}}{\partial y^2} + \frac{\partial^2 E_{\mathrm{i}}}{\partial z^2} + k_0^2 E_{\mathrm{i}} = 0. \tag{2.9}$$

where $\mathrm{i} = x, y, z$. Equation 2.9 is known as the *Helmholtz* equation and its solutions outline the electromagnetic waves in the medium.

2.2.1 Free space propagation of electromagnetic waves

A simple field configuration, or propagation mode, which satisfies the Helmholtz equation in free space is the *Transverse Electromagnetic* or *TEM* mode. It is defined by having no fields components in the direction of propagation (Figure 2.2a). Furthermore, if the geometrical places of constant phase are flat and parallel to each other, the wave is a plane wave (Figure 2.2b). Furthermore, if the transverse fields are invariant in the planes of constant phase, we have a uniform plane wave. It can be considered that the wave propagates in the $\hat{z}$ direction which reduces eq. 2.9 to

$$\frac{\partial^2 E_x}{\partial z^2} + k_0^2 E_x = 0. \tag{2.10}$$

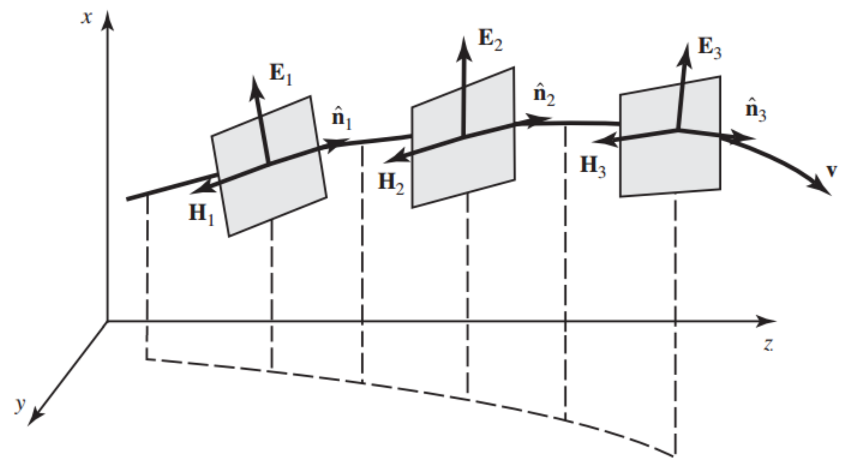

(a) Scheme of a TEM mode

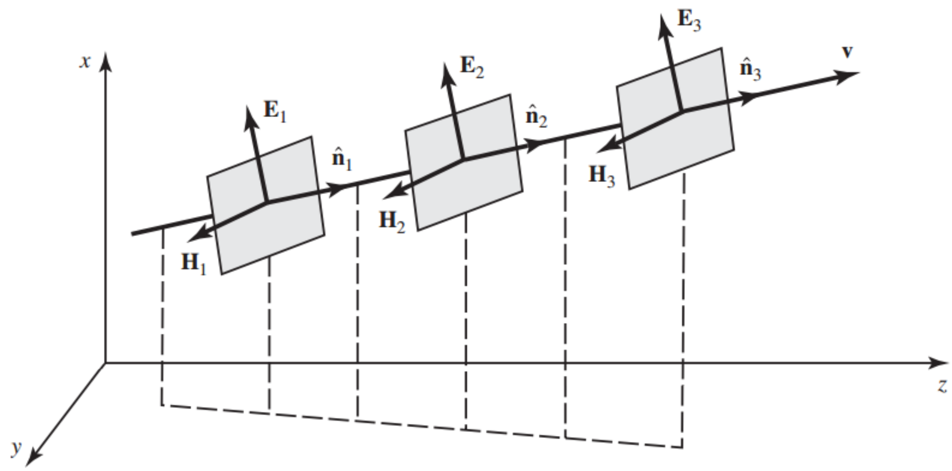

(b) Sketch of a plane wave

Figure 2.2: Basic propagation modes configurations [41]. a)TEM mode. It can be noted that the planes of constant phase are not parallel to each other. (b) If the constant phase planes are parallel , then it determines a plane wave.

One solution for 2.10 is

$$E_x(z) = E^{+}\mathrm{e}^{-jk_0 z} + E^{-}\mathrm{e}^{jk_0 z} \tag{2.11}$$

2.2.2 Polarization of a wave

The polarization of a wave is defined as the orientation of the electric field vector [42]. Mathematically, an arbitrary electromagnetic wave always can be expressed as the addition of two orthogonal waves,

$$\vec{E} = E_{\parallel}\,\mathrm{e}^{\vec{\gamma}\cdot\vec{r}}\ \ \widehat{\mathrm{e}}_{\parallel} + E_{\perp}\,\mathrm{e}^{\vec{\gamma}\cdot\vec{r}}\ \ \widehat{\mathrm{e}}_{\perp}\,\mathrm{e}^{-j\Delta\phi} \tag{2.12}$$

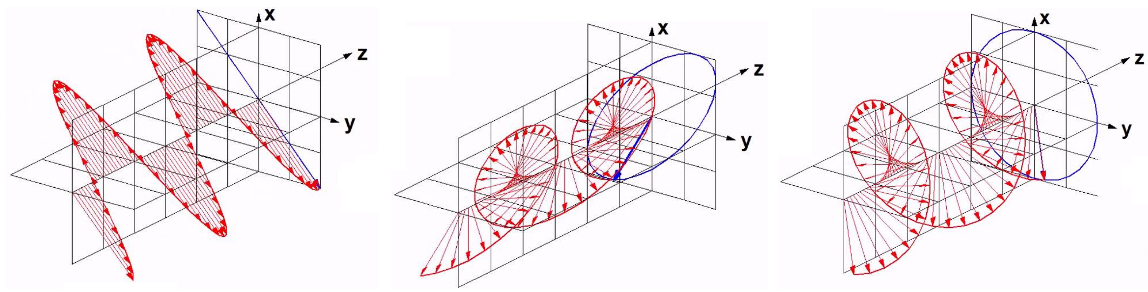

(a) Lineal polarization (b) Eliptical polarization (c) Circular polarization

Figure 2.3: Types of polarization .

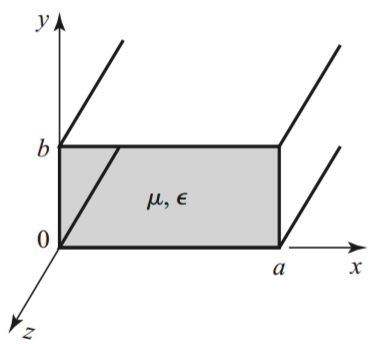

Figure 2.4: Geometry of a rectangular waveguide [38].

where the parameters that define the polarization are the phase offset between components ($\Delta\phi$) and the magnitude of the fields. The polarization can be of three basic kinds, Linear, elliptical and circular, with the latter being a particular case of the former. When the phase offset is zero or some multiple of π the polarization is linear (Figure 2.3a). On the other hand if the phase offset is $\Delta\phi \neq 0$ the wave is said to have an elliptical polarization (Figure 2.3b). Now if $\Delta\phi = \pm\frac{\pi}{2}$ and $E_{\parallel} = E_{\perp}$ the wave has a circular polarization and the sign of the offset gives the sense of rotation of the vector (Figure 2.3c).

2.3 Electromagnetic Propagation in Hollow Waveguides

2.3.1 Waveguides

Waveguides are a particular kind of transmission line, characterized by the propagation of waves through a hollow conductor. Originally it was believed that the existence of electromagnetic waves in hollow pipes was impossible [40]. Nevertheless its existence in rectangular and circular cross sections was mathematically proven by Lord Rayleigh in 1897 [43].

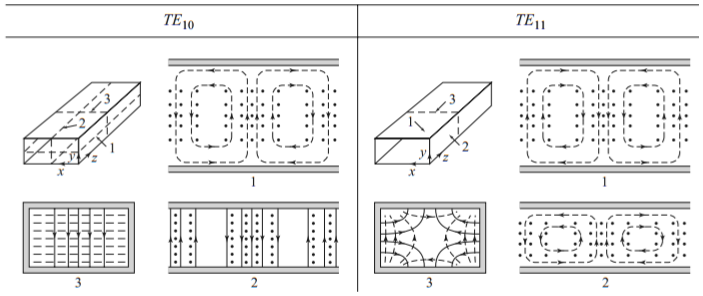

Figure 2.5: TE mode field lines [38]

2.3.1.1 Rectangular waveguides

The geometry of a rectangular waveguide is shown in figure 2.4. The larger side of the waveguide goes on the $\hat{x}$ axis so that $a > b$. For the sake of the analysis, no losses in the waveguide were taken into account.

TE Modes

The waveguide TE modes posses the particularity that the electric field has only transversal components, i.e. $E_z = 0$. Meanwhile H_z must comply with

$$\left(\frac{\partial^2}{\partial x^2} + \frac{\partial^2}{\partial y^2} + k_c^2\right) h_z(x, y) = 0 \tag{2.13}$$

with $H_z(x, y, z) = h_z(x, y, z)\mathrm{e}^{-j\beta z}$, here $k_c = \sqrt{k^2 - \beta^2}$ is the cutoff wavenumber [38]. The equation 2.13 can be solved by the variable separation method. Solving the new differential equation yields the general expressions of components of the TE_{mn} mode,

$$E_x = \frac{j\omega\mu n\pi}{k_c^2 b} A_{mn} \cos\left(\frac{m\pi x}{a}\right) \sin\left(\frac{n\pi y}{b}\right) \mathrm{e}^{-j\beta z} \tag{2.14}$$

$$E_y = \frac{j\omega\mu m\pi}{k_c^2 a} A_{mn} \sin\left(\frac{m\pi x}{a}\right) \cos\left(\frac{n\pi y}{b}\right) \mathrm{e}^{-j\beta z} \tag{2.15}$$

$$H_x = \frac{j\omega\mu m\pi}{k_c^2 a} A_{mn} \sin\left(\frac{m\pi x}{a}\right) \cos\left(\frac{n\pi y}{b}\right) \mathrm{e}^{-j\beta z} \tag{2.16}$$

$$H_y = \frac{j\omega\mu n\pi}{k_c^2 b} A_{mn} \cos\left(\frac{m\pi x}{a}\right) \sin\left(\frac{n\pi y}{b}\right) \mathrm{e}^{-j\beta z} \tag{2.17}$$

where the propagation constant is $\beta = \sqrt{k^2 - k_c^2} = \sqrt{k^2 - \left(\frac{m\pi}{a}\right)^2 - \left(\frac{n\pi}{b}\right)^2}$ and A_{mn} is a constant. Figure 2.5 displays the field lines of some rectangular waveguide TE modes.

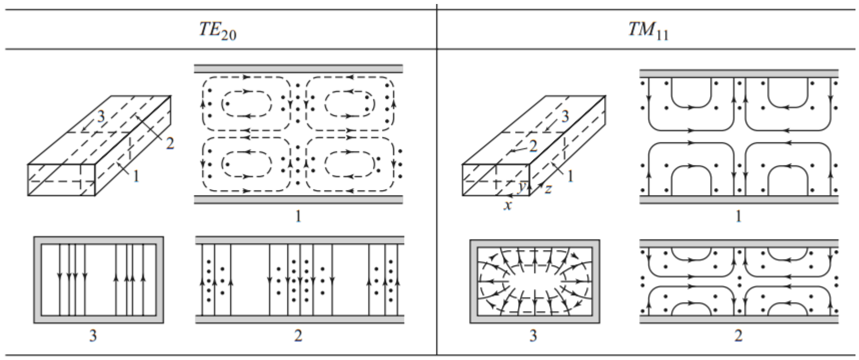

Figure 2.6: Field lines of the TM modes [38]

TM Modes

The waveguide TE modes posses the particularity that the magnetic field has only transversal components, i.e. $H_z = 0$. Meanwhile, E_z must comply with

$$\left(\frac{\partial^2}{\partial x^2} + \frac{\partial^2}{\partial y^2} + k_c^2\right)\mathrm{e}_z(x, y) = 0 \tag{2.18}$$

where $E_z(x, y, z) = \mathrm{e}_z(x, y, z)\mathrm{e}^{-j\beta z}$ and $k_c = \sqrt{k^2 - \beta^2}$ is the cutoff wavenumber. The equation 2.18 can be solved by separation of variables yielding the general expression of the components of the TM_{mn} mode,

$$E_x = \frac{j\omega\mu m\pi}{k_c^2 a} B_{mn} cos\left(\frac{m\pi x}{a}\right) sin\left(\frac{n\pi y}{b}\right)\mathrm{e}^{-j\beta z} \tag{2.19}$$

$$E_y = \frac{j\omega\mu m\pi}{k_c^2 b} B_{mn} sin\left(\frac{m\pi x}{a}\right) cos\left(\frac{n\pi y}{b}\right)\mathrm{e}^{-j\beta z} \tag{2.20}$$

$$H_x = \frac{j\omega\mu m\pi}{k_c^2 b} A_{mn} sin\left(\frac{m\pi x}{a}\right) cos\left(\frac{n\pi y}{b}\right)\mathrm{e}^{-j\beta z} \tag{2.21}$$

$$H_y = \frac{j\omega\mu n\pi}{k_c^2 a} B_{mn} cos\left(\frac{m\pi x}{a}\right) sin\left(\frac{n\pi y}{b}\right)\mathrm{e}^{-j\beta z} \tag{2.22}$$

where the propagation constant is $\beta = \sqrt{k^2 - k_c^2} = \sqrt{k^2 - \left(\frac{m\pi}{a}\right)^2 - \left(\frac{n\pi}{b}\right)^2}$ and B_{mn} is a constant. Figure 2.6 shows the basics TM modes on a rectangular waveguide.

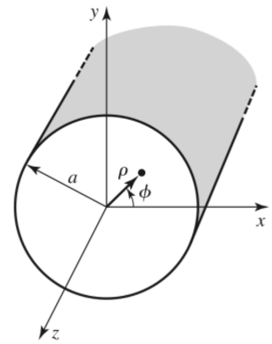

Figure 2.7: Geometry of a circular waveguide [38]

2.3.1.2 Circular waveguides

This kind of waveguide consist in a hollow cilindrical pipe and also supports the existence of TE and TM modes. The geometry is displayed in Figure 2.7.

TE modes

H_z is the solution of the wave equation for TE modes ($E_z = 0$) [38].

$$\nabla^2 H_z + k^2 H_z = 0 \tag{2.23}$$

where $H_z(\rho, \phi, z) = h_z(\rho, \phi)\mathrm{e}^{-j\beta z}$. Recurring to variable separation and determining the solution of the Bessel differential equation gives

$$E_\rho = \frac{-j\omega\mu n}{k_c^2 \rho}(A\cos(n\phi) - B\sin(n\phi))J_n(k_c\rho)\mathrm{e}^{-j\beta z} \tag{2.24}$$

$$E_\phi = \frac{j\omega\mu}{k_c}(A\sin(n\phi) + B\cos(n\phi))J_n'(k_c\rho)\mathrm{e}^{-j\beta z} \tag{2.25}$$

$$H_\rho = \frac{-j\beta}{k_c}(A\sin(n\phi) + B\cos(n\phi))J_n'(k_c\rho)\mathrm{e}^{-j\beta z} \tag{2.26}$$

$$H_\phi = \frac{-j\beta n}{k_c^2 \rho}(A\cos(n\phi) - B\sin(n\phi))J_n(k_c\rho)\mathrm{e}^{-j\beta z}. \tag{2.27}$$

where J_n is the Bessel function of the first kind, J_n' its derivative , $\beta_{mn} = \sqrt{k - \left(\frac{p'_{mn}}{a}\right)}$ and p'_{mn} the root of J_n'. Figure 2.8 shows the field lines of some supported TE_{mn} modes.

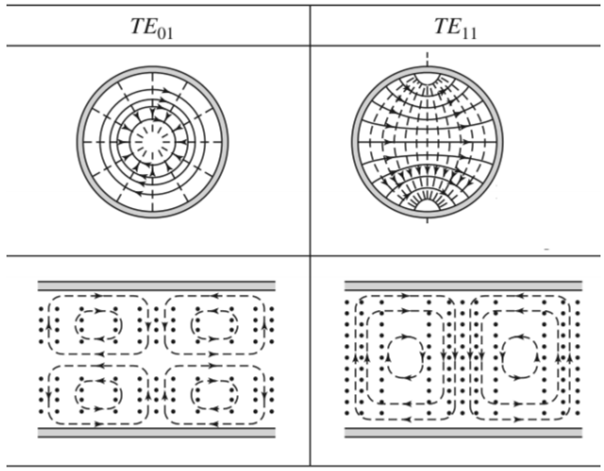

Figure 2.8: TE mode field lines [38]

TM modes

The TM modes have a null transverse magnetic field ($H_z = 0$) and E_z is a solution of the wave equation [38],

$$\nabla^2 E_z + k^2 E_z = 0. \tag{2.28}$$

where $E_z(\rho, \theta, z) = \mathrm{e}_z(\rho, \theta)\mathrm{e}^{-j\beta z}$. Solving in an analogous manner to TE modes yields,

$$E_\rho = \frac{-j\beta}{k_c}(A\sin(n\phi) + B\cos(n\phi))J_n'(k_c\rho)\mathrm{e}^{-j\beta z} \tag{2.29}$$

$$E_\phi = \frac{-j\beta n}{k_c^2\rho}(A\cos(n\phi) - B\sin(n\phi))J_n(k_c\rho)\mathrm{e}^{-j\beta z} \tag{2.30}$$

$$H_\rho = \frac{-j\omega\varepsilon n}{k_c^2\rho}(A\cos(n\phi) - B\sin(n\phi))J_n(k_c\rho)\mathrm{e}^{-j\beta z} \tag{2.31}$$

$$H_\theta = \frac{-j\omega\varepsilon}{k_c}(A\sin(n\phi) + B\cos(n\phi))J_n'(k_c\rho)\mathrm{e}^{-j\beta z} \tag{2.32}$$

where J_n is the Bessel function of the first kind, J_n' its derivative, $\beta_{mn} = \sqrt{k - \left(\frac{p'_{mn}}{a}\right)}$ and p'_{mn} is root of J_n'. Figure2.9 displays the configuration and lines of some TE$_{mn}$ modes.

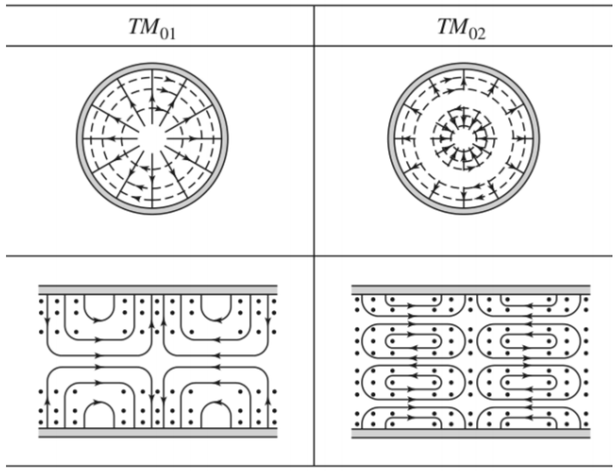

Figure 2.9: TM mode field lines [38]

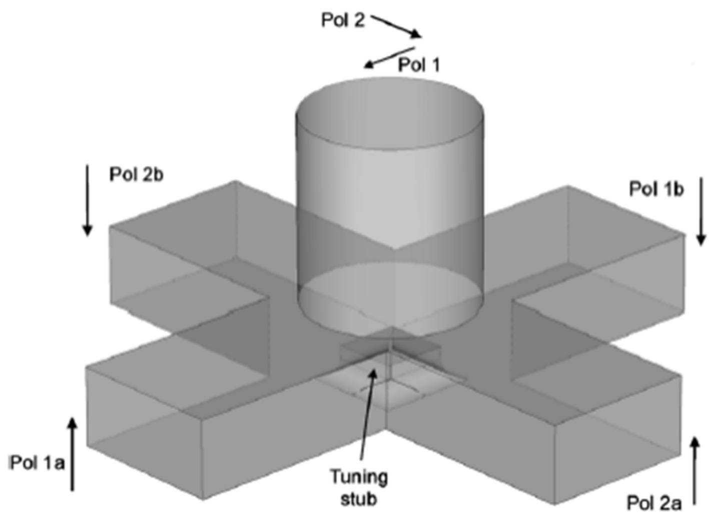

Figure 2.10: Turnstile Junction Model. [45]

2.3.2 Orthomode Transducer

An orthomode transducer (OMT) is an electric device that separates the oncoming wave in two orthogonal polarizations. There are many geometries and design of OMTs, varying from the input port and the way it separates the polarizations to the number of output ports. Seeing this as a problem, Boifot proposed three kinds of OMT [44], depending on the number of output ports on the OMT. The broad bandwidth of ALMA Band 2+3 (56% fractional bandwidth) limits the structure of the OMT. Since the turnstile junction OMT [45] has been proved to achieved fractional bandwidth of 64% [46], it has been chosen as the candidate for the OMT.

2.4 Electromagnetic Propagation in Coplanar Waveguides

Coplanar waveguides (CPW) consist in a dielectric substrate, two semi infinite ground planes and a conductor strip in the middle of the planes. The center strip and the two ground planes are separated by a gap (Figure 2.11). The CPW present some advantages over other kinds of transmission lines. It is easier to manufacture and has lower radiation losses.

In contrast to normal waveguides, this kind of planar structure supports quasi-TEM mode propagation, the most important are even quasi-TEM mode, being the fundamental mode (Figure 2.12), and the odd mode. The even and odd mode are degenerated modes and they can propagate simultaneously.

To understand the characteristics of the transmission lines in an easier way, the CPW can be analysed in a quasi static manner by conformal mappings. Coformal mapping allows to transform the geometry of the waveguide into another whose structure makes the calculations more straightforward. Following the steps proposed in [47], the relevant parameters of the CPW lines can be obtained. Equations 2.33 to 2.35 give the parameters of a CPW with a finite substrate thickness.

$$\lambda_{guided} = \frac{\lambda}{\sqrt{\varepsilon_{eff}}} \tag{2.33}$$

$$Z = \frac{30 \cdot \pi}{\sqrt{\varepsilon_{eff}}} \frac{K'(k_1)}{K(k_1)} \tag{2.34}$$

$$\varepsilon_{eff} = 1 + \frac{\varepsilon_r - 1}{2} \cdot \frac{K(k_2)}{K'(k_2)} \frac{K'(k_1)}{K(k_1)} \tag{2.35}$$

While the independent evaluation of $K(k)$ and $\mathcal{K}'(k)$ can be arduous and cumbersome, their ratio is somewhat easier to compute,

$$\frac{K(k)}{K'(k)} = \begin{cases} \dfrac{\pi}{ln\left[2 \cdot \dfrac{1+\sqrt{k'}}{1-\sqrt{k'}}\right]} & k \in [0\ ,\ 1/_{\sqrt{2}}] \\ \\ \dfrac{ln\left[2 \cdot \dfrac{1+\sqrt{k}}{1-\sqrt{k}}\right]}{\pi} & k \in [1/_{\sqrt{2}}\ ,\ 1] \end{cases} \tag{2.36}$$

$$k_1 = \frac{W}{W + 2s} \tag{2.37}$$

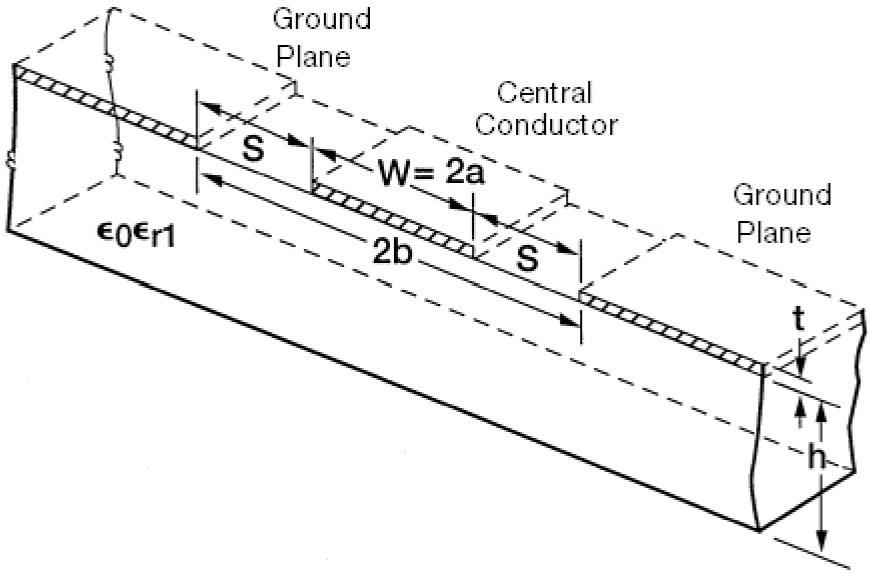

Figure 2.11: Scheme of a CPW with a substrate of finite thickness [48].

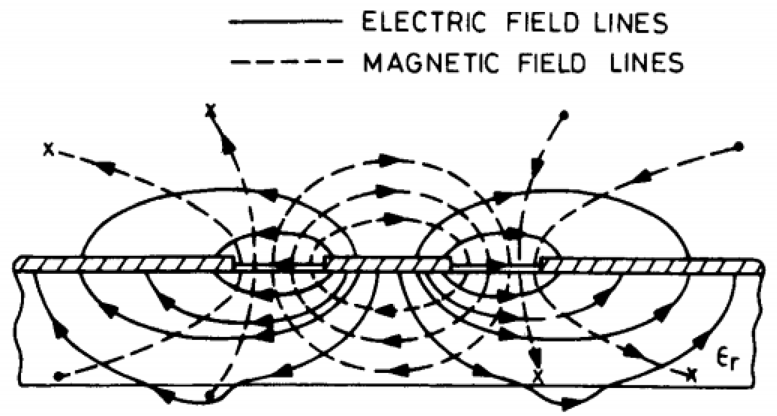

Figure 2.12: Even quasi-TEM mode of a CPW [47]

$$k_2 = \frac{sinh\left(\dfrac{W\pi}{4h}\right)}{sinh\left(\dfrac{\pi(W+2s)}{4h}\right)} \tag{2.38}$$

$$k' = 1 - \sqrt{k} \tag{2.39}$$

The k_1 and k_2 parameters depends of the geometrical parameters of the CPW Eqs. 2.37 - 2.38. The parameter $k' = 1 - \sqrt{k}$ is the complementary modulus. The complete analysis of a CPW line can be found in [49].

2.5 Summary

We have reviewed the theoretical framework required to understand the waveguide and CPW designs and performance of the devices here presented.

Chapter 3

Orthomode Transducer

This chapter begins with the review of the previous OMT design, its performance and the issues faced in its development and construction. It follows with the proposal of a new model and the procedures used to mechanize the waveguide devices, Then it presents the experimental set up used to attain electrical parameters of waveguide components. Subsequently there are presented the characterization of aluminium and copper at different temperatures and the electrical parameters of the OMT.

3.1 Previous OMT Design for ALMA Band 2+3

Within the Millimeter Wave lab some models of OMT have alredy beed developed. Pablo Zorzi developed a dual ridge OMT [50] for the old ALMA Band 1 (35-45 GHz) [51]. There was also a OMT model for ALMA Band 2+3 (Figure 3.1)[52] following the design considerations given in [53] to reduce narrowband spikes in the electrical parameters of the OMT. The OMT was constructed and tested with a "home-made" Scalar Network Analyser with a Vector Network Analyser. Figures 3.2 to 3.5 display the simulations and experimental results of the first version of the OMT. The experimental result show substantial differences with the simulated results. The reflections at the output ports are above -15 dB in several sections of the w band. Moreover, the simulations and the experimental results do not follow the same behaviour across the band (Figure 3.2).Regarding the insertion losses for the horizontal polarization are bellow -2 dB reaching -8 dB (Figure 3.3) at the lower end of the band. On the other hand the cross polar transmissions are lower than -20 dB having an average level of -30.5 dB. The isolation between output ports is also higher than expected with an average of -30 dB, more than 20 dB greater than expected.

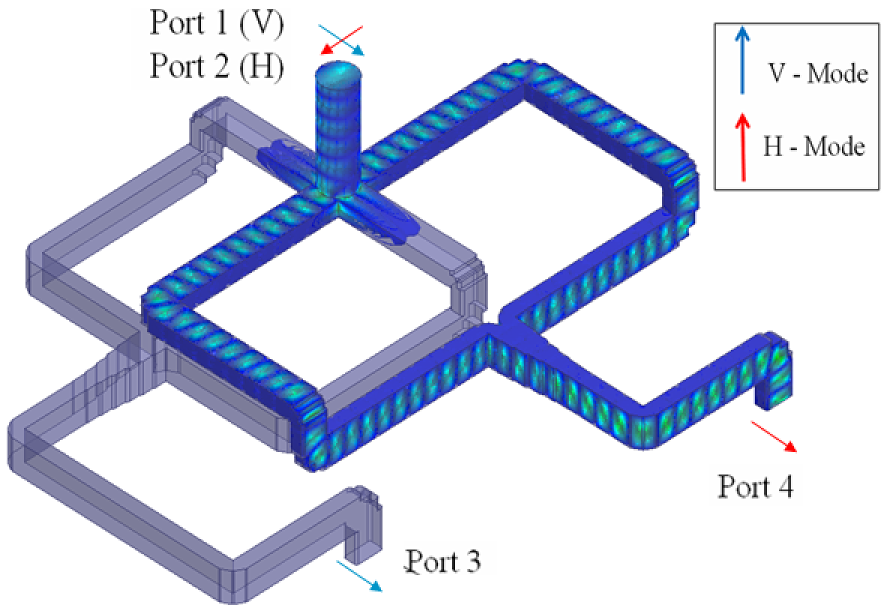

Figure 3.1: Previous design of the OMT.

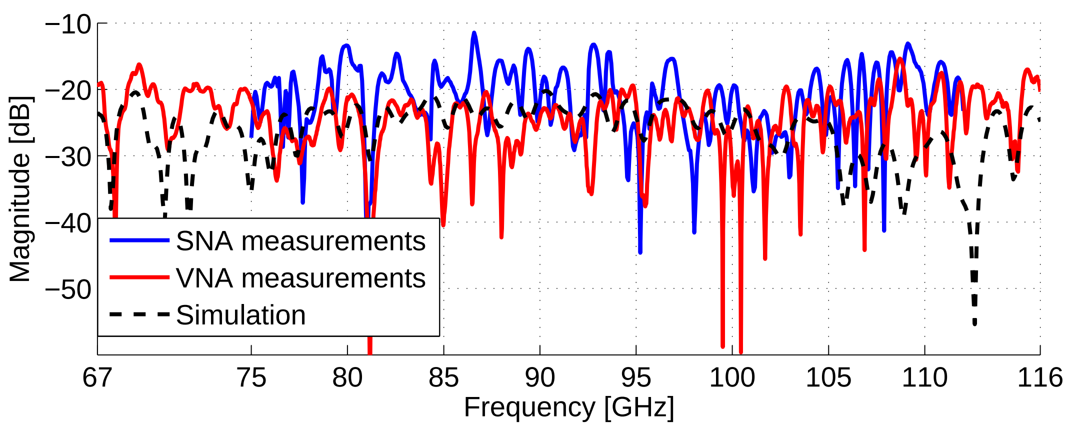

Figure 3.2: Reflections at the input port of the OMT v1.

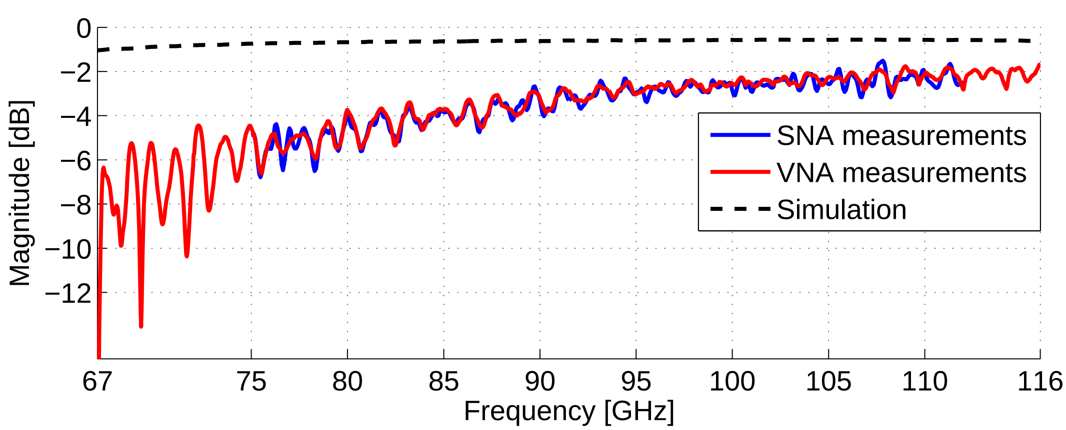

Figure 3.3: Copolar Transmission of the OMT v1

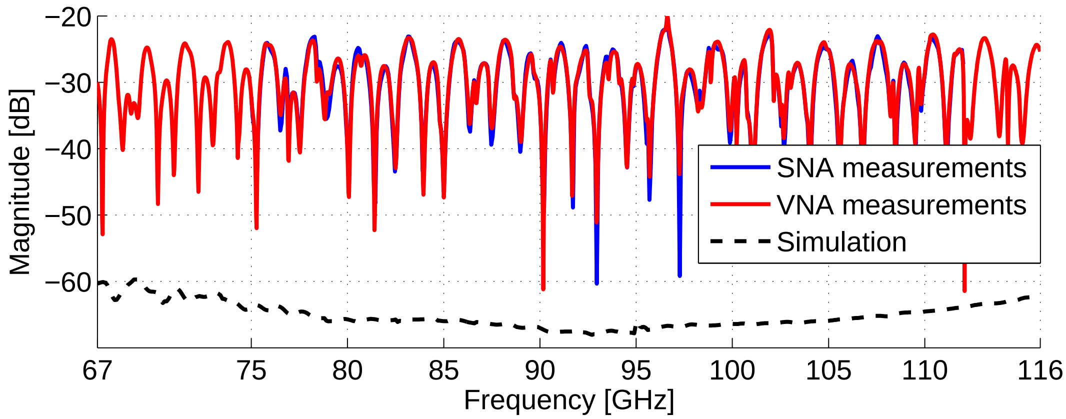

Figure 3.4: Crosspolar Transmission of the OMT v1.

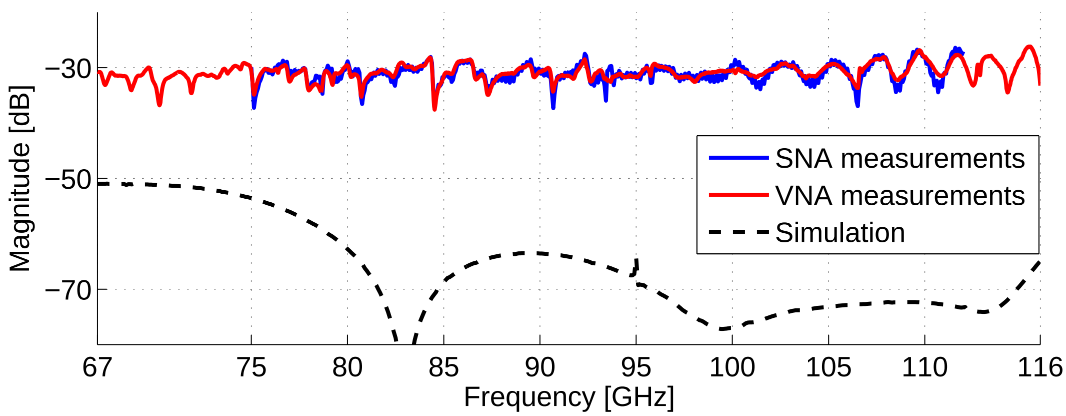

Figure 3.5: Transmission between output ports of the OMT v1.

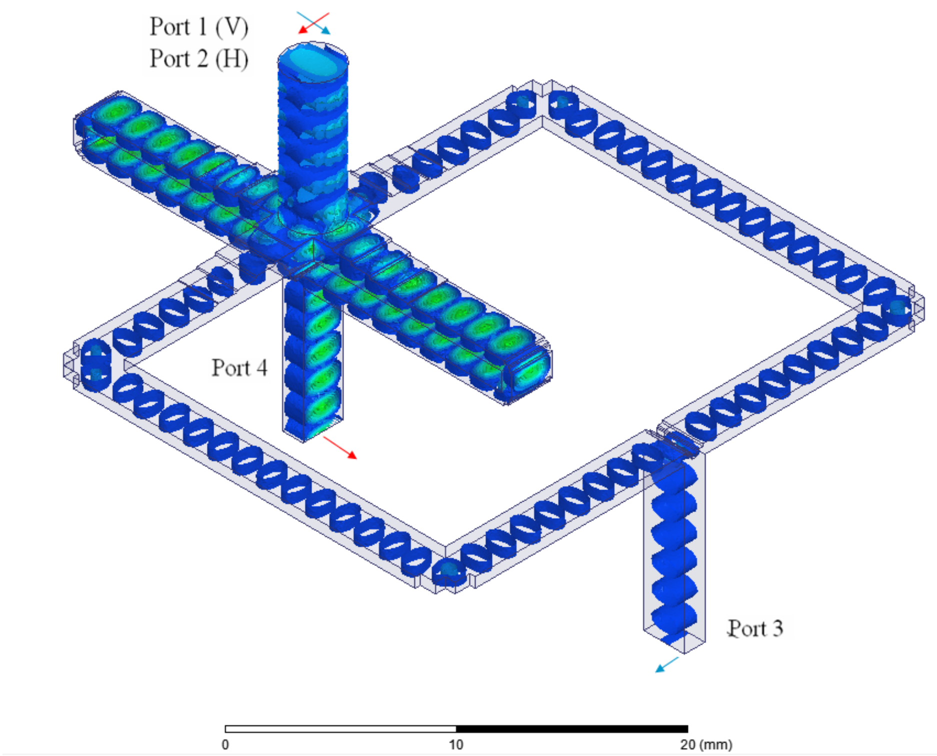

Figure 3.6: New model proposed. The length of the recombinations arms for both polarizations are considerably shorter. The distance between the output ports is set to match the architecture of the receiver.

3.2 Second Version of the OMT

As it can be seen in the previous section, the performance OMT was not up to expectations, particularly in the copolar transmissions. The main factor behind the severe disagreement between the simulations and experimental results was that the geometry made the fabrication and assembly of the OMT difficult and inaccurate. Moreover there was no certainty about the exact electrical properties of the material used to fabricate the OMT. This two issues prompted to take actions to look for ways to simplify the milling of the OMT and how to determine the effective conductivity of the material used for its construction.

The main factors that affected the OMT performance were poor contact on the seams of the waveguide and the length of them. The construction scheme of the OMT places the two E-plane (Figure 3.7a) seams in all the waveguides in the same plane as the Y-combiner (Figure 3.1. The seams are placed in the extremes of the waveguide, were good contact is essential for the TE_{10} currents (Figure3.7b). Furthermore, in order to attenuate higher order modes the waveguides were designed to be as long as possible.In the actually fabricated OMT, these two actions wreaked the performance of the OMT. The reason was poor contact in the seams and the long waveguide, added with the lower than expected wall conductivity. They contributed to reduce even more the efficiency of the OMT.

To avoid placing the waveguide seams in sensitive locations (not to interrupt the mode currents) it is required to change the geometry of the OMT and remove the design constrain

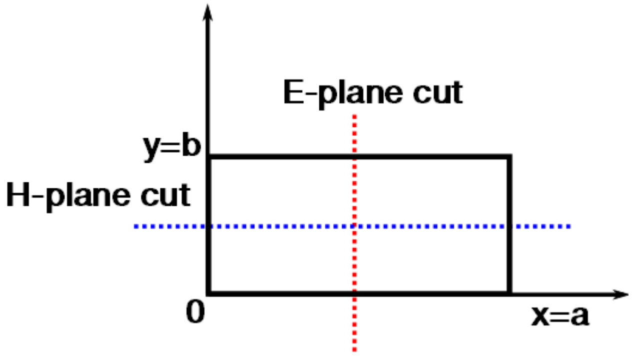

(a) E and H-plane cuts in a rectangular waveguide.

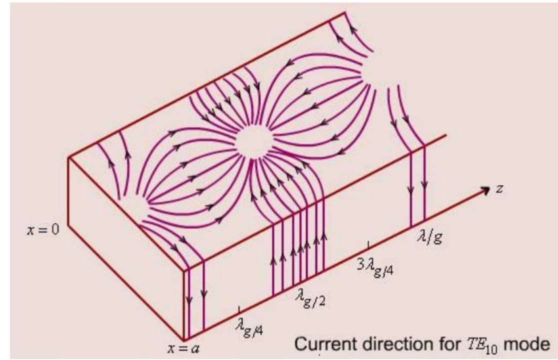

(b) Current distribution in a rectangular waveguide for the TE_{10} mode [54]

Figure 3.7: Cuts and current distribution for a TE_{10} mode. The fabrication of the OMT required that waveguides in the same plane of the Y-power combiners to have seams in $x = 0$ and $x = a$ respectively. .

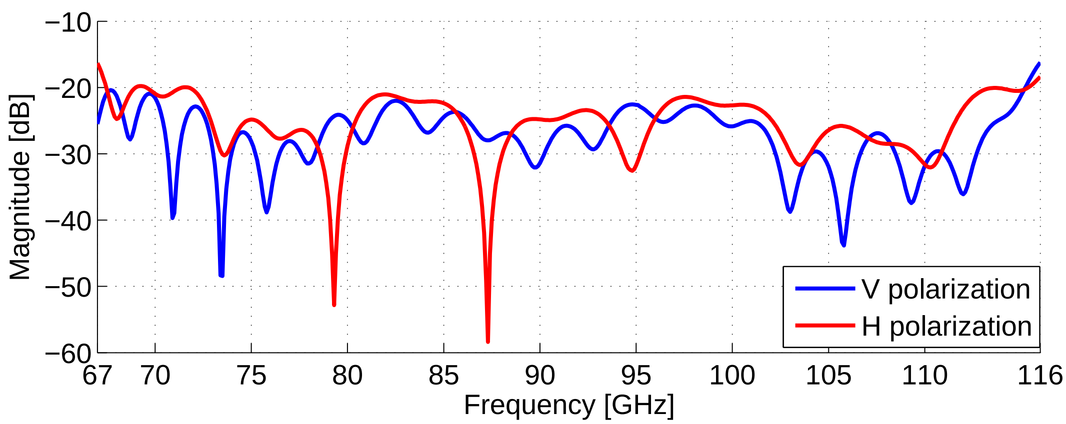

Figure 3.8: Simulated reflections at the input port of the OMT

that the output waveguides of the OMT must be parallel (Figure 3.6). To solve the low transmissions of the OMT it is enough to shorten the output waveguides, but also the use of a material with better conductivity will ensure that the losses are as low as possible.

The new OMT design keeps the turnstile junction intact and the changes solely the length recombination arms of the OMT. The simulation of the OMT considers a sweep of 491 points with2 100 MHz of resolution and the material properties of the Aluminium ($\sigma = 38$ M$Siemens \cdot m^{-1}$, $\mu_r = 1.000021$ and $\varepsilon_r = 1$). Figures 3.8 to 3.11 display the simulated performance of the OMT.

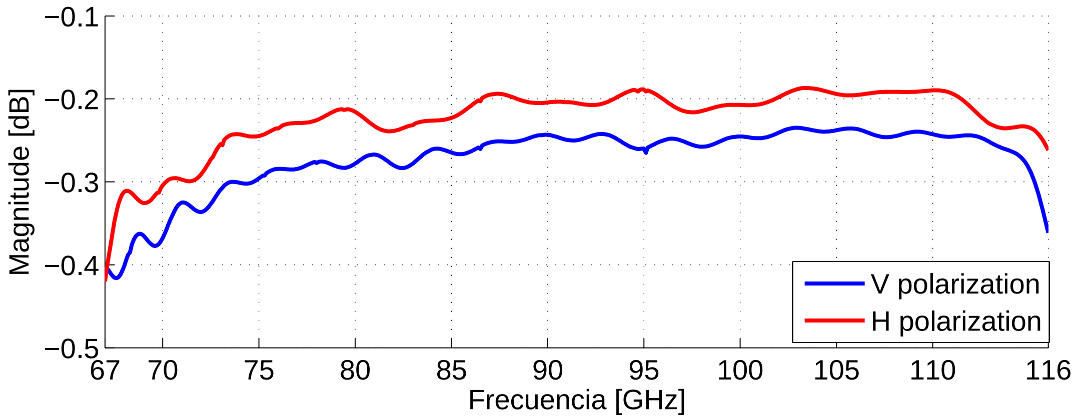

Figure 3.9: Simulated Copolar transmissions of the OMT

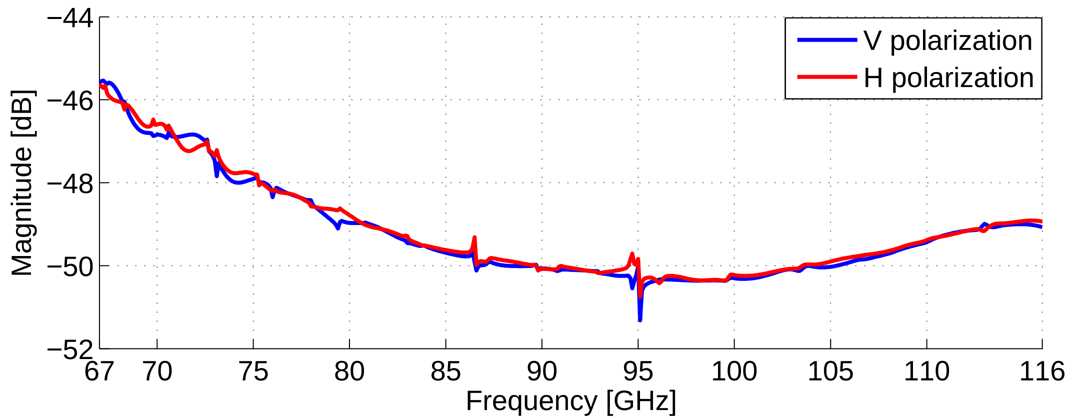

Figure 3.10: Simulated Crosspolar transmissions of the OMT

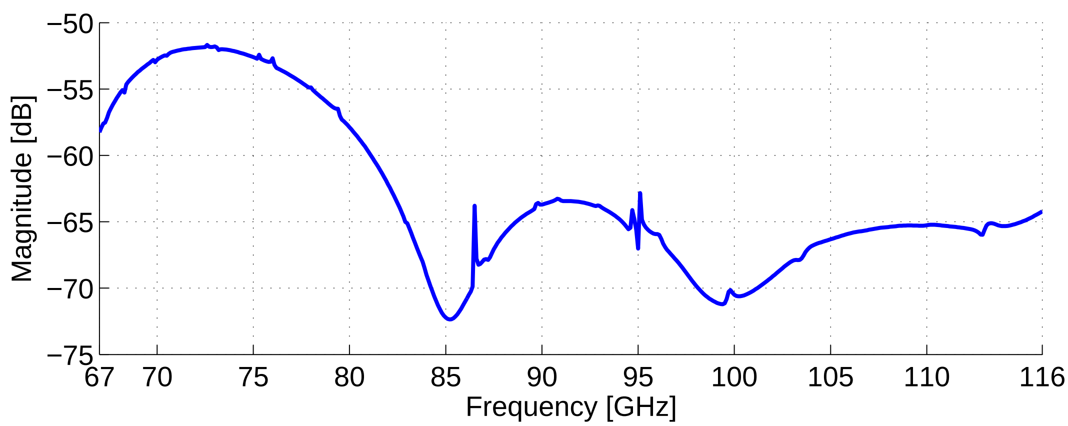

Figure 3.11: Simulated transmissions between output ports of the OMT

Figure 3.12: Built OMT and Horn. The external dimensions of the OMT aluminium block are $14.4 \times 45 \times 56$mm.

3.3 Constructions of Waveguides

The construction of waveguide devices was carried out at the Millimeter Wave Lab. The materials chosen for the constructions of meanders were Aluminium Alloy, due to its widespread use in waveguide components and a C14500 Tellurium Copper Alloy, due to possessing a higher conductivity than aluminium. Meanwhile the OMT was only machined in Aluminium Alloy. To manufacture the devices we resorted to a five axis Kern **C**omputer **N**umerical **C**ontrol (CNC) machine.

3.4 Experimental setup

The OMT (Figure 3.12) was tested at the Instituto Naziolale di Astrofisica with an *MS4647B Anritsu Vector Network Analyzer*(VNA). To attain the four performance parameters of the OMT two measurement configurations . The only difference in the is the termination of the input circular waveguide of the OMT. To test reflections at the output ports and isolation between output ports it is needed to put a load at the input circular waveguide (Figure 3.13a). Meanwhile for the copolar and crosspolar transmission the input waveguide needs to be terminated with a short circuit (Figure 3.13b).

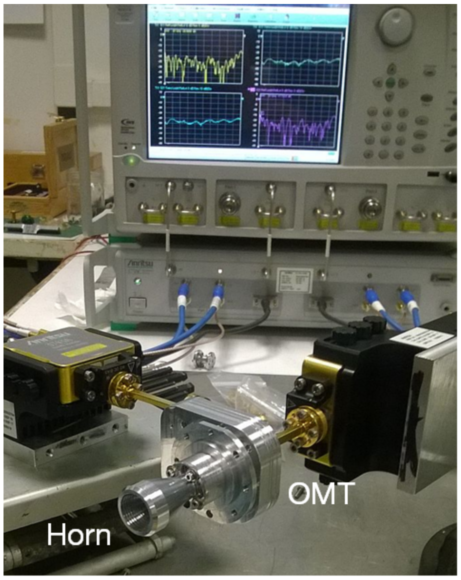

(a)

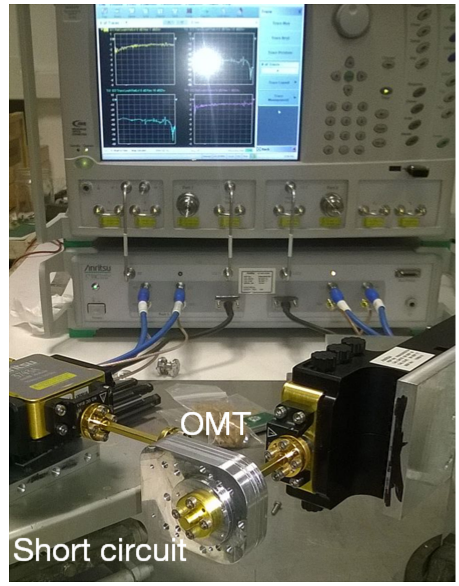

(b)

Figure 3.13: Measurements of the OMT with an Anritsu VNA.(a) Measurement setup for the reflections and isolations between ouput ports. (b) Measurement setup for the copolar and cross polar transmissions.

3.5 Results

The experimental results show a good agreement with the simulated results. The reflection at the output ports (Figure 3.14) are below the required level at most part of the band, rising above −20 dB at the extremes and the center of the band. Also, both polarizations follows the tendency of the simulated results

Both the copolar transmissions (Figure 3.15) are above −1.4 dB over the entire band and above −0.6 dB in the high end at band. There is a great disagreement between the expected and the experimental results, having more than 1 dB of difference at the lower end of the band.

The cross polar transmissions are below −35 dB over the complete band (Figure 3.16) and show good agreement with the expected results. It can be seen that in the high part of the band there are some noise peaks in the cross polar transmission, the reasons for their appearance are detailed in [53]. The cross polar transmission is deeply related with the transmission between the output ports (Figure 3.17). As the cross polar transmission is low, the isolation exhibits levels below −50 dB over the entire band.

The disagreement seen in the copolar transmissions of the OMT may be due to the incorrect characterization of the materials after the process of construction. Fig 3.15 shows that the effective wall conductivity of the waveguides is lower than the nominal conductivity of aluminium.

Table 3.1: Comparison between simulations and experimental results for the OMT

Parameter	Simulation	Experimental
Reflections V Pol	−27.53	−24.76
Reflections H Pol	−25.39	−26.09
Copolar V Pol	−0.27	−0.69
Copolar H Pol	−0.22	−0.52
Xpolar	−49.13	−42
Isolation	−62.88	−60.24

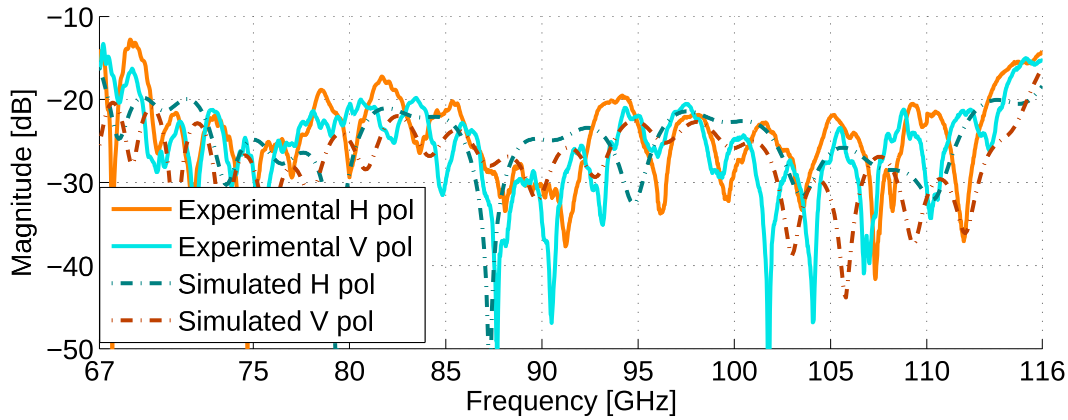

Figure 3.14: Experimental and simulated reflections at the output ports of the OMT

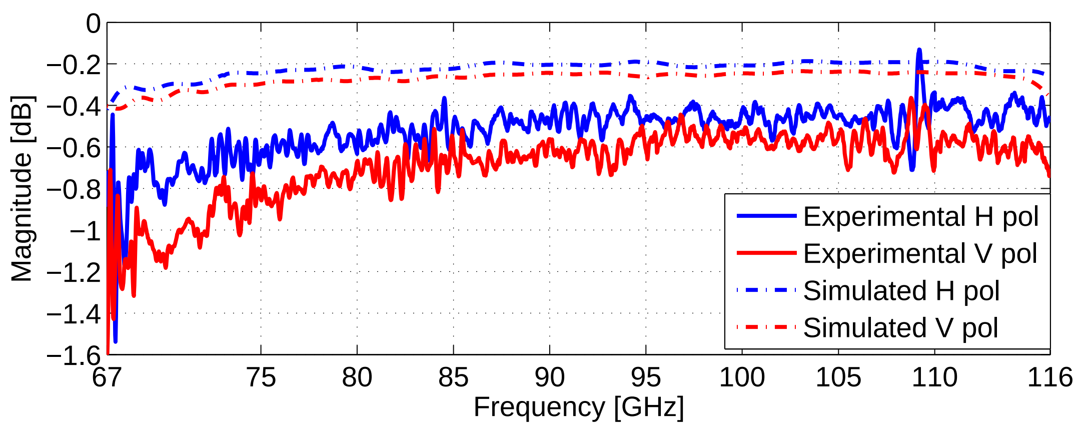

Figure 3.15: Experimental and simulated copolar transmissions of the OMT

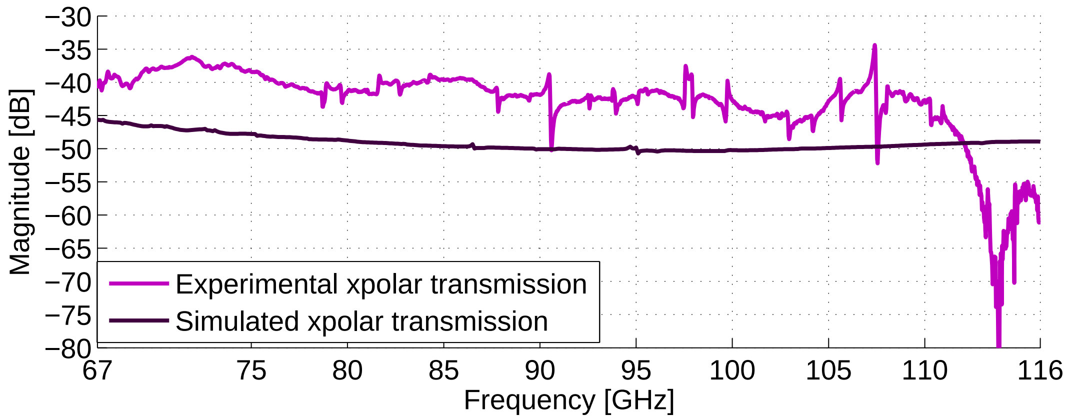

Figure 3.16: Experimental and simulated cross polar transmissions of the OMT

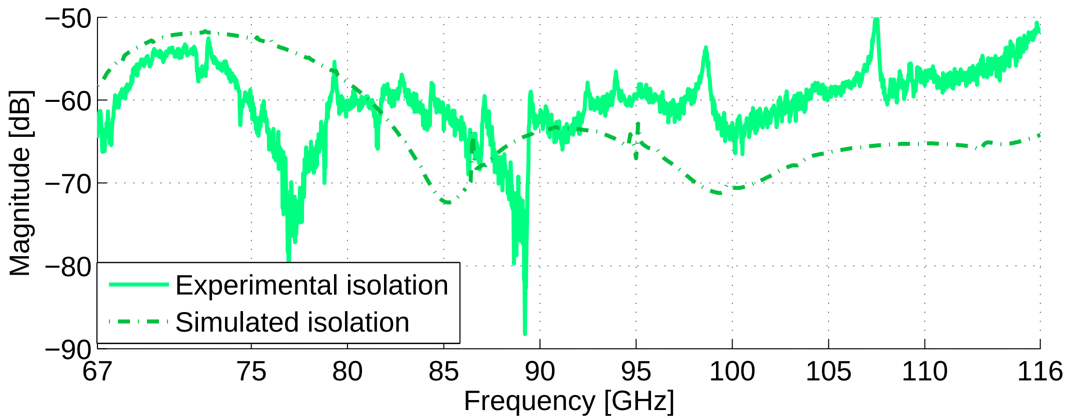

Figure 3.17: Experimental and simulated transmissions between output ports of the OMT

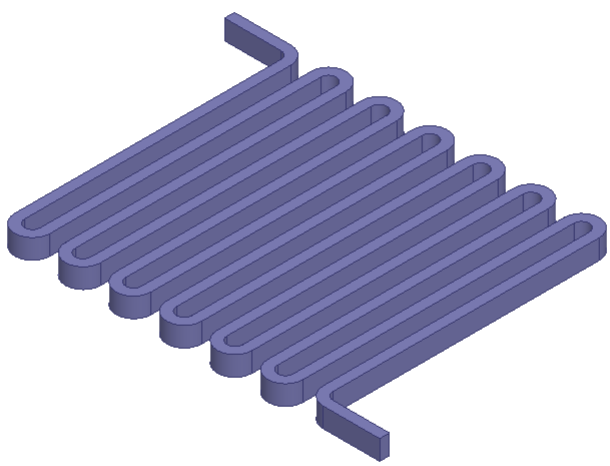

Figure 3.18: Model of the WR10 meander in HFSS. It has a length of 481 mm

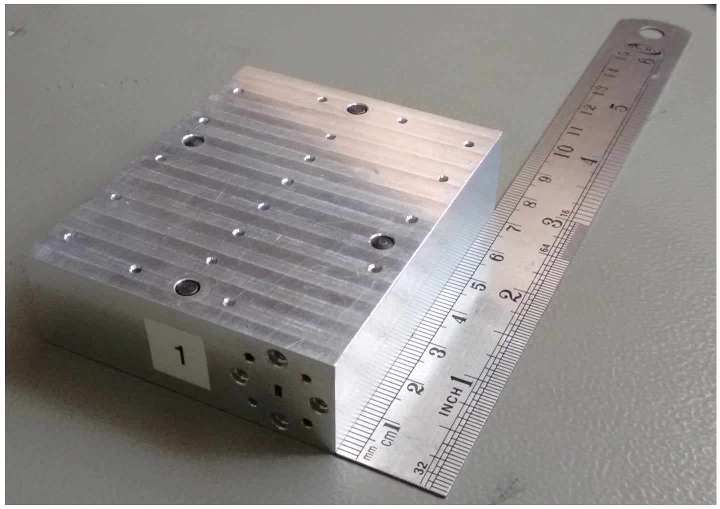

Figure 3.19: Constructed aluminium meander

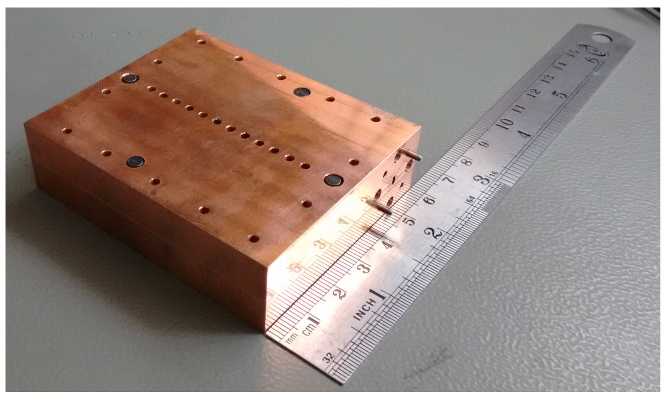

Figure 3.20: Constructed copper meander

3.6 Conductivity Measurement across the W Band

The fact that the effective wall conductivity of the mechanized guides seems to be lower than the nominal conductivity of the Aluminium prompts the characterization of waveguides at different temperatures. In [55] a waveguide meander is proposed to amplify the losses across the W band in order to approximate the effective wall conductivity in an easier manner. A waveguide meander is a very long waveguide curved in a sinuous fashion for space concerns(Fig 3.18)

Two WR10 meander were designed an built at the Millimeter Wave Laboratory. The design procedure of the waveguide meander is detailed by Alexander Ibarra in "*Simulations and design Waveguide WR10*" (Figure 3.18). The meander has a total length of 481 mm and was constructed by the split block technique on Aluminium and C14500 Tellurium Copper Alloy.

The waveguides were tested with the set up configuration presented in Figures 3.21 and 3.22 with home-made Scalar Network Analyser detailed in [52] at the temperatures 290, 77 and 15 K. To accomplish this we placed the waveguide inside the cryostat available at the Millimeter Wave Lab (Figure 3.22). In order to connect the devices in the interior of the cryostat with

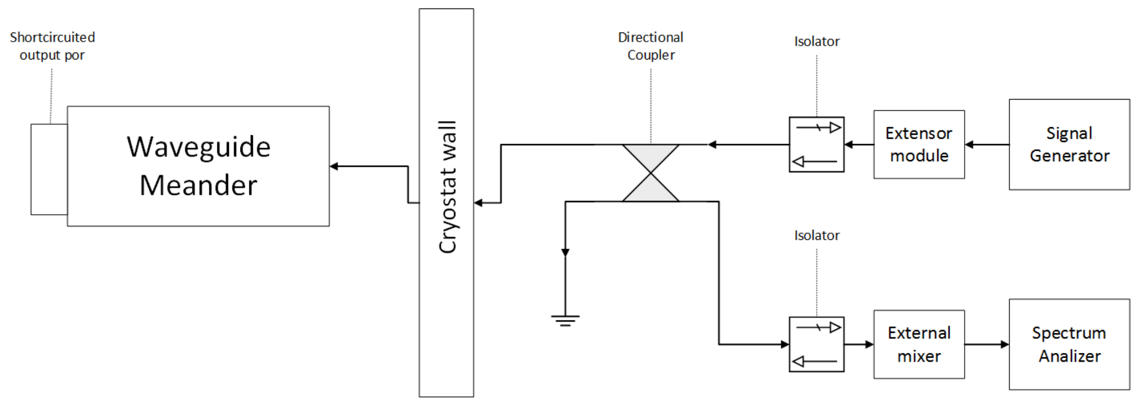

Figure 3.21: Scheme of the setup needed for the meander transmission measurement

the equipment outside a WR10 window is used. To preserve the vacuum within the cryostat, the window is covered with a Mylar film. The process of measuring the transmission on the meander requires a short circuit placed in one of its ports From the outside of the cryostat a signal is launched into the waveguide and travels through the meander to finally be reflected back to the input port of the meander and outside the cryostat. At that point, the wave has travelled twice the meander and allows the calculation of the transmission. The presence of the Mylar film creates a resonator cavity in the cryostat as the interface air - mylar has a reflection coefficient $\Gamma > 0$. This resonator will generate a standing wave whose frequency will be in direct relation to the length of the resonator. A high frequency standing wave is expected to be generated by the cavity resonator as the length of the meander is 481 mm. The effects of this standing wave are visible in the transmissions of the meander as the transmission will exhibit a sinusoidal behaviour across the frequency. The complete response of the transmissions measured can be seen as the addition of effects, the standing wave caused by the cavity resonator and the insertion losses caused by travel of the signal through the waveguide. The nature of this two phenomena is very different, meanwhile the standing wave is a high frequency phenomenon, the insertion losses are characterized by having few and small oscillations across the w band[55]. By virtue of this, it is possible to separate and study each effect independently. The influence of the insertion losses from the effect of the standing wave are separated by a Butterworth low-pass filter, which eliminates the high frequency sinusoidal component of the measurement (Figure 3.23).

The copper and aluminium copper were tested at the cryogenic temperatures of 290, 77 and 15 K at the facilities of the Millimeter Wave Lab. The experimental measurements were compared and matched with HFSS simulations to obtain the effective conductivity of the materials. The different transmissions of the meander and simulations that match them are presented in Figure 3.24 and 3.25. It can be noted that the conductivity of aluminium varies less between the two temperatures than the copper. The effective conductivities for each material at cryogenic temperatures are summarized in Table 3.2.

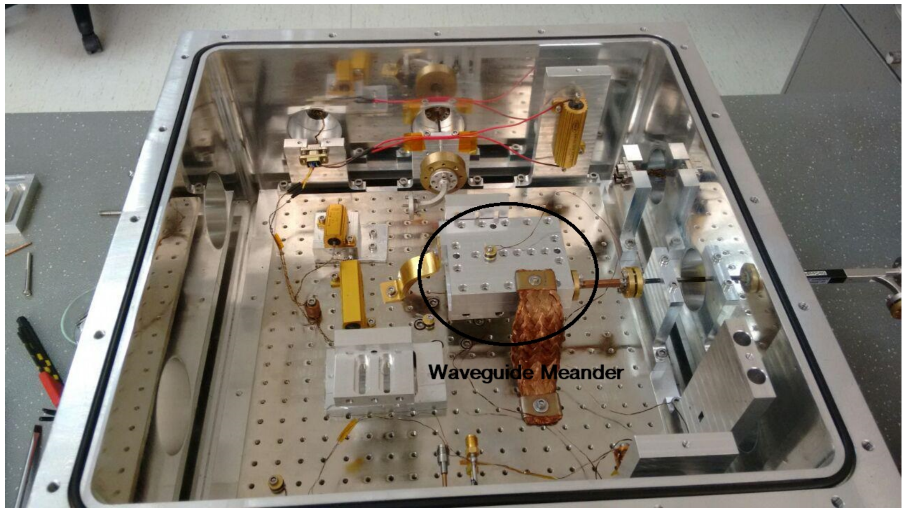

Figure 3.22: Meander inside the cryostat

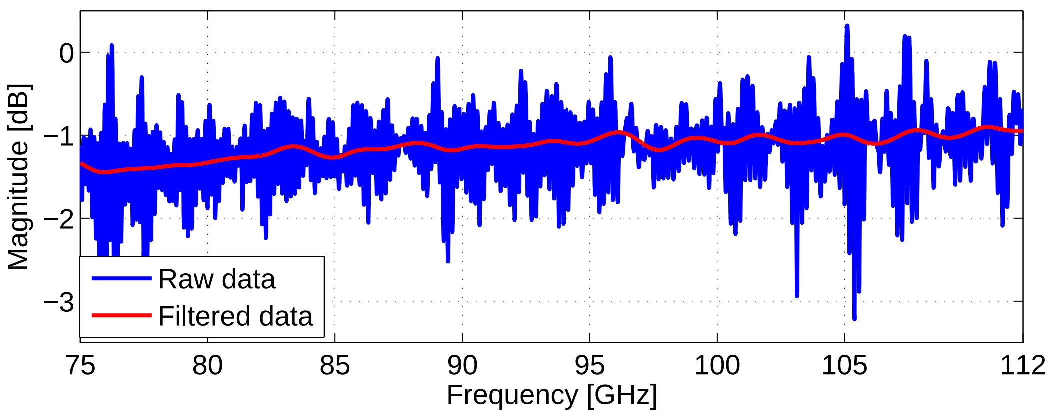

(a) Comparison of raw transmission and filtered transmission of the meander

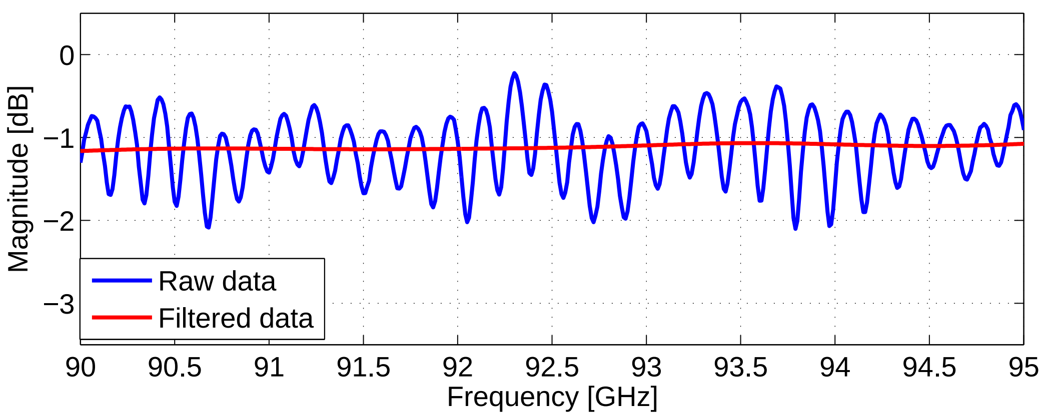

(b) Close up of the transmission of the meander.

Figure 3.23: Measured tranmissions for the meander. The mylar film and the short circuit at the end of the meander generates a cavity resonator which enables the presense of a standing wave.

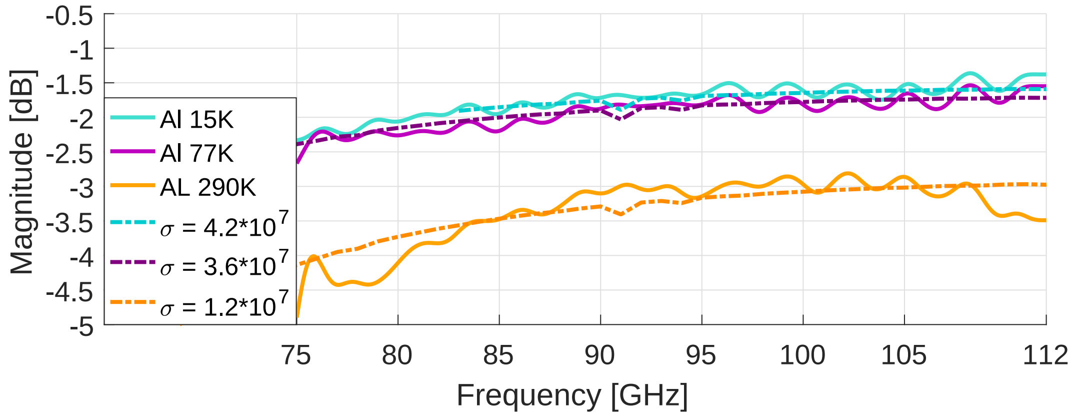

Figure 3.24: Experimental and simulations results of the conductivity measurements of the aluminium meander

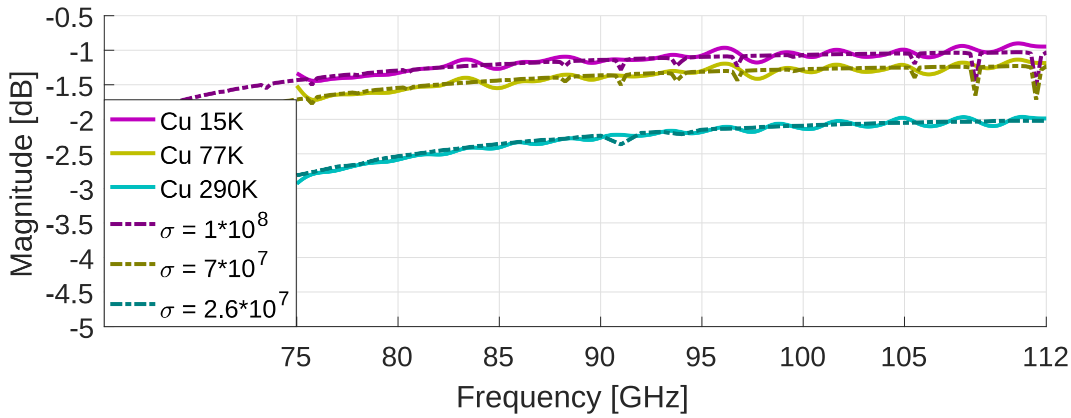

Figure 3.25: Experimental and simulations results of the conductivity measurements of the copper meander

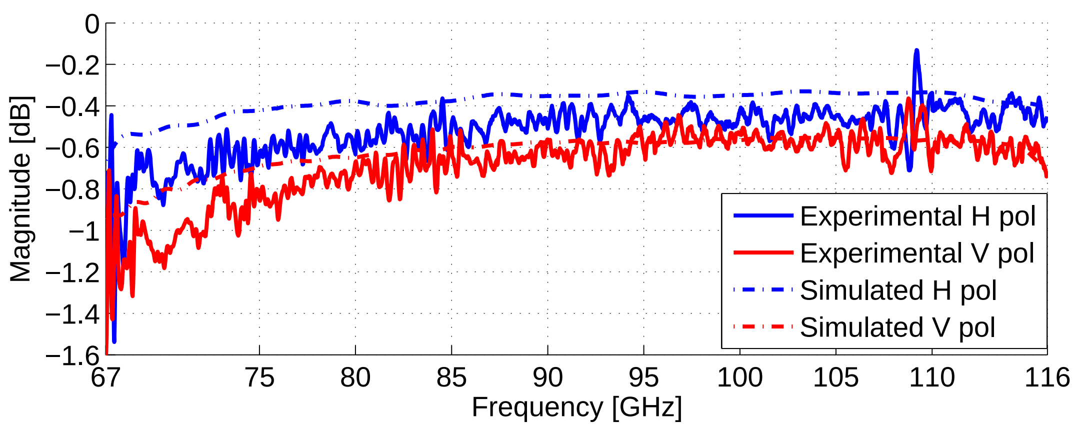

Figure 3.26: Experimental and simulated copolar transmissions of the OMT

Table 3.2: Conductivity of Aluminium and Copper milled waveguides at different temperatures

Material	Conductivity Sm^{-1}		
	290 K	77 K	15 K
Aluminium	$1.2 \cdot 10^7$	$3.6 \cdot 10^7$	$4.2 \cdot 10^7$
Copper	$2.6 \cdot 10^7$	$7 \cdot 10^7$	$1 \cdot 10^8$

Table 3.3: Comparison between simulated insertion losses with the effective conductivity and experimental results

Parameter	Simulation	Experimental
Copolar V Pol	-0.63	-0.69
Copolar H Pol	-0.38	-0.52

With the value of effective conductivity for the aluminium at 290 K we calculated the insertion losses of the OMT (Figure 3.26 and Table 3.3) . The simulation show a good degree of agreement with the experimental results over the half and upper part of the band.

3.7 Summary

In this chapter we have presented a new design for the OMT, detailing the construction and characterization procedures and the method used to obtain the effective conductivity of certain materials at cryogenic temperatures.

The effective conductivities for aluminium and copper at 290, 77 and 15 K were presented. The effective conductivity of both, aluminium and copper are significantly higher at cryogenic temperatures having values of $4.2 \cdot 10^8$ and $1 \cdot 10^8$ $S{\cdot}\mathrm{m}^{-1}$, respectively. The simulated and experimental result of the OMT shows a good agreement and are a significant improvement from the first model of OMT for ALMA Band 2+3.

The process of calculating a effective wall conductivity for the mechanized waveguides proved to be useful and precise as a first approach. If more precision is required, the surface roughness needs to be measured and its effect on the transmissions characterized. However this procedure can be more difficult and time consuming than approximating the effective wall conductivity.

Chapter 4

SMAI

This chapter details the proposed schemes for a LO-power distribution for the SMAI receiver, as well as the respective components required, their design, performance and issues at the current stage of development.

4.1 First Power Distribution Design

To achieve the requirements established for the LO distribution to the 16 pixels of **SMAI** a 1D integration approach is taken. The complete distribution block will be made of four basic blocks, each one of them will distribute the incoming LO signal to a row of four Superconductor-Isolator-Superconductor (SIS) Mixers (Figure 4.1).

The first step was designing a simple divider to be the basic block of the device. Due concerns about size and construction capabilities, the transmission line chosen to make the division was a coplanar waveguide. The first approach was to design balanced power dividers and to make the division of power symmetrical regarding components and distance. Marc Peter Westig demonstrated the performance of CPW devices at 490 GHz [56], in particular, a 90° hybrid and a waveguide-to-CPW transition. For that reason, the first power divider proposed for the system of Figure 4.1 is a 90° Hybrid [57].

The second stage was choosing a way to deliver the input signal to each divider and to each mixer. Then, it is necessary to generate all the required devices for such endeavour. The main concerns are the transmission losses of the line and its construction feasibility.

The third phase consist of using CST circuit solver to simulate the distribution of a row of four pixels to attain the approximate behaviour of the system.

The fourth step is to analyse the issues that may have turned up in the last phase and carry out the possible solutions. The simulations of the proposed systems shows the presence of standing waves within the systems. For that reason a new scheme is recommended with a different approach to the power division. To detect obstacles early on and to test if the new

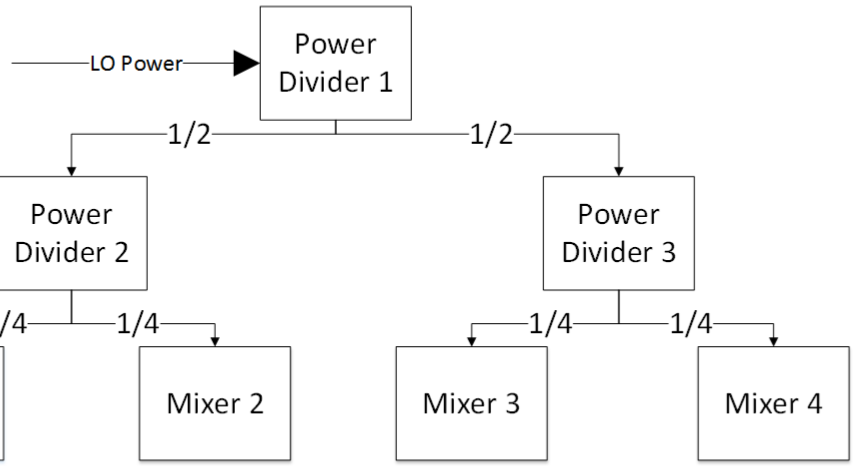

Figure 4.1: Scheme one of the blocks of the proposed LO-power distribution. It is intended that each of the power dividers will be implemented on planar circuits. Meanwhile the proposed transmission lines to deliver the signal to each divider, and to the mixers are waveguides, mainly because powerloss concerns.

design will solve the issues of the initial design, the power divider is analytically designed and included in a circuit solver of the basic block. Once its has been proven that the new approach can overcome the problems of the initial design, we proceed to design the power dividers. Finally, once all power dividers are designed a final check is executed in a circuit simulation of the basic block with the designed components.

To model and simulate the behaviour of the CPW components we recurred to CST Microwave Studio and CST . The difference lies in the solver used by both software, ANSYS HFSS uses a frequency solver meanwhile CST utilises a time domain solver allowing detection of narrowband behaviour. The parameters of the simulation are

- Two modes excitation at each port (even and odd quasi-TEM mode).
- Frequency samples: 1001.
- Frequency span: 700-900 GHz.
- Metal : Perfect Conductor.
- Metallization layer: 0.5 μm.
- Substrate : Silicon ($\varepsilon_r = 11.9$).
- Substrate Thickness : 5 μm.

This parameters will be used as default parameters unless specified otherwise.

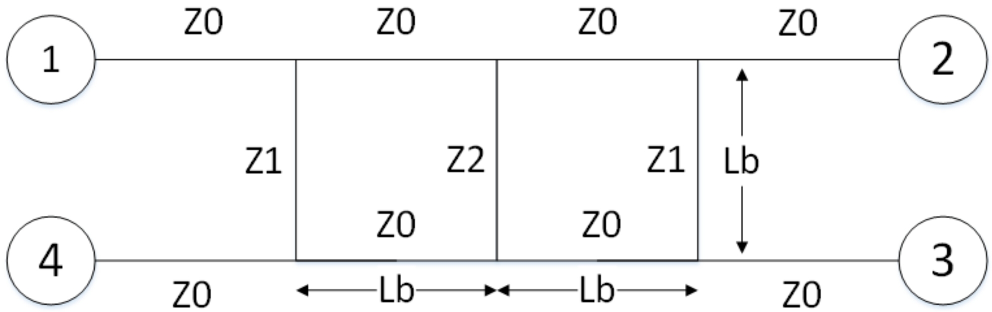

Figure 4.2: Scheme of the hybrid with its three cross arms and relevant parameters of the design.

Table 4.1: Calculated dimensions of the hybrid

Line	W [μm]	s [μm]	Impedance [Ω]
Z_0	8	3	45
Z_1	1	11.5	108.63
Z_2	8	1	31.82

4.1.1 Hybrid Design

The hybrid design is a three crossed-arm hybrid (Figure 4.2) so that the impedance matching is better than a normal two cross-arm hybrid. The parameters of the hybrid are obtained from [57] and given by.

$$Lb = \frac{\lambda_{guided}}{4} \tag{4.1}$$

$$Z_1 = Z_0 \cdot 2.415 \tag{4.2}$$

$$Z_2 = \sqrt{2} \cdot Z_0 \tag{4.3}$$

The impedance of line is $Z_0 = 45\,\Omega$, was picked for easiness of design . The metallization layer and substrate thickness are fabrication parameters and were kept constant of the CPW devices. This leaves only the width of the line (W) and gaps between ground planes (s) as design variables for most of the CPW circuits. Therefore using equations 4.1 to 4.3 the initial dimensions the line Z_0 and the cross arms of the hybrid were calculated.

As described above, the cpw supports two degenerated quasi-TEM propagation. This effect can be very harmful to the CPW tranmissions as the odd mode subtracts energy from the fundamental mode even and introduces noise to the transmissions. The propagation of the odd mode requires two conditions. First it needs a excitation, and, second, a difference in the electric potential between the two ground planes.

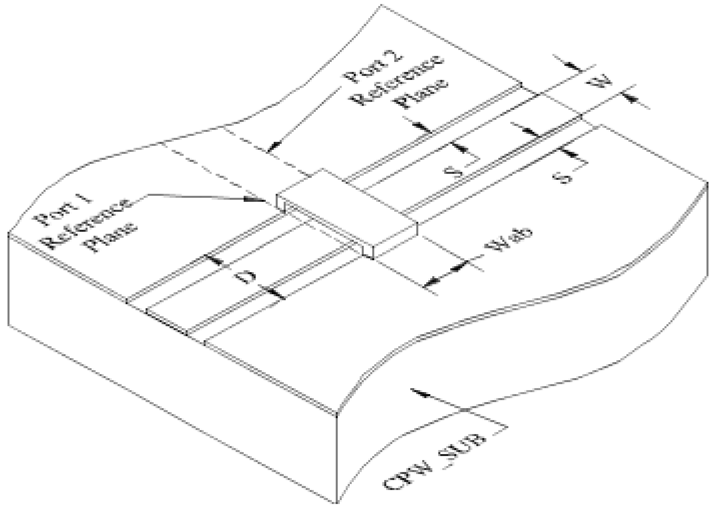

Figure 4.3: Example of a air bridge over a CPW line [58].

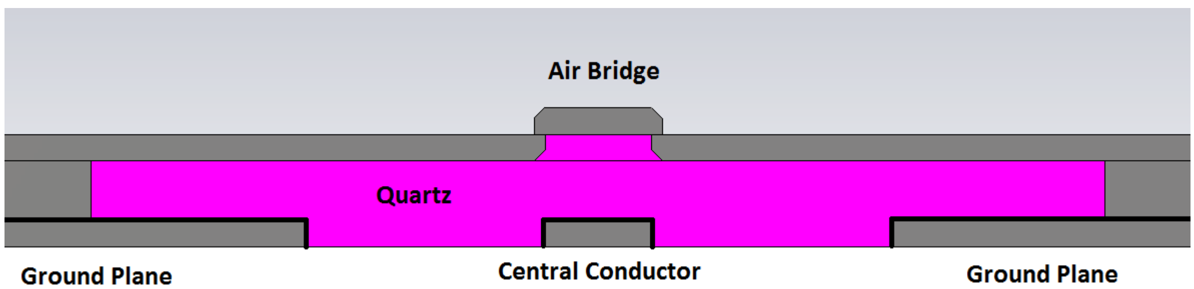

Figure 4.4: Lateral view of the air bridges. Quartz is chosen to support the bridge due its low relative permittivity ($\varepsilon_r = 2.2$).

Since the excitation of the odd mode (and other high order modes) happens at every discontinuity of the CPW line, it is impossible to avoid its appearance in any other CPW device except for a straight line. Nevertheless, by assuring that the two ground planes have the same potential the odd mode propagation can be prevented. To make sure that potential on the ground planes is the same conductive air bridges are placed at the discontinuities of the CPW line (impedance variations, junctions or bends). Thus, removing the condition for the odd mode propagation (Figure 4.3).

Due to the fabrication process and mechanical stability of the metal at μm scales, it is impossible to build the air bridges without supporting material. To solve this concern, it has been decided to sputter quartz on the CPW line to support the air bridges (Figure 4.4). Owing to the overlap tolerances between each layer of the CPW devices, the conductive bridges requires to be at least 3 μm from the quartz edges for photolithographic fabrication reasons.

Due to the need of integrating the hybrid into other CPW circuits and different devices, the use of bends is required (Figure 4.5). We designed a 90° and a 45° CPW mittered bends [59] (Figures 4.6 and 4.7). As we were interested on the reflections of the even mode we do not include the air bridges required for the odd mode suppression. For simulations constrains the 45° could not be simulated by itself and it was needed to analyse two bends in series as

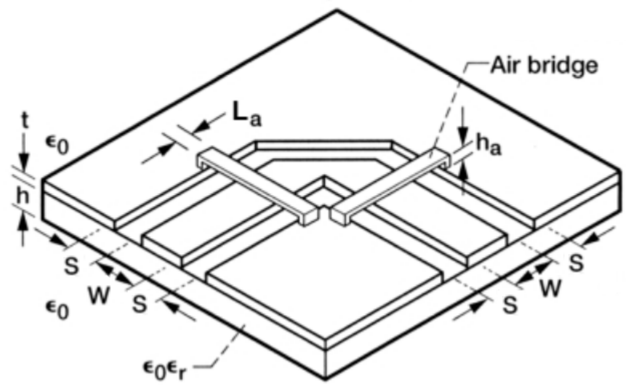

Figure 4.5: Example of the use of air bridges over a CPW mittered bend to deter the propagation of the odd mode [48]

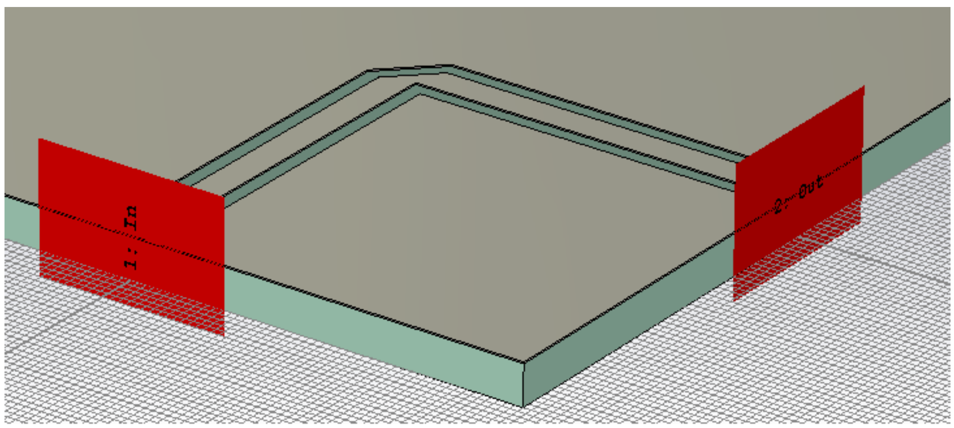

Figure 4.6: CST model of a 90° bend.

the ports can only lie orthogonal to the $\hat{x}$, $\hat{y}$ or $\hat{z}$ vectors. The simulations of both bends are presented in Figures 4.8 and 4.9.

Once the bends have been completed, a first design of the hyrbid were sketched (Figure 4.10) and simulated. The results were not as expected. The high relative permittivity of the silicon reduces the guided wavelength λ_{guided} of the transmission line, making the length of the arms of the hybrid very similar to the width of the lines. Furthermore, even though the relative permittivity of the quartz is very low, it still changes the effective permittivity of the CPW line. All those factors were not accounted for in the theoretical calculations and its effect on the performance of the hybrid was not studied. However, the initial dimensions of the hybrid (Table 4.1) gives a starting point from where to start the optimizations of the hybrid. Table 4.2 displays the final dimensions of the hybrid cross arms and the results are given in Figures 4.11 and 4.12.

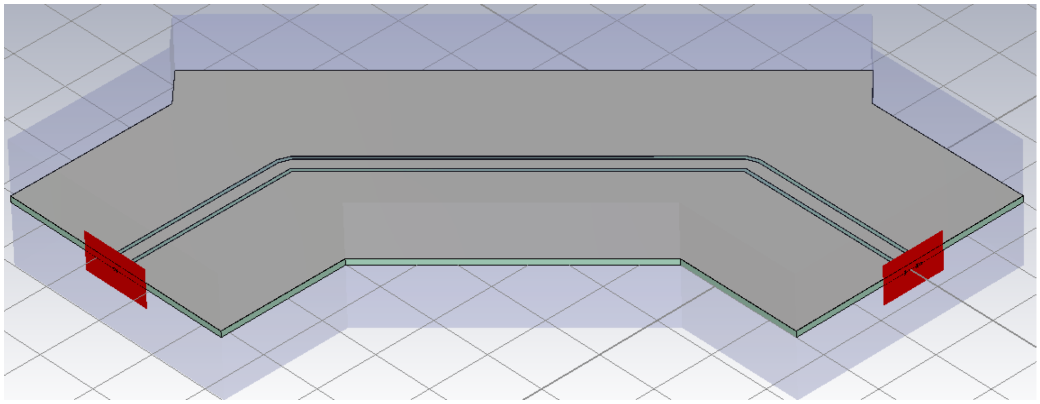

Figure 4.7: CST model of a 45° bend.

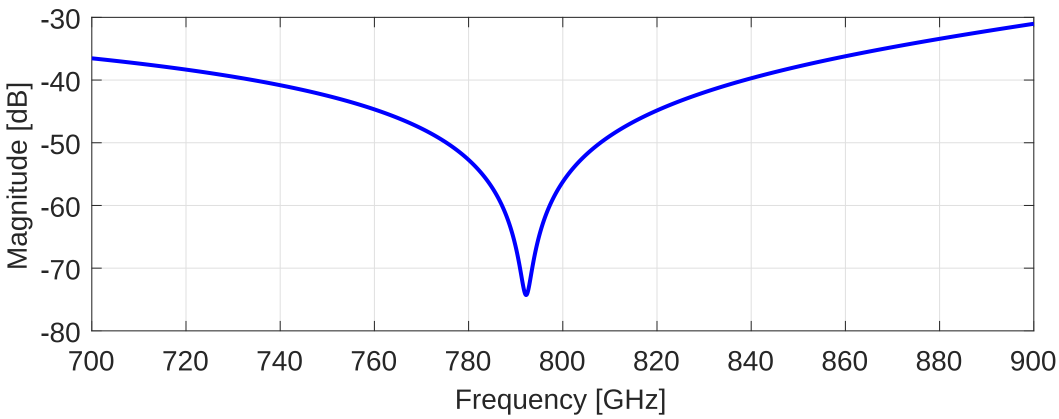

Figure 4.8: Reflections from the 90° bend (S11 Parameter).

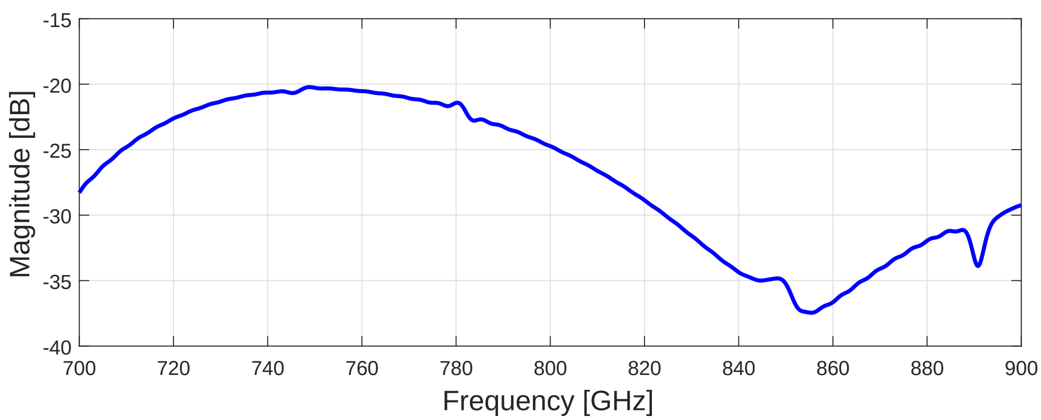

Figure 4.9: Reflections from the 45° bend (S11 Parameter).

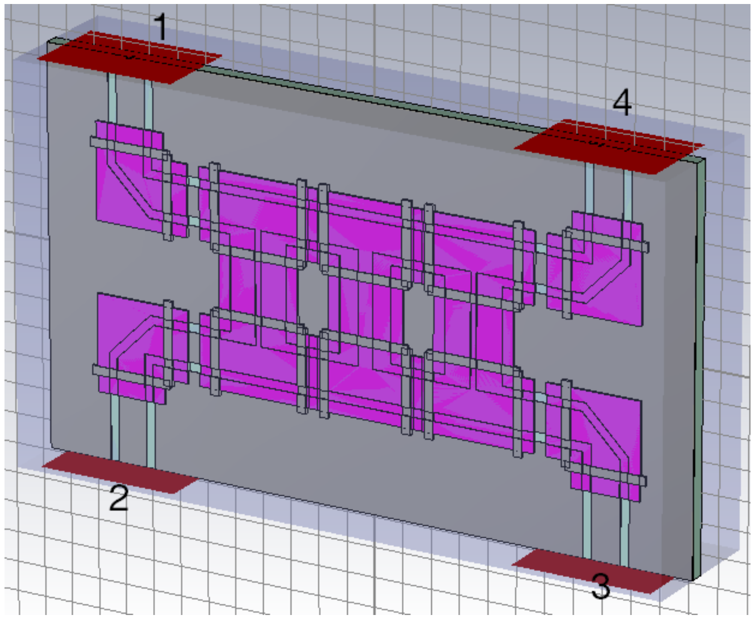

Figure 4.10: CST model of the hybrid designed and optimized. Port 1 is the input port meanwhile ports 2 and 3 are the output ports and port 4 is the isolated port

Table 4.2: Optimised dimensions of the hybrid

Line	W [μm]	s [μm]	Impedance [Ω]
Z_0	10	3	45
Z_1	2	9	108.63
Z_2	5	6.6	31.82

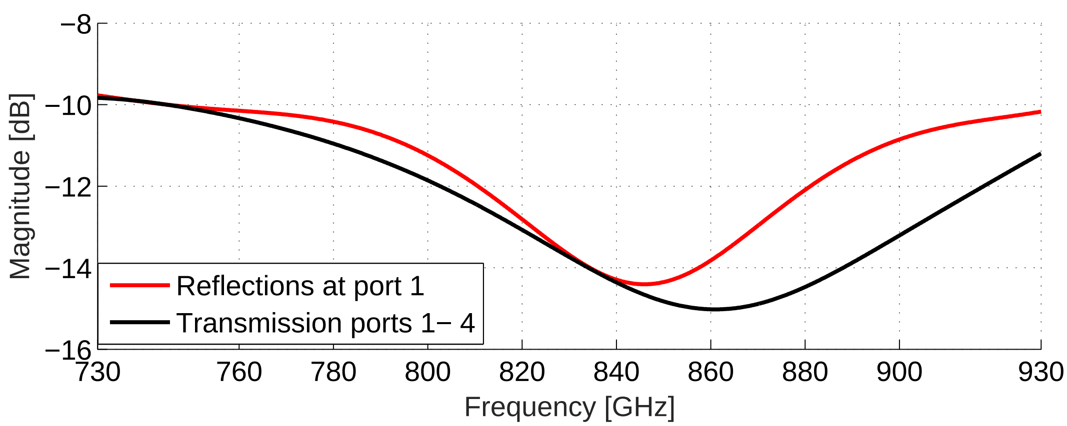

Figure 4.11: Reflections at the input port and transmissions to the isolated port of the Hybrid.

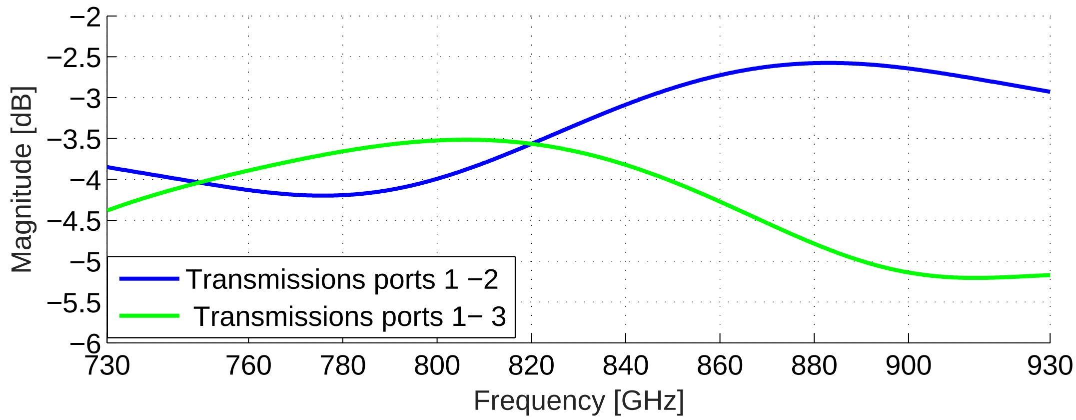

Figure 4.12: Transmissions to ports 2 and 3.

4.1.2 CPW-to-waveguide Transition

After the power division is carried out by the hybrid, the signal needs to be launched to waveguides for its further distribution to other hybrids or to be delivered to the mixers. To accomplish such deed we resort to waveguides as they are easier to manufacture than CPW lines or planar circuits and are more practical due the dimension requirement of the distribution. There is also the concern about the handling of large silicon slabs, as they may break during the manufacturing process. The lateral dimensions of the waveguide proposed to deliver the signal are $150\,\mu m \times 300\,\mu m$

We selected a type of transition developed in [56]. It was modified to suit the requirements of the system, such as the input and output transmissions lines. The transition uses an intermediary transition from CPW to slotline and then from the slotline to the intended waveguide (Figure 4.13). To match the coplanar waveguide to the slotline a quarter lambda adaptation was used. The line has been bend by reasons of space concerns. A conductive bridge with inductance compensation is used to deter the propagation of the odd mode through the CPW line and its coupling waveguide mode. Figure 4.14 shows the reflection losses of the transition.

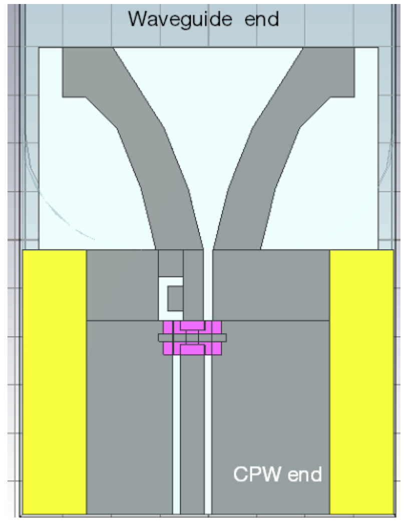

Figure 4.13: CPW to Waveguide transition. The transition uses an intermediary slot line to achieve the transition

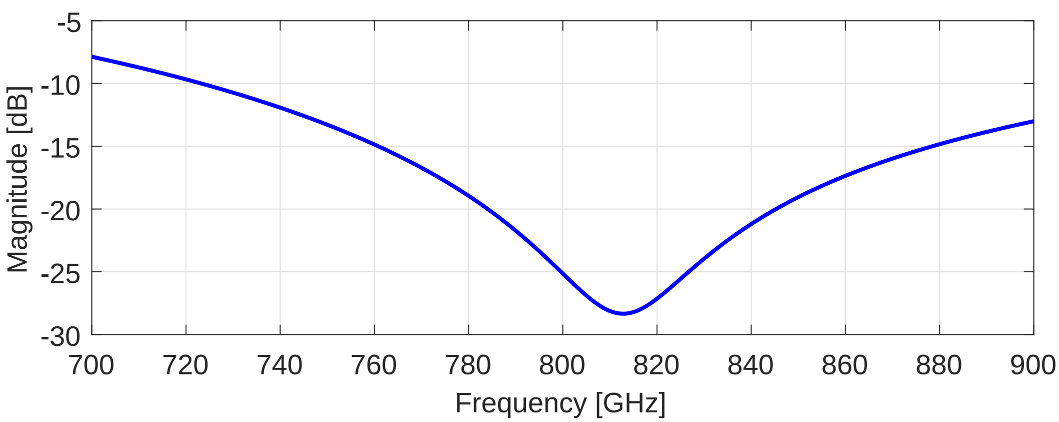

Figure 4.14: Reflections of the CPW to Waveguide transition

4.1.3 Simulation of the Basic Distribution Block

Once the hybrid and basic devices have been designed and simulated , it is necessary to attain a first approximation of the expected performance of the device. The designed block consists of a row of four mixer and it was contrived by Pablo Tapia at the I. Physikalisches Institut of the university of Cologne (Figure 4.15). The use of hybrid as a mean to divide the LO power demands the usage of loads to terminate the isolated ports. This reduces the effects of incoming reflections at ports 2 or 3 of the hybrid. To guarantee minimal reflections coming through the isolated port 4 we resort to waveguide meanders between the port and the load. The length of the waveguides delivering the LO signal to the hybrids are

- **P1**: Delivers the LO signal to the first hybrid. Length = 8640 μm
- **P2**: Conveys the LO signal from the hybrid 1 to the hybrid 2. Length = 7130 μm
- **P3**: Transfers the LO signal from the hybrid 1 to the hybrid 3. Length = 27730 μ m

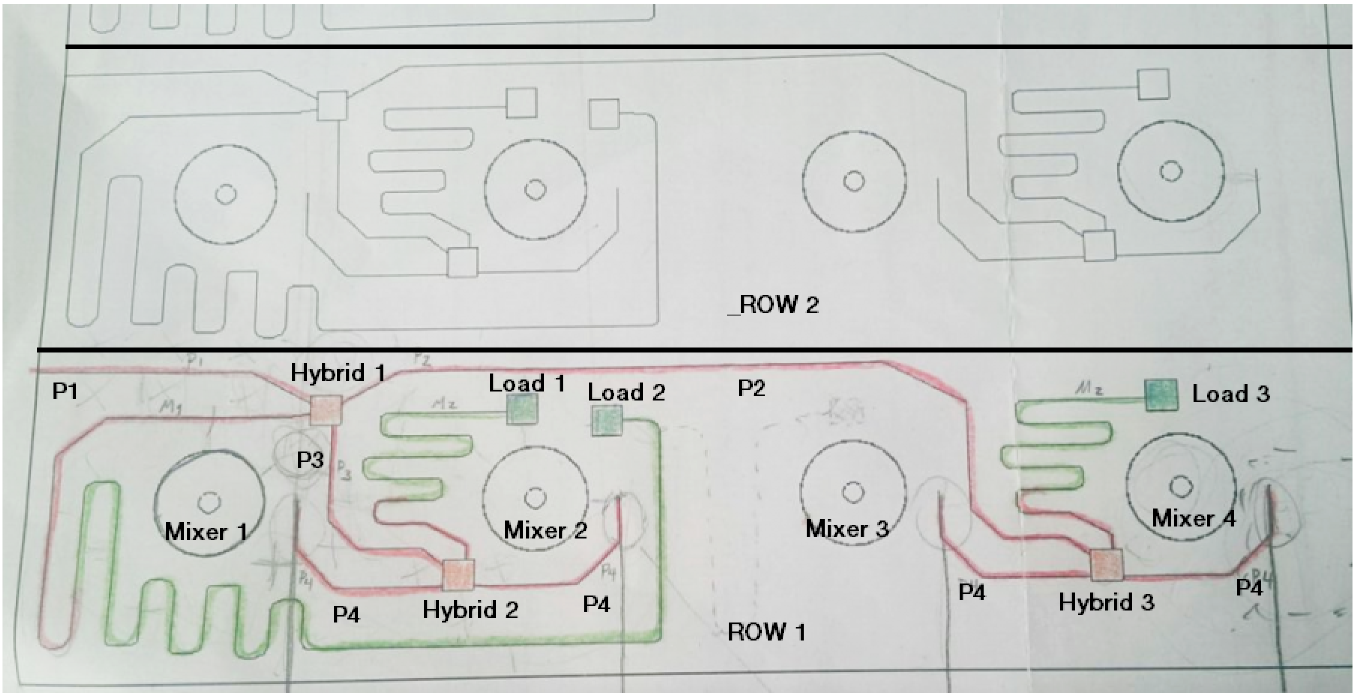

Figure 4.15: Proposed distribution of devices in the basic block of the LO distribution. The position of the hybrids, loads and mixers are displayed. *Credits: Pablo Tapia*

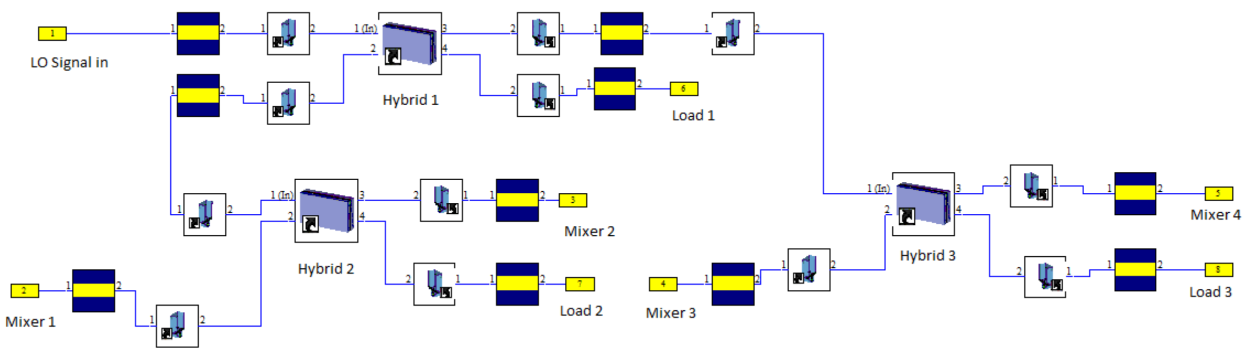

Figure 4.16: Scheme of the proposed LO distribution network in CST. The loads and mixers are replaced with ports since they can emulate the levels of reflections expected from these devices.

- **P4**: Carries the LO signal from hybrids 2 and 3 to the Mixers. Length $= 6400\,\mu$ m

To test the performance of the distribution system we resort to the circuit simulator of CST provides. For this simulation we considered perfect waveguides, as it was not possible to add the feature of finite resistivity to the waveguide basic block. The loads and the mixers are emulated by circuit ports since their impedances can be adjusted manually (Figure 4.16). The port loads have been set to have -25 dB of reflection, while the mixers have an optimistic level of -7 dB of reflections. Results from the circuit simulation are presented in Figures 4.17 and 4.18.

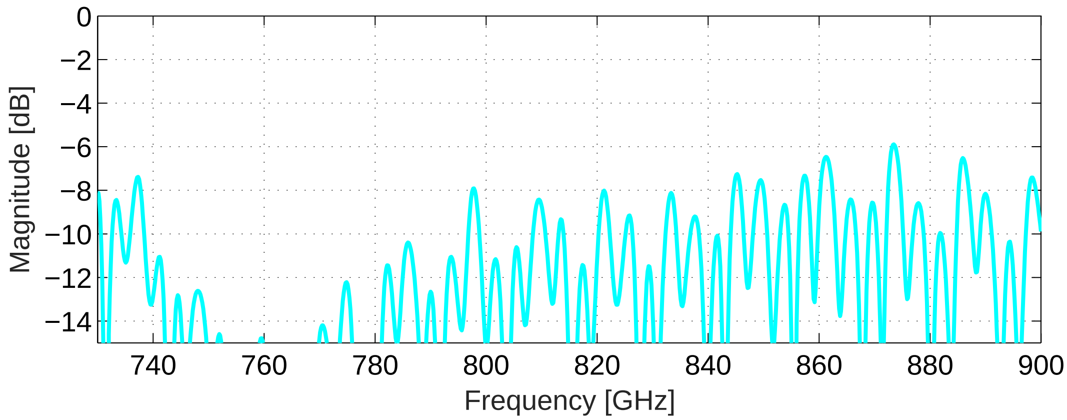

Figure 4.17: Reflections at the input of the block.

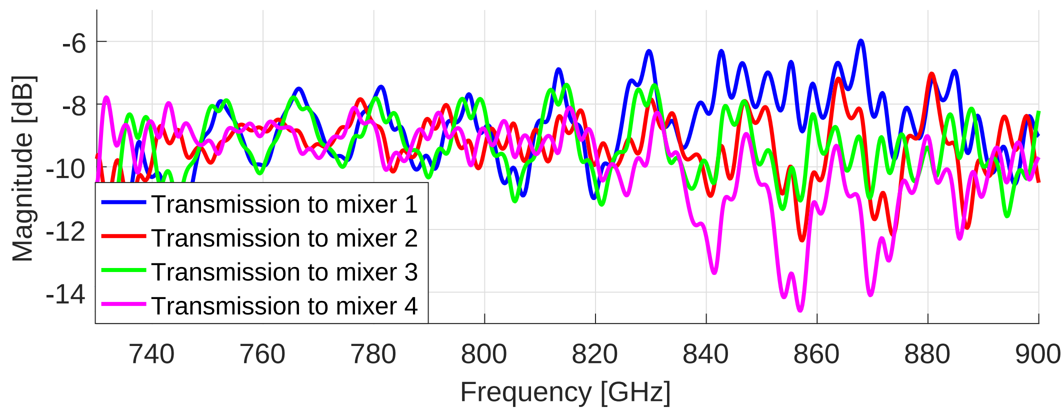

Figure 4.18: Power transmission to the four mixers

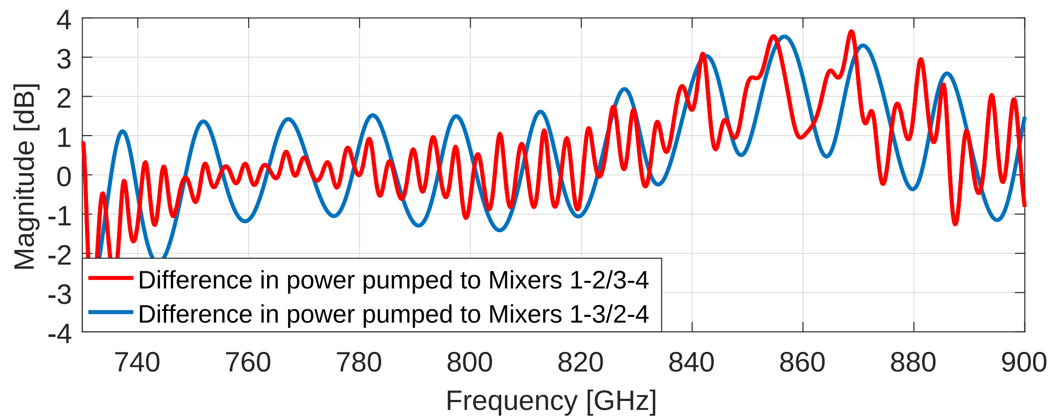

Figure 4.19: Difference in power pumped to the mixers. In the 800-820 GHz band the difference is greater than 1 dB between mixers 1-3/2-4.

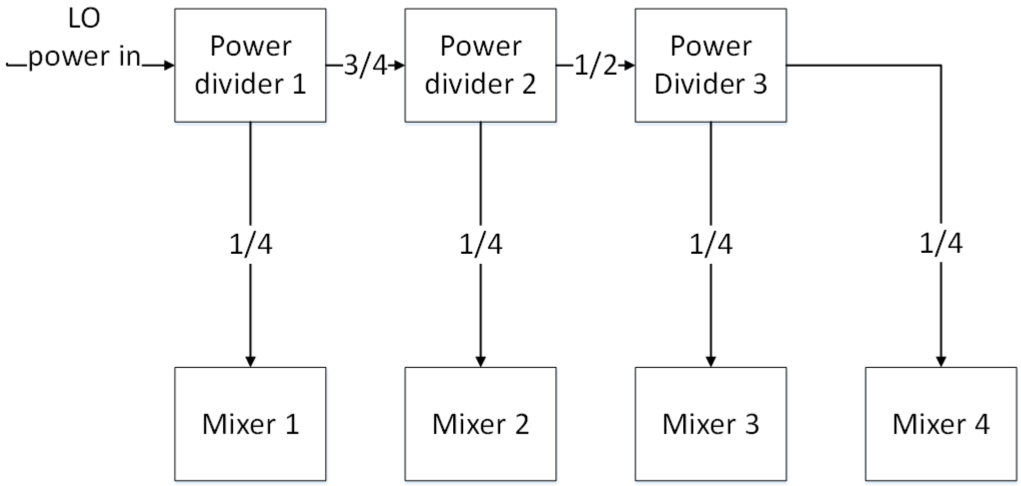

Figure 4.20: New scheme for the power division. Due to way the power is divided, the power dividers require to be unbalanced and have the division ratios of 3 : 1,2 : 1,1 : 1 respectively.

4.2 Second Power Distribution Design

Due the appearance of standing waves in the current design the power pumped to the mixers is not balanced. To reduce the effect of the standing waves it would be needed to, either, reduce the length of the waveguides or to match better the CPW and waveguide devices. Taking a step back in the design, a new scheme with unbalanced power dividers is proposed (Figure 4.20).

To achieve the unbalanced power division with hybrids, it would require further analysis. Furthermore, it would not relieve the need of including a load in the design. However, Wilkinson power dividers [60] have been proven to achieve high division ratios [61, 62] so they are the device of choice for the second power distribution design.

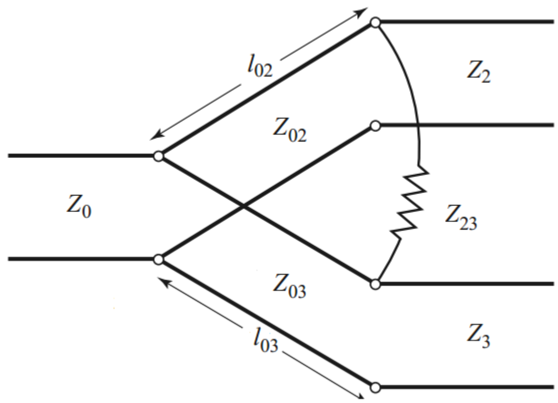

Figure 4.21: Scheme of a wilkinson power divider [38].

Table 4.3: Calculated impedance values for the three Wilkinson power dividers

Parameter	Value Ω		
	3:1	2:1	1:1
Z_0	41.04	41.04	41.04
Z_{02}	35.09	42.27	58.04
Z_{03}	108.02	84.53	58.04
Z_{23}	94.78	87.05	82.08
Z_2	23.7	29.01	41.04
Z_3	71.08	58.04	41.04

4.2.1 Wilkinson Power Dividers

The Wilkinson power divider is a three port network that has the convenient feature that its output ports (Figure 4.21) are isolated from one another [38]. The division ratios can be varied and we will focus on the 3:1, 2:1 and 1:1 division ratios for the LO distribution. The impedance values for each divider are displayed in Table 4.3.The complete derivations and analysis for this circuit can be found in [38]. The power dividers are simulated in the CST circuit simulator an its results are presented on Figures 4.22 to 4.27. To reveal problems early on and to confirm that, at least at simulation stage, the new distribution is not distressed by the same issues as the first design we resort again to the circuit simulator. The results (Figures 4.22 to 4.30) show promising results for the possible distribution. The reflection losses are around -8 dB in the band of interest and are similar to the hybrid distribution. However, concerning the imbalance in power distribution, the maximum difference in power pumped to is seen between mixers $3-4$ and $2-5$ and the variation is about ± 0.5 dB (Figure 4.30). The next stage is to develop the 3D models of the three Wilkinson power dividers and attain more realistic expectation about the performance of the design.

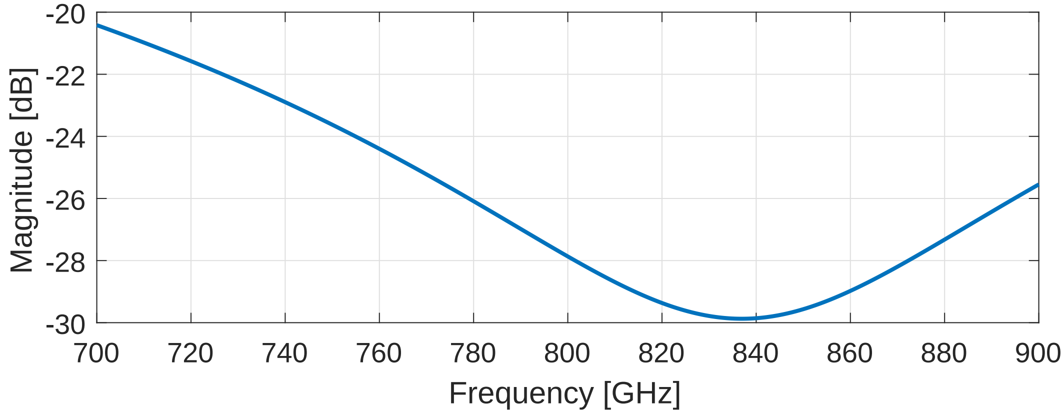

Figure 4.22: Reflections at the input port of the Wilkinson power divider 1:1.

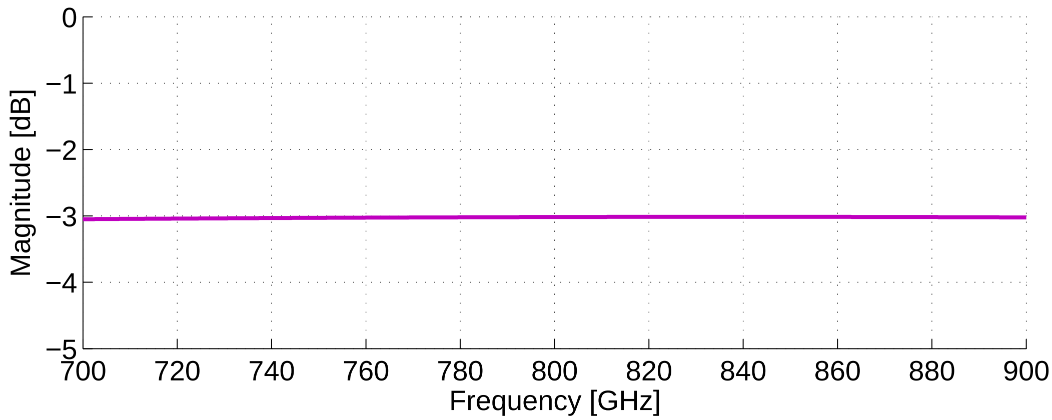

Figure 4.23: Transmissions to output ports 2 and 3 of the 1:1 Wilkinson.

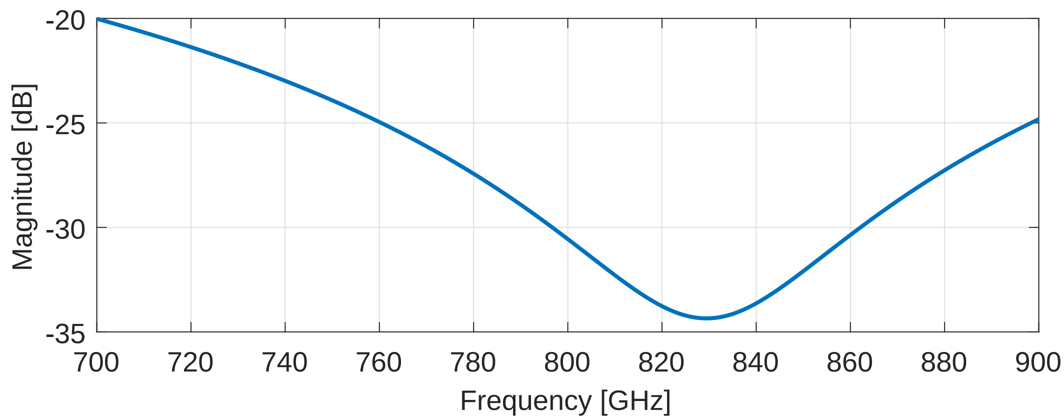

Figure 4.24: Reflections at the input port of the Wilkinson power divider 2:1.

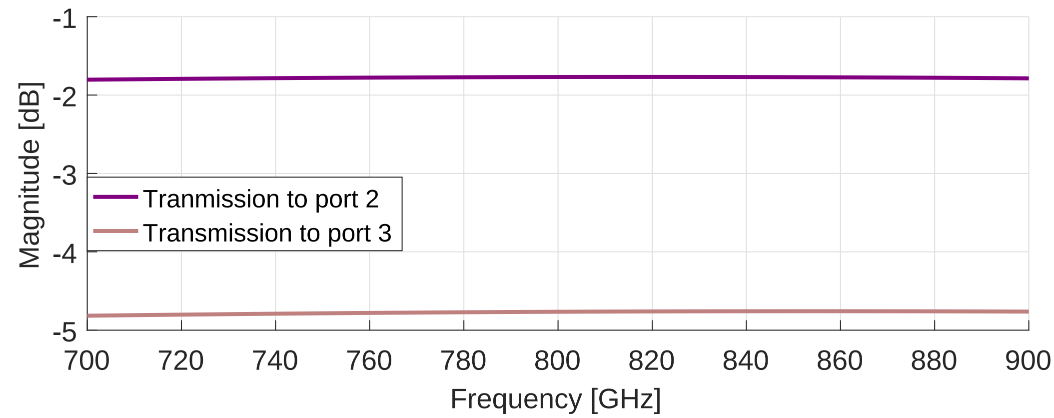

Figure 4.25: Transmissions to output ports 2 and 3 of the 2:1 Wilkinson.

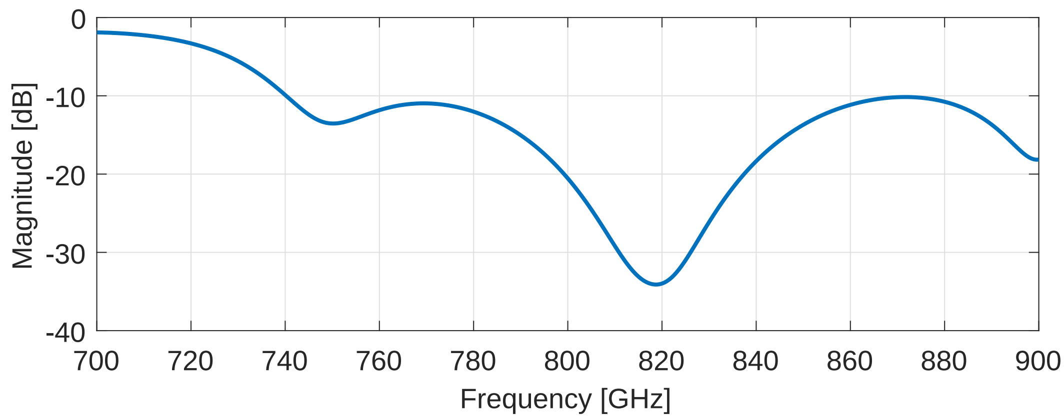

Figure 4.26: Reflections at the input port of the Wilkinson power divider 3:1.

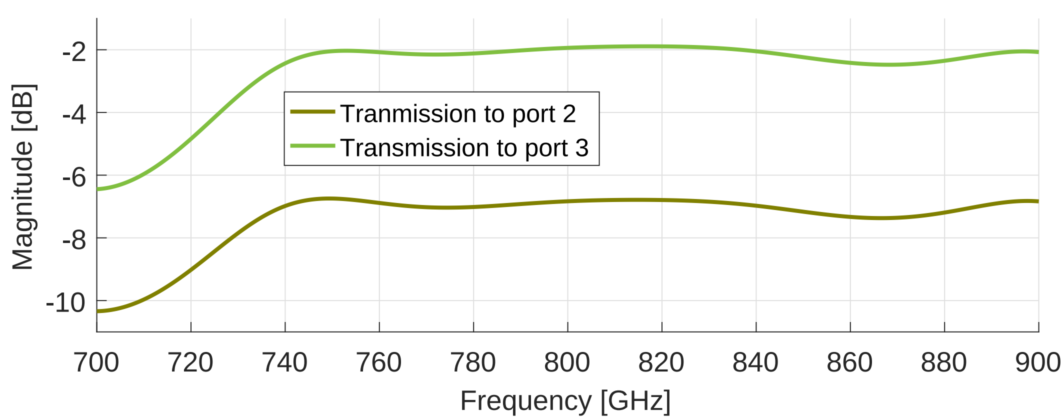

Figure 4.27: Transmissions to output ports 2 and 3 of the 3:1 Wilkinson.

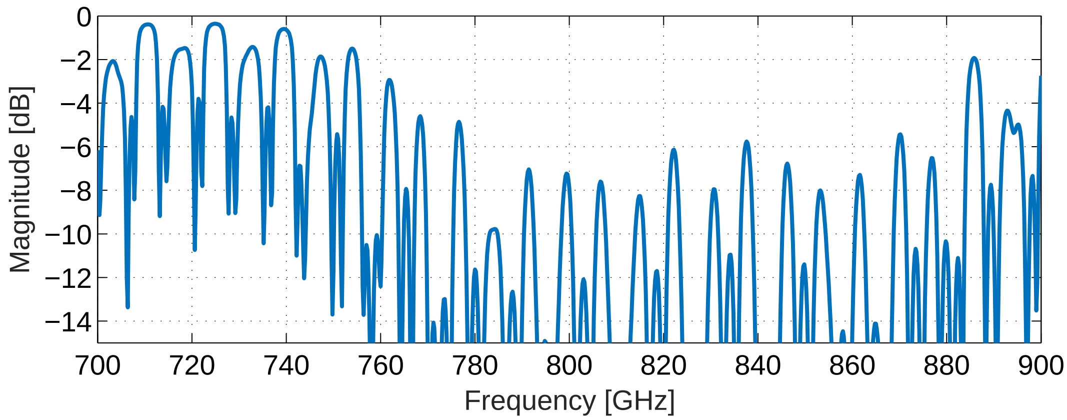

Figure 4.28: Reflections at the input port of the second design of LO distribution network

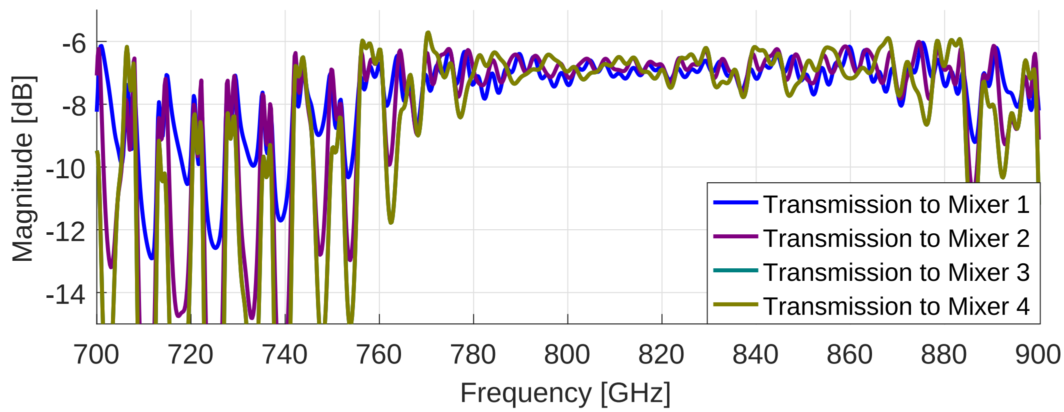

Figure 4.29: Transmission to the four mixers of the basic block.

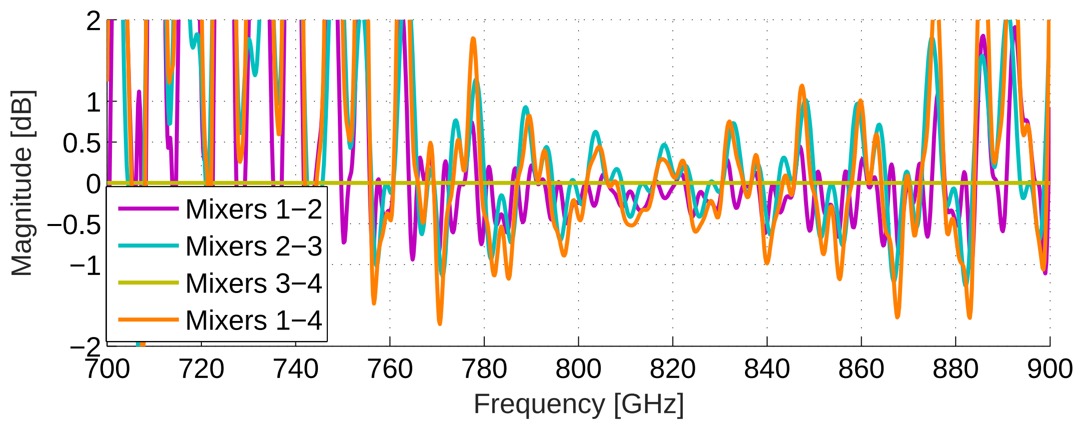

Figure 4.30: Difference in power pumped to the mixers.

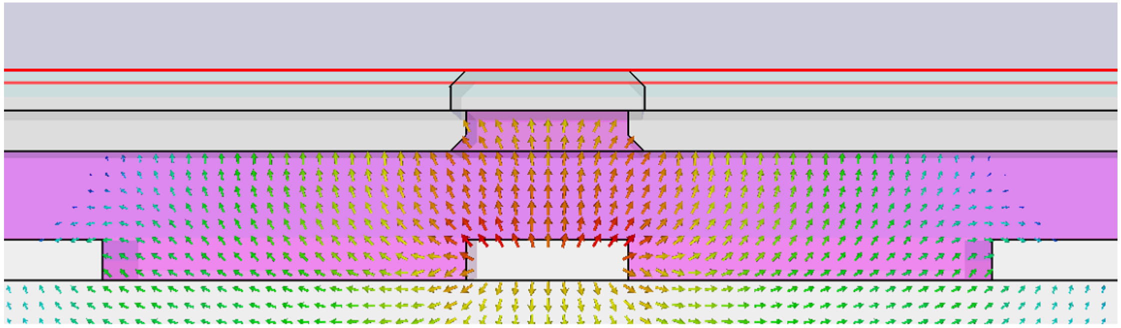

Figure 4.31: Electric field lines in the covered CPW line. It can be seen that the field distribution similar to inverted a Microstrip mode.

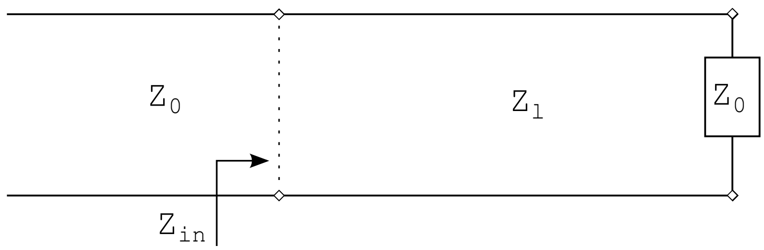

Figure 4.32: DTransmission line scheme for the calculation of Z_{in}.

4.2.2 3:1 Wilkison design

We start modelling the 3:1 Wilkinson because it is the most difficult to design due the high imbalance needed and, therefore, very extreme impedances. CPW lines have a impedance ranging between 30 and 80 Ω that are easily achievable. Impedances outside that range fall in geometries with very acute ratios that are not always possible to manufacture or the processes can take several times longer than for a CPW with lower ratios. To solve this issue we had to resort to non-conventional CPW geometries in order to achieve the required impedances for the Wilkinson divider without resorting to geometries that fall beyond the accuracy and tolerances of the machines.

The 3:1 ratio demands low and high impedances $Z_2 = 23.7\Omega$, $Z_{03} = 108.2\Omega$ and $Z_3 = 71.08\Omega$. The line Z_2 would require a W/s ratio of 6 . To overcome this problem, the CPW is covered with a conductor layer. This changes the distribution of the electromagnetic fields in the line (Figure 4.32) and lowers the impedance to the required levels. Again, as with the conductive bridges, we made use of quartz to support the conductor layer. The dimension of the CPW line Z_2 are effortlessly achieved with values of $W_2 = 4.5$ μm and $s_2 = 3$ μm.

To reach higher impedances the process needed is somewhat harder and cumbersome. CPW impedance of 207 [Ω] have been achieved in [62] using *Electromagnetic Bandgaps* (EBG) in the CPW line. The dimensions and impedance of the line were obtained indirectly from the S parameters [62]. We start with the relationship between S_{11} an the reflections at the input port,

$$S_{11}[\mathrm{d}B] = 20 \cdot log_{10}(|\Gamma|). \tag{4.4}$$

Its known that the input impedance is given by

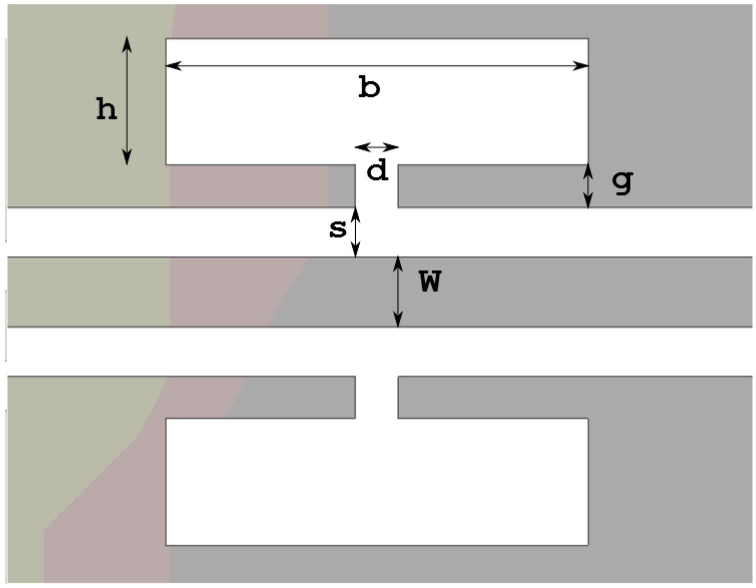

Figure 4.33: Scheme of the CPW EBG

$$Z_l = Z_0\sqrt{\frac{1+|\Gamma|}{1-|\Gamma|}}. \tag{4.5}$$

With these equations we can calculate the line impedance from the input reflection coefficient. In this case we need the input reflection coefficient dependence of the line impedance,

$$|\Gamma| = \frac{Z_l^2 + Z_0^2}{Z_l^2 - Z_0^2}. \tag{4.6}$$

With eq. 4.6 we can obtain the reflection coefficient, and subsequently the S_{11} parameter of the line with given impedance since we known Z_0. To calculate the parameters of the line, we simulated a EBG CPW line in CST microwave studio and used the CPW ports as load with an impedance of 42.65 Ω, which is the line impedance of line Z_0. This method was used to determine the dimension of lines Z_{03} and Z_3.

To obtain the length of the line we used the phase of the S_{12} parameter. The normal wilkinson divider design demands that the lines Z_{02} and Z_{03} have a length of $\lambda_{guided}/4$, but in this case the addition of the EBG to line Z_{03} makes the line somewhat short for construction. To solve this problem the length of the lines is extended to $3\lambda_{guided}/4$. However, this has the effect of narrowing the bandwidth of the divider. The phase equivalent for such length would be $3\pi/2$ or $-\pi/2$. The dimension of lines of the 3 : 1 Wilkinson divider are tabulated in table 4.4. Each EBG for lines Z_{03} and Z_3 was places at the middle of the line.

Table 4.4: Calculated dimension for the $3:1$ Wilkinson power divider

Line	Kind	W [μm]	s [μm]	length [μm]	d [μm]	g [μm]	b [μm]	h [μm]
Z_0	normal	5	2	31.41	-	-	-	-
Z_{02}	covered CPW	4	3	113.14	-	-	-	-
Z_{03}	EBG CPW	5	3.5	182	3	3	38	6
Z_2	normal	4.5	3	56.57	-	-	-	-
Z_3	EBG CPW	5	3.5	105	3	3	30	9

The last device needed for the Wilkinson power divider is the Z_{23} impedance which connects the output lines Z_2 and Z_3. This impedance has the particular feature that it needs to be small respect with the operational wavelength of the device so it can be considered a lumped element. At submillimeter regime the construction of such device is no small feat. Considering that resistive films about $25\,\Omega/square$ of sheet resistance (a square sheet will have 25 Ω regardless the size of the sheet) for 2.3 K temperatures were achieved [63], we can calculate the element that is needed. The resistance of a element can be defined by

$$R = \frac{\rho \cdot l}{Area} = \frac{\rho \cdot l}{h \cdot w}, \tag{4.7}$$

where ρ is the resistivity of the material, l is the length, h is the height and w is the width. Considering the same material in [63] and a height of 45 μm, the relation between the length and width of the slab is

$$l = 1.86 \cdot w. \tag{4.8}$$

Considering a width of 3 μm, the length of the slab is 5.57 μm. Once the dimension of the lines and resistive slab have been determined we proceed to create the model in CST microwave studio. Figure 4.34 shows the model designed with every line labelled. The output lines Z_2 and Z_3 have been adapted by a quarter lambda transformer to the nominal Z_0 line.

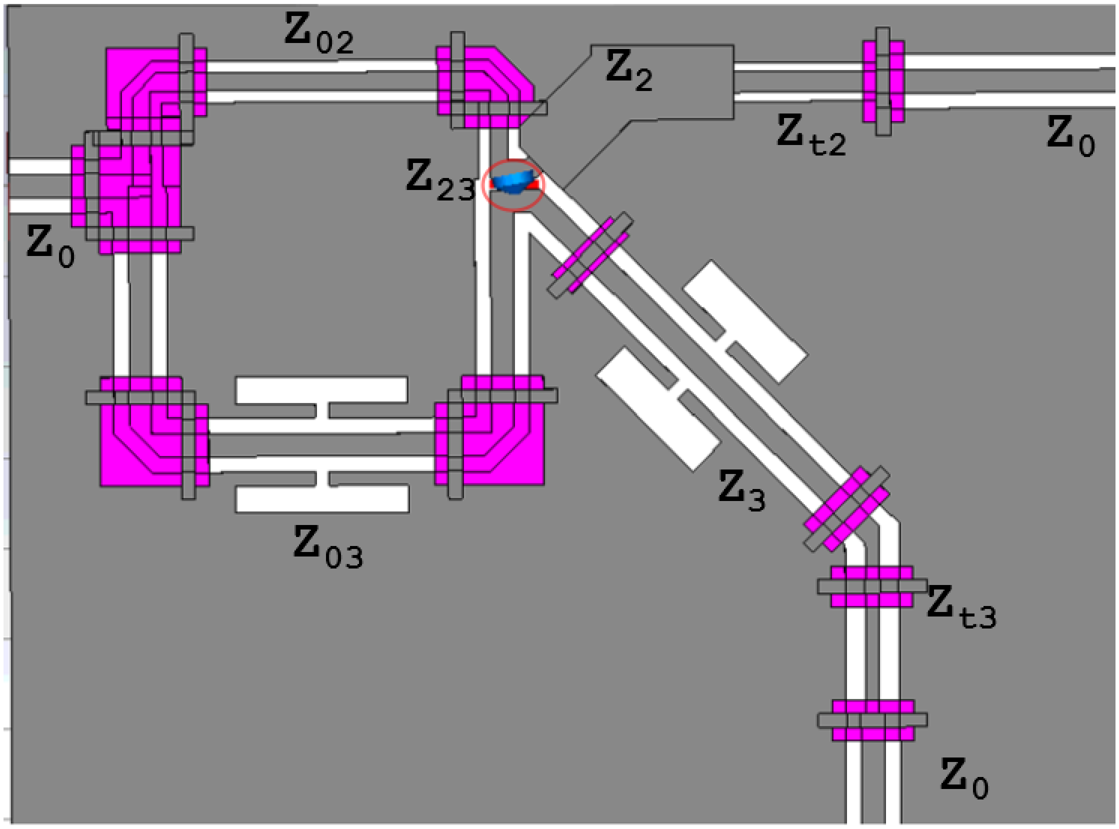

Figure 4.34: Model of the complete model of the 3:1 Wilkinson power divider.

4.3 Simulations of the 3:1 Wilkinson

The design was presented at sec 4.2.2. At this stage we only present a model and results for the 3 : 1 Wilkinson power divider.The simulations of the models does not agree with the theoretical values (Figures 4.35 and 4.36). The reflections at the input port are very high in the band of interest, even reaching −2 dB. The imbalance between ports 2 and 3 is greater than one order of magnitude (−5 and −20). The incongruence between the simulated model and theoretical model are because the theoretical model does not considered the interfaces and connections between each line and the parasitic interactions between them. This model requires further optimization to be fit reach the performance needed for the LO-power distribution.

Table 4.5: Comparison between theoretical and simulated results for the 3:1 Wilkinson power divider

Parameter	Theory	Simulation
Reflections at the input port	−23.34	−2.14
Transmission to port output port 2	−6.84	−24.97
Transmission to output port 3	−1.94	−4.7

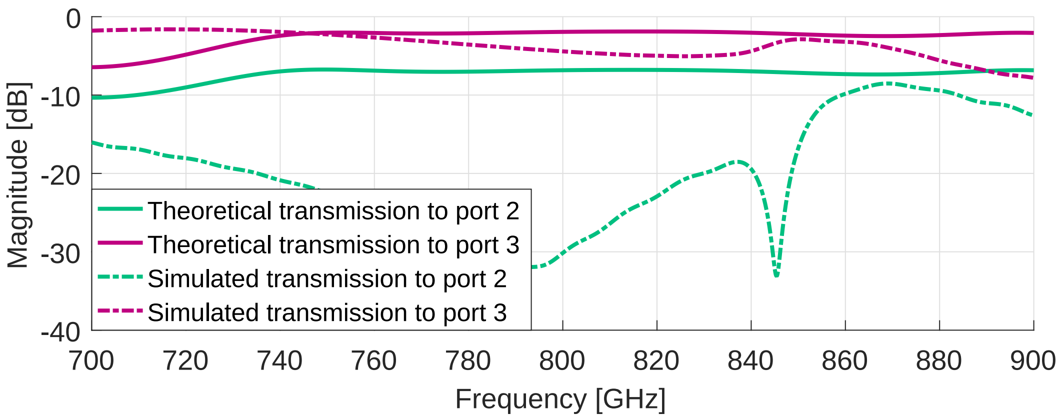

Figure 4.35: Simulated transmissions to output ports 2 and 3 of the 3:1 Wilkinson

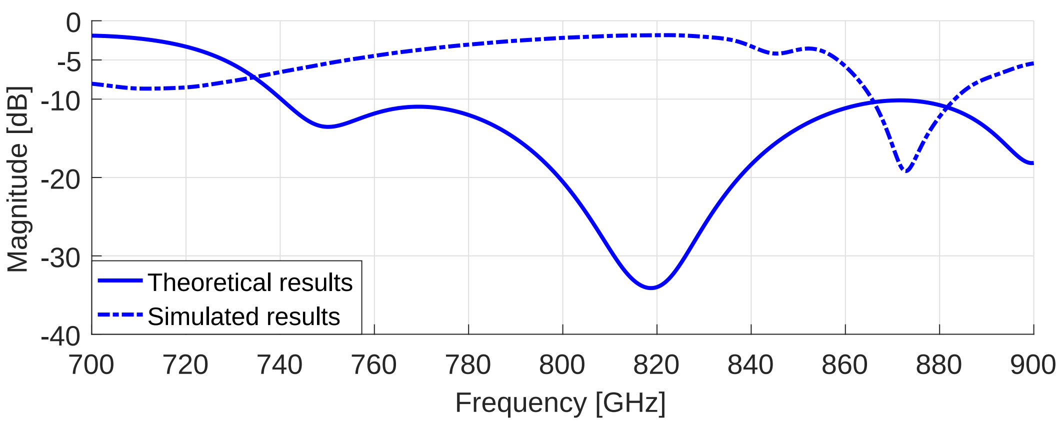

Figure 4.36: Simulated reflections at the input port of the 3:1 Wilkinson

4.4 Summary

Concerning the SMAI LO-power division, we have presented two schemes for the power distribution, one involving balanced power division and the other consisting in imbalanced power division. For the former we developed 90° hybrids for the power division and CPW-to-Waveguide transition to transmit the signal, for the latter we present the theoretical three unequal Wilkinson power dividers with power division ratios of 3:1, 2:1 and 1:1 and expose the design of the 3:1 Wilkinson power divider.

The balanced power division scheme suffered from the standing waves present in the long waveguides delivering the LO signal to the mixers. Thus creating an imbalance in the power pumped to the mixers making the proposed scheme not suitable for the SMAI receiver. On the other hand, the imbalanced scheme has theoretically better performance than the balanced scheme as it does not suffer from standing waves in a great manner. The lines with the most extreme characteristic impedances needed for the most difficult power divider, the Wilkinson 3:1, were designed in the given technology. However, the simulations of the current 3:1 Wilkinson power divider, combining the separately designed lines shows that it is not achieving the expected performance. The reflections at the input port are about

-2 dB and the imbalance between the output port is greater than needed. However, it is expected that further optimization will improve its performance. This taks requires more time, therefore falls outside the scope of this thesis work.

Chapter 5

Conclusions and Future Work

5.1 Effective Conductivity Measurement

The method explained to obtain effective conductivities of particular material on cryogenic conditions has been proven to be an effective way to calculate the effective properties of a mechanized waveguide at different cryogenic temperatures. The effective conductivities of aluminium and C14500 tellurium copper alloys were obtained at 15, 77 and 290 K attaining effective conductivities of $\sigma_{15k} = 1 \cdot 10^8\,[Sm^{-1}]$ and $\sigma_{77k} = 7 \cdot 10^7 [Sm^{-1}]$ for Copper and for the Aluminium: $\sigma_{77k} = 3.6 \cdot 10^7 [Sm^{-1}]$ and $\sigma_{290K} = 1.2 \cdot 10^7$. Further analysis of how the milling process affects the conductivity requires measure the surface roughness of the mechanized waveguides.

5.2 OMT for ALMA BAND 2+3

A second iteration of the band $2 + 3$ OMT was designed, constructed and tested. The new model is a significant upgrade from the first model. The reflections at the output ports show an average level of -24.76 dB for the V polarization and -26.09 dB for the H polarization. The copolar transmissions have an average of -0.52 and -0.69 dB for polarizations V and H, respectively, and fall to 1 dB in the lower part of the band. The cross polar transmissions are below -35 dB in the complete band 2+3 with an average of -42 dB. Finally the isolation between output ports is better than 50 dB and its average across the band is -60.24 dB.

The performance of the OMT complies with almost every requirement imposed and agrees with the HFSS simulations. The parameter that does not present satisfactory levels is the copolar transmissions. The main reason behind this is that the conductivity of the material used is not high enough and the surface roughness is considerable. Future iterations of the OMT should consider manufacture on materials with higher conductivity than Aluminium and a structure that deals with the material mechanical properties and allows proper fabrication.

5.3 LO-power distribution for SMAI

Two LO power distribution systems were proposed. First, a balanced and symmetrical scheme resorting to 90° CPW hybrids. Second, an non symmetrical distribution resorting to Wilkinson power dividers with imbalanced division ratios. The 90° Hybrids design is proposed and the simulations yield good result in the band of interest (800 - 820 GHz). However, due the existence of standing waves on the distribution the imbalance in power pumped to each mixer is greater than 1 dB in the worst cases. Due to this issue, the second scheme was proposed. The theoretical designs of the three Wilkinson power divider were presented and the 3D model of the 3 : 1 Wilkinson is shown. The simulated results of the coupler as a whole were not up to expectations. The reflections at the input port are about -2 dB and the imbalance in power division is greater than 10 dB. The incongruence in behaviour is attributed to parasitic interaction effects between the lines that are not taken into account in the theoretical model. Adapted designs of the Wilkinson power divider must take into account these effects in order to tune the performance of the device accordingly.

Bibliography

[1] CCAT-p, "About ccat." http://www.ccatobservatory.org/index.cfm/page/about-ccat.htm. Accessed: December 7th, 2016.

[2] CCAT-p, "Introduction to radio astronomy." http://www.cv.nrao.edu/course/astr534/Introradastro.html. Accessed: December 8th, 2016.

[3] M. Burton, "NANTEN2 project overview," (St Kilda & Swinburne University, Melbourne), Nanten2 and Mopra: New Studies of the ISM, February 2013.

[4] L. C. Godara, "Introduction to The heterodyne receiving system, and notes on the recent Arlington-Salem tests," *Proceedings of the IEEE*, vol. 87, pp. 1975–1978, Nov 1999.

[5] NRAO, "Karl jansky and the discovery of cosmic radio waves." http://www.nrao.edu/whatisra/hist_jansky.shtml. Accessed: March 3th, 2017.

[6] ALMA, "Introduction to radio astronomy." http://www.almaobservatory.org/en/about-alma/how-does-alma-work/technology/antennas. Accessed: December 8th, 2016.

[7] L. Knee, S. Claude, D. Johnstone, K. Yeung, and the rest of the Band 3 Team, "The band 3 receiver cartridges for alma," *Herzberg Institute of Astrophysics, Victoria, BC, Canada*.

[8] NRAO, *ALMA Band 2 Science Workshop*. Charlottesville, Virginia: NRAO, NAASC Workshops, May 29 - 30, 2013.

[9] K. Vanderlinde, "Properties of and detection of radio and microwave light," Dunlap Institute for Astronomy and Astrophysics, August 2015.

[10] U. U. Graf, C. E. Honingh, K. Jacobs, and J. Stutzki, "Terahertz Heterodyne Array Receivers for Astronomy," *Journal of Infrared, Millimeter, and Terahertz Waves*, vol. 36, no. 10, pp. 896–921, 2015.

[11] J. Payne, "Multibeam receiver for millimeter-wave radio astronomy," *Review of Scientific Instruments*, vol. 59, no. 9, pp. 1911–1919, 1988.

[12] K. Sunada, C. Yamaguchi, N. Nakai, K. Sorai, S. Okumura, and N. Ukita, "BEARS: SIS 25-beam array receiver system for the NRO 45-m telescope," in *Radio Telescopes*

(H. Butcher, ed.), vol. 4015 of *Proc. SPIE 4015, Radio Telescopes*, pp. 237–246, Jul 2000.

[13] R. Güsten, G. Ediss, F. Gueth, K. Gundlach, H. Hauschildt, C. Kasemann, T. Klein, J. Kooi, A. Korn, I. Kramer, R. LeDuc, H. Mattes, K. Meyer, E. Perchtold, M. Pilz, R. Sachert, M. Scherschel, P. Schilke, G. Schneider, J. Schraml, D. Skaley, R. Stark, W. Wetzker, H. Wiedenhover, S. Wongsowijoto, and F. Wyrowski, "Champ: the carbon heterodyne array of the mpifr," in *Proceedings SPIE*, vol. 3357, pp. 167–177, 1998.

[14] C. Kasemann, R. Güsten, S. Heyminck, B. Klein, T. Klein, S. Philipp, A. Korn, G. Schneider, A. Henseler, A. Baryshev, and T. Klapwijk, "Champ+: a powerful array receiver for apex," in *Proceedings SPIE*, vol. 6275, pp. 62750N–62750N–12, 2006.

[15] C. Walker, C. Groppi, D. Golish, C. Kulesa, A. Hungerford, C. D. d'Aubigny, K. Jacobs, U. Graf, C. Martin, and J. Kooi, "Polestar: An 810 ghz array receiver for ast/ro," in *Proceedings of the 12th International Symposium on Space Terahertz Technology*, (San Diego, California), February 2001.

[16] K. F. Schuster, C. Boucher, W. Brunswig, M. Carter, J. Y. Chenu, B. Foullieux, A. Greve, D. John, B. Lazareff, S. Navarro, A. Perrigouard, J. L. Pollet, A. Sievers, C. Thum, and H. Wiesemeyer, "A 230 ghz heterodyne receiver array for the iram 30 m telescope," *Astronomy and Astrophysics*, vol. 423, no. 3, pp. 1171–1177, 2004.

[17] U. Graf, S. Heyminck, E. Michael, S. Stanko, C. Honingh, K. Jacobs, R. Schieder, and J. Stutzki, "SMART: The KOSMA Sub-Millimeter Array Receiver for Two frequencies," in *Proceedings of the 13th International Symposium on Space Terahertz Technology*, (Cambridge, Massachusetts), March 2002.

[18] C. Groppi, C. Walker, C. Kulesa, D. Golish, A. Hedden, P. Gensheimer, G. Narayanan, A. Lichtenberger, U. Graf, and S. Heyminck, "Desertstar: a 7 pixel 345 ghz heterodyne array receiver for the heinrich hertz telescope," in *Proceedings SPIE*, vol. 4855, pp. 330–337, 2003.

[19] J. V. Buckle, R. E. Hills, H. Smith, W. R. F. Dent, G. Bell, E. I. Curtis, R. Dace, H. Gibson, S. F. Graves, J. Leech, J. S. Richer, R. Williamson, S. Withington, G. Yassin, R. Bennett, P. Hastings, I. Laidlaw., J. F. Lightfoot, T. Burgess, P. E. Dewdney, G. Hovey, A. G. Willis, R. Redman, B. Wooff, D. S. Berry, B. Cavanagh, G. R. Davis, J. Dempsey, P. Friberg, T. Jenness, R. Kackley, N. P. Rees, R. Tilanus, C. Walther, W. Zwart, T. M. Klapwijk, M. Kroug, and T. Zijlstra, "Harp/acsis,"

[20] C. Walker, C. Kulesa, P. Bernasconi, H. Eaton, N. Rolander, C. Groppi, J. Kloosterman, T. Cottam, D. Lesser, C. Martin, A. Stark, D. Neufeld, C. Lisse, D. Hollenbach, J. Kawamura, P. Goldsmith, W. Langer, H. Yorke, J. Sterne, A. Skalare, I. Mehdi, S. Weinreb, J. Kooi, J. Stutzki, U. Graf, M. Brasse, C. Honingh, R. Simon, M. Akyilmaz, P. Puetz, and M. Wolfire, "The stratospheric thz observatory (sto)," in *Proceedings SPIE*, vol. 7733, pp. 77330N–77330N–9, 2010.

[21] A. Young, W. Chris, C. Kulesa, P. Bernasconi, R. Dominguez, J. Siles, D. Hayton,

J. R. Gao, W. Peters, and P. Goldsmith, "Stratospheric terahertz observatory 2016, sub-orbital flight from mcmurdo, antarctica," in *28th International Symposium on Space Terahertz Technolog*, (Cologne, Germany), March 13-15, 2017.

[22] C. Groppi, C. Walker, C. Kulesa, D. Golish, J. Kloosterman, S. Weinreb, G. Jones, J. Barden, H. Mani, T. Kuiper, J. Kooi, A. Lichtenberg, T. Cecil, G. Narayanan, P. Pütz, and A. Hedden, "Supercam: A 64 pixel heterodyne array receiver for the 350 ghz atmospheric window," in *Proceedings of the 20th International Symposium on Terahertz Space Technology*, (Charlottesville), April 2009.

[23] A. L. Fontana, B. Lazareff, A. Navarrini, and Y. Bortolotti, "Heterodyne array receiver for radio astronomy in the 2mm band," in *Proceedings of the 40th European Microwave Conference (EuMC)*, pp. 906–909, Sept 2010.

[24] A. L. Fontana, C. Boucher, P. Serres, Y. Bortolotti, I. Cope, F.and Stil, B. Lefranc, O. Garnier, G. Butin, F. Mattiocco, S. Navarro, D. John, A. Navarrini, and K. F. Schuster, "A 3mm multipixel SIS receiver for IRAM 30-m pico veleta telescope," in *Proceedings SPIE*, vol. 8452, pp. 84522E–84522E–11, 2012.

[25] C. Groppi, C. Wheeler, H. Mani, S. Weinreb, D. Russell, J. Kooi, A. Lichtenberg, and C. Walker, "The kilopixel array pathfinder project (kappa): A 16 pixel 660 ghz pathfinder instrument with an integrated heterodyne focal plane detector," in *Proceedings of the 22nd International Symposium on Space Terahertz Technology*, (Tucson, Arizona), pp. 152–158, April 2011.

[26] G. S. Staff, "Observing with the green bank telescope." https://science.nrao.edu-/facilities/gbt/observing/GBTog.pdf, November 2015. Accessed: July 12th, 2016.

[27] P. Bolli, A. Orlati, L. Stringhetti, A. Orfei, S. Righini, R. Ambrosini, M. Bartolini, C. Bortolotti, F. Buffa, M. Buttu, A. Cattani, N. D'Amico, G. Deiana, A. Fara, F. Fiocchi, F. Gaudiomonte, A. Maccaferri, S. Mariotti, P. Marongiu, A. Melis, C. Migoni, M. Morsiani, M. Nanni, F. Nasyr, A. Pellizzoni, T. Pisanu, M. Poloni, S. Poppi, I. Porceddu, I. Prandoni, J. Roda, M. Roma, A. Scalambra, G. Serra, A. Trois, G. Valente, G. P. Vargiu, and G. Zacchiroli, "Sardinia Radio Telescope: General Description, Technical Commissioning and First Light," *Journal of Astronomical Instrumentation*, vol. 04, no. 03n04, p. 1550008, 2015.

[28] M. Sieth, K. Devaraj, P. Voll, S. Church, R. Gawande, K. Cleary, A. C. S. Readhead, P. Kangaslahti, L. Samoska, T. Gaier, P. F. Goldsmith, A. I. Harris, J. O. Gundersen, D. Frayer, S. White, D. Egan, and R. Reeves, "Argus: a 16-pixel millimeter-wave spectrometer for the green bank telescope," in *Proceedings SPIE*, vol. 9153, pp. 91530P–91530P–12, 2014.

[29] C. Risacher, R. Güsten, J. Stutzki, H. W. Hübers, D. Büchel, U. Graf, M. Greiner-Baer, S. Heyminck, C. Honingh, K. Jacobs, , B. Klein, P. Pütz, H. Richter, N. Rothbart, and O. Ricken, "The upgreat thz heterodyne arrays for sofia: 1.9 thz and 4.7 thz first results," in *28th International Symposium on Space Terahertz Technology*, (Cologne, Germany), March 13-15 2017.

[30] M. Niemack, "Designs for a large-aperture telescope to map the cmb 1x faster," *Applied Optics*, vol. 55, p. 1686, march 2016.

[31] "Conceptual design by s. parshley."

[32] CCAT-p. `http://www.xoptx.com/cornell-caltech-atacama.php`. Accessed: December 15th, 2016.

[33] CCAT-p, "Initial instrumentation plan for ccat-p." `http://www.ccatobservatory.org/docs/ccat-technical-memos/CCAT-p.instruments.160707.pdf`. Accessed: December 10th, 2016.

[34] CCAT-p, "Ccat pathfinder ksz science case: Probing the transition between gravity and dark energy dominated regimes." `http://www.ccatobservatory.org/docs/ccat-technical-memos/CCAT-p.kSZ_whitepaper.pdf`. Accessed: December 11th, 2016.

[35] CCAT-p, "Ccat-p : Science cases." `http://www.ccatobservatory.org/docs/ccat-technical-memos/CCAT-p.IMEOR.v2.pdf`. Accessed: December 12th, 2016.

[36] CCAT-p, "Ccat-p science case for geco." `http://www.ccatobservatory.org/docs/ccat-technical-memos/CCAT%20Pathfinder%20Science%20Case_GEco_03Feb2017.pdf`. Accessed: December 13th, 2016.

[37] U. U. Graf, S. Heyminck, E. Michael, S. Stanko, C. E. Honingh, K. Jacobs, R. Schieder, and J. Stutzki, "SMART: The KOSMA Sub-Millimeter Array Receiver for Two Frequencies," Thirteenth International Symposium on Space Terahertz technology, Harvard Univerisity, March 2002.

[38] D. Pozar, *Microwave Engineering*. New York: Wiley, 4th ed., 2011.

[39] J. C. Maxwell, *A Treatise on Electricity and Magnetism*. Londres: Oxford,Clarendon press series, 1st ed., 1873.

[40] O. Heaviside, *Electromagnetic Theory*. The Electrician, 1st ed., 1893.

[41] C. Balanis, *Advanced Engineering Electromagnetics*. Wiley, 2nd ed., 2012.

[42] *IEEE Standard 145-1983, IEEE Standard Definitions of Terms for Antennas*, vol. AP-31. reprinted in *IEEE Trans. Antennas Propagat.*, November 1983.

[43] L. Rayleigh, *On the Passage of Electric Waves through Tubes*, vol. 43. Philosofical Magazine, 1897,Reprinted in *Collected Papers*, Cambridge University Press, Cambridge, 1903.

[44] A. Boifot, "Classification of orthomode transducers," *European Transactions on Telecommunication and Related Technologies*, vol. 2, no. 5, pp. 503–510, 1991.

[45] A. Navarrini and R. Plambeck, "A turnstile junction waveguide orthomode transducer,"

Microwave Theory and Techniques, IEEE Transactions on, vol. 54, pp. 272–277, Jan 2006.

[46] J. L. Cano, A. Tribak, R. Hoyland, A. Mediavilla, and E. Artal, "Full band waveguide turnstile junction orthomode transducer with phase matched outputs," *International Journal of RF and Microwave Computer-Aided Engineering*, vol. 20, no. 3, pp. 333–341, 2010.

[47] K. Gupta, R. Grag, I. Bahl, and P. Bhartia, *Microstrip lines and Slotlines.* Boston, London: Artech House, 2nd ed., 1996.

[48] R. N. Simons, *Coplanar Waveguide Circuits, Components, and Systems.* Wiley-Interscience, 2001.

[49] R. E. Collins, *Foundations for Microwave Engineering.* New York: MC Graw-Hill, 2nd ed., 1992.

[50] A. Dunning, "Double ridged orthogonal mode transducer for the 16-26ghz microwave band," *CSIRO Australia Telescope National Facility Memo*.

[51] P. Zorzi, "Design and constructions of an optical system for a 31-45 ghz radioastronomical receiver," 2013.

[52] I. Barrueto González, "Diseño de un transductor de modos ortonormales para la banda 2 + 3 de alma," engineering thesis, Universidad de Chile.

[53] D. Henke and S. Claude, "Minimizing rf performance spikes in a cryogenic orthomode transducer (omt)," vol. 62, no. 4, pp. 840–850, 2014.

[54] `http://nptel.ac.in/courses/117101057/downloads/lec46.pdf`. Accessed: April 18th, 2017.

[55] I. Stil, A. Fontana, B. Lefranc, A. Navarrini, P. Serres, and K. Schister, "Loss of wr10 waveguide across 70-116 ghz," *22nd Internationas Symposium on Space Terahertz Technology, Tokyo*, April 2-4 2012.

[56] M. P. Westig, *Quantum limited balanced superconducting 380-520 GHz mixer on a silicon membrane and mesoscopic tunnel devices for terahertz frequencies.* PhD thesis, Universität zu Köln, Zülpicher Strasse 77 50937 Koeln, 2015.

[57] J. Reed, "A method of analysis of symmetrical four-port networks (correspondence)," *IRE Transactions on Microwave Theory and Techniques*, vol. 5, pp. 162–163, April 1957.

[58] *https://awrcorp.com/download/faq/english/docs/Elements/CPWABRGX.htm.*

[59] A. Rida, A. Margomenos, and M. M. Tentzeris, "A method of analysis of symmetrical four-port networks (correspondence)," *IRE Transactions on Microwave Theory and Techniques*, vol. 5, pp. 162–163, April 1957.

[60] E. J. Wilkinson, “An n-way hybrid power divider,” *IRE Transactions on Microwave Theory and Techniques*, vol. 8, pp. 116–118, January 1960.

[61] J.-S. Lim, S.-W. Lee, C.-S. Kim, J.-S. Park, D. Ahn, and S. Nam, “A 4:1 unequal wilkinson power divider,” *IEEE Microwave and Wireless Components Letters*, vol. 11, pp. 124–126, March 2001.

[62] C.-P. Chang, C.-C. Hung, and Y.-H. Wang, “A 6:1 unequal wilkinson power divider with ebp cpw,” *Profress in Electromagnetics Research Letters*, vol. 8, pp. 151–159, 2009.

[63] M. Schicke, P. Sabon, and K.-F. Schuster, “Nbnx thin film resistors for cryogenic application,” *Thin Solid Films*, vol. 384, no. 2, pp. 294–297, 2001.